POLITECNICO DI TORINO

Master Degree in Biomedical Engineering

Biomedical Instrumentation

Master Degree Thesis

Test of a new ultrasound system for monitoring the edges of the inferior vena cava

Supervisor:
prof. Luca Mesin
Co-supervisor:
Piero Policastro

Candidates:
Aurora Giambartolomei
Michela Pieragostini

March 2023

Abstract

The size and pulsatility of the inferior vena cava (IVC) allow the extraction of parameters that are difficult to estimate but essential for a correct diagnosis, such as the right atrial pressure or the blood volume status of patients. No standardized method exists for the analysis of this vessel. One of the most widely used techniques is M-mode ultrasound. However, this only allows the IVC scan to be viewed along a fixed direction and therefore cannot refer to the same section of the vessel as the vein moves during respiratory and cardiac activity. To overcome these limitations, a new software has been developed by Vein Image Processing for Edge Rendering (VIPER). This software allows the identification of vein edges and displacements, both along the transverse and longitudinal planes, by means of a semi-automatic analysis of B-mode ultrasound videos. The aim of this thesis is to evaluate the ability of this software to correctly segment IVC in different working conditions. The analysis was carried out by means of a comparison with manual segmentation masks. In particular, the research assessed the software's dependence on user input, the reliability and the resilience to occasional events. Finally, the algorithm was tested on ultrasound videos acquired from doctors. To objectively analyze the results obtained, the variability of manual segmentations was also evaluated. Along the transverse plane, the software is independent of user input, while greater sensitivity to input was found in the longitudinal plane. The software can correctly segment the vessel both in static conditions and during vein movements. The main limitations are the sensitivity to noise, the inability to recognize the disappearance of the vessel and the difficulty in segmenting small veins. Nevertheless, the good performance achieved shows that this software is an excellent tool to overcome the limits currently existing in the clinical field for the analysis of IVC pulsatility.

Contents

List of Figures

List of Tables

Chapter 1

Introduction

The inferior vena cava (IVC) is one of the main vessels of the human circulatory system. It is characterized by elastic walls that make the vessel size sensitive to pressure changes regularly produced by cardiac and respiratory activity. During the cardiac cycle, the diameter of the IVC decreases before atrial systole and increases during atrial contraction. During respiratory activity, the vessel is smallest during inspiration and largest during expiration. However, opposite variations occur in the case of patients undergoing mechanical ventilation without respiratory effort. Any maneuver or pathological condition that alters the pressure or blood volume in the abdominal compartment affects both the size of the IVC and how much the vessel size varies. For this reason, the study of the pulsatility and size of this vein is of great interest in medicine. It allows the evaluation of many critical conditions, such as cases of fibrosis and pulmonary cirrhosis, and extracts information on right heart function. In addition, IVC caliber assessment may be a new technique to estimate right atrial pressure (RAP) and blood volume status in patients. Indeed, to date, there is no noninvasive method to correctly estimate RAP or accurate technique to study blood volume. Unfortunately, the analysis of the pulsatility of this vessel is made particularly complex by the movements along the transverse plane and along the longitudinal plane generated by respiration. The main analysis techniques are based on the acquisition of M-mode or B-mode ultrasound videos of the IVC and aim to estimate the Caval Index (CI). This index, which is calculated from the difference between the maximum and minimum diameters, is representative of the pulsatility of the IVC. Specifically, M-mode ultrasonography works along a fixed direction and represents on screen a section of the vessel from which its diameter can be estimated. However, due to the movement of the vein, the section investigated varies over time, making the analysis inaccurate. On the other hand, B-mode ultrasound allows complete visualization of the IVC in both the transverse and longitudinal planes. In this case, however, the choice of vessel section to measure the parameters of interest makes this technique highly operator dependent. In addition, the results of both modalities are not very reproducible because it is up to the operator to identify the moment in which the measurements should be taken. To overcome these limitations, a startup called Vein Image Processing for Edge Rendering (VIPER) has developed new semi-automated software that can detect the inferior vena cava and follow its movements in both the longitudinal and transverse planes. The goal of this algorithm is to provide accurate and repeatable measurements that assist clinicians in making diagnosis and treatment decisions. Several studies have been conducted on early versions of this software and have already demonstrated the benefits it could introduce in estimating RAP or blood volume. This thesis aims to analyze the ability and accuracy of the software to segment the vein under different working conditions. Specifically, the analysis focuses on the latest update released by VIPER and evaluates the dependence on user input, reliability, and resilience to occasional events. The segmentations obtained by the algorithm were compared with manual masks. The first chapters of this study will describe the anatomy of the IVC and the respiratory and circulatory systems that influence

its pulsatility. Next, the basic principles of ultrasonography, possible clinical applications of the IVC and previous studies on the software will be briefly presented. Finally, the method used, the tests performed, and the results obtained will be described.

Chapter 2

Respiratory system

All living cells of the human body require oxygen (O_2) to survive and produce carbon dioxide (CO_2) during aerobic respiration. The respiratory system is the structure that enables the exchange of gases between the air and the blood. The circulatory system carries oxygenated blood from the lungs to the body's cells and returns deoxygenated blood from the body's cells to the lungs. For this reason, the respiratory and cardiovascular systems are closely related both anatomically and functionally. In addition, the respiratory system performs other functions: the nose is the seat of olfactory function, the larynx is the organ of phonation, and it is also involved in the regulation of blood pH.

The main elements that constitute this system are the nasal cavity, pharynx, larynx, trachea, bronchi and finally lungs. Specifically, the upper respiratory tract refers to the nose, the pharynx, and associated tissues, while the lower respiratory tract includes the larynx, trachea, bronchi, and lungs (figure 2.1). The inner part of the nose consists of two nasal cavities, that are always open and allow the passage of air. These channels are covered by a mucous membrane that secretes a layer of mucus, hat cleans, humidifies, and warms the inhaled air. The nasal cavities communicate with the pharynx, a hollow organ common to both the digestive and respiratory systems. In particular, the pharynx is connected inferiorly to the respiratory system at the larynx. The larynx is another important element of the respiratory system, performing three basic functions: through the thyroid gland and cricoid cartilages it maintains an open passage for air; the epiglottis and vestibular folds prevent ingested food from moving into the larynx; through the vocal folds it enables the production of sound. The larynx is followed by the trachea, a membranous tube consisting of dense, regular connective tissue and smooth muscle reinforced with 15-20 C-shaped pieces of cartilage. The cartilages protect the trachea and maintain the open passage for air. In the end, the trachea divides to form two smaller tubes called primary bronchi, which, in turn, split to create bronchi that are smaller and smaller until, at last, numerous microscopic tubes and sacs are generated. These tubes and sacs then give rise to the bronchioles, which are characterized by a diameter of less than 1 mm. The bronchioles subdivide in turn until they become terminal bronchioles, which are even smaller. Starting from the trachea, all airways are denoted as the tracheobronchial tree. The conducting zone and the respiratory zone are two divisions of the tracheobronchial tree based on their functions. The conducting zone, which connects the trachea to the terminal bronchioles, acts as a passageway for air circulation and is lined with epithelial tissue that helps move debris out of the tracheobronchial tree and out of the trachea. On the other hand, the respiratory zone extends from the terminal bronchioles to small air sacs called alveoli, which serve as the sites of air-blood gas exchange. The walls of the respiratory bronchioles consist of collagenous and elastic connective tissue with bundles of smooth muscle. Precisely, gas exchange between air and blood takes place at the level of the respiratory membrane of the lungs and it consists of pavement epithelial cells. This membrane is very thin to facilitate the diffusion of gases. Finally,

there are the two lungs, the main organs of respiration. The right lung consists of three lobes and the left has two lobes. The base of each lung rests on the diaphragm, while the apex of each lung extends superiorly to a point about 2.5 cm above the clavicle.

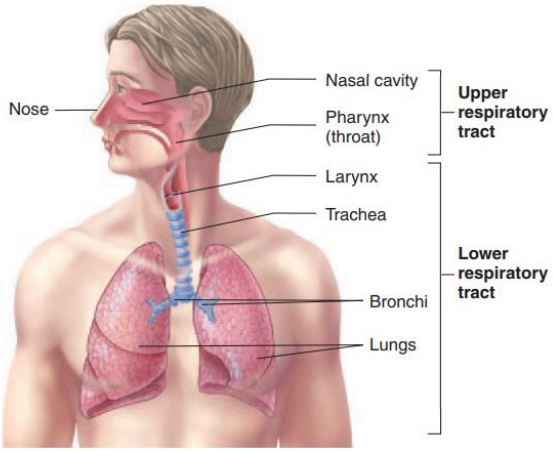

Figure 2.1: The figure shows the respiratory system, which can be divided into the upper and the lower respiratory tract. The upper respiratory tract refers to the nose, the pharynx, and associated tissues, whereas the lower respiratory tract involves the larynx, trachea, bronchi, and lungs. [1]

Respiratory function occurs in four main stages:

1. Ventilation: movement of air in and out of the lungs.
2. Exchange of gases between the air entering the lungs and the blood.
3. Transport of O_2 and CO_2 through the blood occurs.
4. Exchange of gases between the blood and tissues.

For ventilation, a pressure gradient from the outside of the body to the alveoli is needed for airflow into the lungs, and the opposite is required for airflow out of the lungs. The following relationship applies:

$$F = \frac{P1 - P2}{R} \tag{2.1}$$

where F is the air flow inside a generic cylinder, $P1$ is the pressure at point one, $P2$ is the pressure at point two, and R is the resistance to flow. Air moves through tubes because of a pressure difference. When $P1$ is greater than $P2$, gas flows from $P1$ to $P2$ at a rate that's proportional to the pressure difference. Furthermore, the general law of gases states reveals that air pressure is inversely proportional to volume. As the volume increases, the pressure decreases and vice versa, according to the following law:

$$P = \frac{nRT}{V} \tag{2.2}$$

where P is pressure, n is the number of grams moles of gas, R is the gas constant, T is the absolute temperature, and V is the volume. Air, then, reaches the lungs through the respiratory movements made possible by the diaphragm, chest wall muscles, and abdominal muscles. These movements generate a change in thoracic volume, which in turn causes a change in alveolar volume. Since changes in alveolar volume produce changes in alveolar pressure, the pressure difference between the atmospheric air pressure outside the body, barometric air pressure (P_B), and the pressure inside an alveolus, alveolar pressure (P_{alv}), determines the movement of air. It is possible to highlight four different values that the pressure gradient can take corresponding to four moments of breathing (figure 2.2):

1. At the end of exhalation, atmospheric pressure and alveolar pressure are equal. Therefore, no air passage takes place.
2. During inspiration, contraction of the inspiratory muscles increases thoracic volume resulting in expansion of the lungs and increase in alveolar volume. The increase in alveolar volume causes a decrease in alveolar pressure below atmospheric pressure. Air enters the lungs.
3. At the end of inspiration, the chest and the alveoli stop expanding and alveolar pressure becomes equal to atmospheric pressure due to the presence of air in the lungs. No air movement occurs.
4. During expiration, on the other hand, the chest volume decreases as the diaphragm relaxes and the chest and lungs retract. The decrease in thoracic volume causes a decrease in alveolar volume and thus an increase in alveolar pressure relative to atmospheric pressure. Air flows out of the lungs.

The diffusion of gases between blood and alveoli in the pulmonary capillaries is the following stage in the breathing process. The behavior of gas molecules predicts that gas tends to move from the area of higher concentration to the area of lower concentration until a homogeneous mixture is obtained. Once oxygen diffuses into the blood, most of it combines reversibly with hemoglobin, and a smaller amount dissolves in the plasma. Hemoglobin then transports oxygen, via blood vessels, from the pulmonary capillaries to the tissue capillaries, where some of the oxygen is released. In aerobic respiration, the oxygen diffuses from the blood to the tissue cells. In turn, carbon dioxide is produced by cells during aerobic metabolism, and it diffuses into the tissue capillaries. Once carbon dioxide enters the blood it is transported in the form of bicarbonate ions. [1], [2]

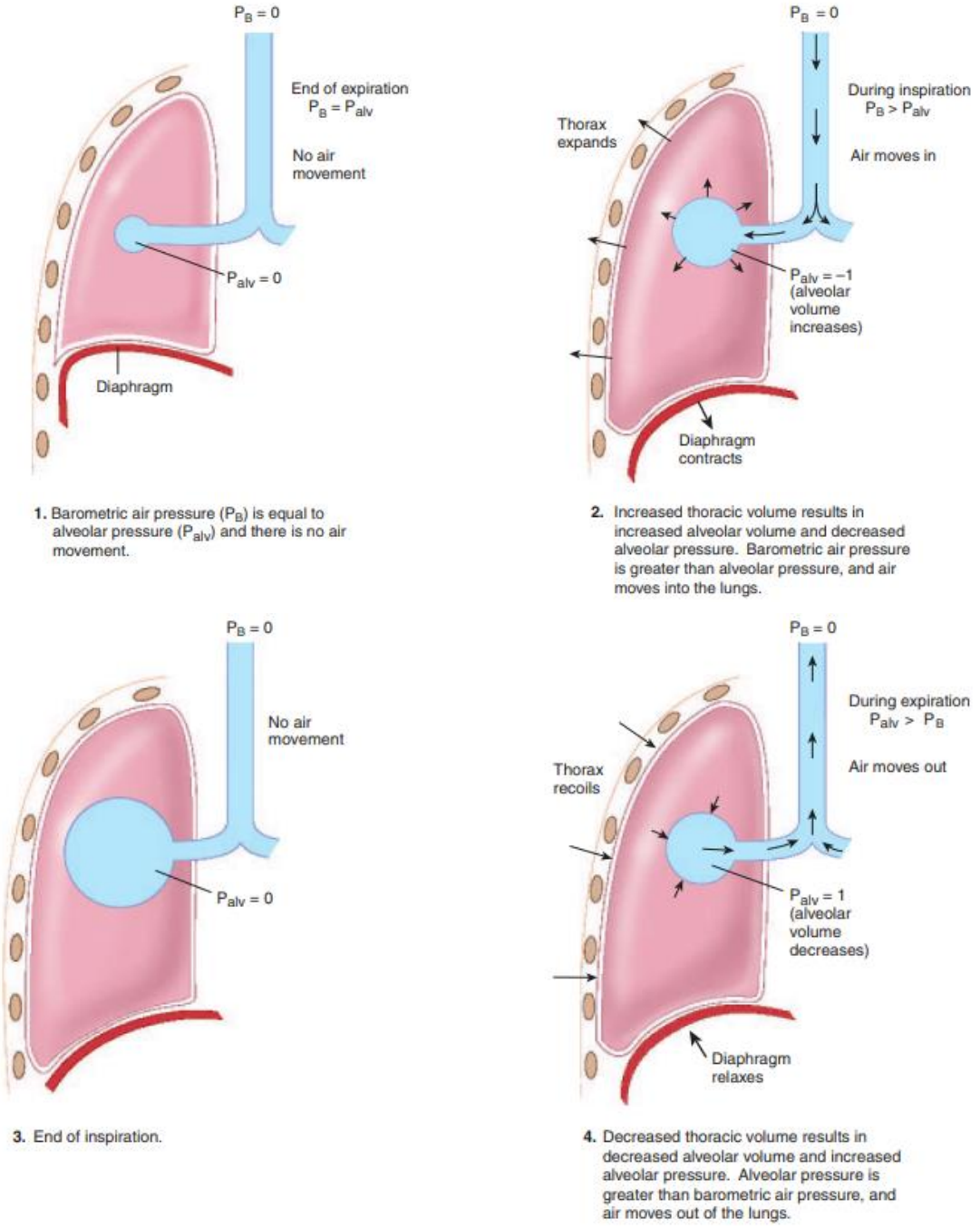

Figure 2.2: The figure shows how alveolar pressure changes during the four main phases of respiration: end of expiration (A), inspiration (B), end of inspiration (C), expiration (D). [1]

Chapter 3

Cardiovascular system

The cardiovascular system consists of a central organ, the heart, and numerous branching channels, the blood vessels, which are divided into arteries, veins, and capillaries. Nutrient fluids, namely blood and lymph, circulate in these vessels. Blood performs many essential functions in life. It is a type of connective tissue consisting of cells and cell fragments surrounded by a liquid matrix. The cells and cell fragments constitute the corpuscular part, and the plasma is the liquid part. About 45% of the total volume of blood is made up of cells and cell fragments, the remaining 55% of plasma. Because cells are metabolically active, as was seen in the previous section, they require a constant supply of nutrients and removal of waste. These tasks are performed by the cardiovascular system; the heart pumps blood through the vessels, and the blood supplies nutrients and collects waste products.

The heart is a hollow organ consisting of two communicating pumps. The right pump receives blood from the body and pumps it into the pulmonary circulation, or small circulation, which carries blood to the lungs for gas exchange and returns oxygenated blood to the left side of the heart. The left side of the heart pumps blood through the systemic circulation, also called the great circulation, which supplies oxygen and nutrients to the various tissues of the body. From those tissues, carbon dioxide and other waste products are returned to the right side of the heart.

Blood pressure regulates blood flow and is therefore essential for maintaining the body's homeostasis. Mean arterial pressure (MAP) is defined as the average blood pressure between the systolic and diastolic pressures in the aorta. It is proportional to cardiac output (CO) multiplied by peripheral resistance (PR). CO is the amount of blood pumped by the heart per minute, and PR is the total resistance against which blood must be pumped. Both the blood vessels and the heart are regulated to ensure that the blood pressure is high enough to generate flow to meet the metabolic needs of the tissues.

The ventricles pump blood from the heart to large elastic arteries that branch repeatedly to form progressively smaller arteries. As they become smaller, arteries undergo a gradual transition from having walls with a large amount of elastic tissue and a smaller amount of smooth muscle to having walls with a smaller amount of elastic tissue and a relatively large amount of smooth muscle. Arterioles transport blood to capillaries which are the smallest blood vessels. Most of the exchange between the blood and interstitial spaces occurs through the walls of the capillaries. From the capillaries, blood goes into the venous system. [1]

3.1 Structure of blood vessels

Except for capillaries and venules, the walls of blood vessels consist of three distinct layers (figure 3.1), which are more evident in muscular arteries than in veins. Starting from the lumen

and moving toward the outer wall of the vessels, the layers, or tunics, are tunica intima, tunica media, and tunica adventitia, or outer tunic. The tunica intima consists of endothelium, a delicate connective tissue basement membrane, a thin layer of connective tissue called the lamina propria, and a fenestrated layer of elastic fibers called the internal elastic membrane. The tunica intima and the following layer, the tunica media, are separated by an internal elastic membrane. The tunica media, or middle layer, consists of smooth muscle cells arranged circularly around the blood vessel. The amount of blood flowing through a blood vessel can be regulated by contraction or relaxation of smooth muscle in the tunica media. A decrease in blood flow results from vasoconstriction, a decrease in blood vessel diameter caused by smooth muscle contraction, while an increase in blood flow is produced by vasodilation, an increase in vessel diameter due to smooth muscle relaxation. Depending on the size of the vessel, the tunica media also contains variable amounts of collagen and elastic fibers. Finally, the tunica adventitia is composed of connective tissue. The diameter and type of the blood vessel affect the relative thickness and composition of each layer. Compared with arteries, the walls of veins are thinner and contain less elastic tissue, fewer smooth muscle cells, and are less resistant in the radial direction. This is because veins are subject to less pressure forces than arteries. They turn out to be more deformable along the longitudinal section, however, to avoid probable occlusions due to the lower pressure that characterizes these vessels. Their walls increase in thickness as they project toward the heart. [1]

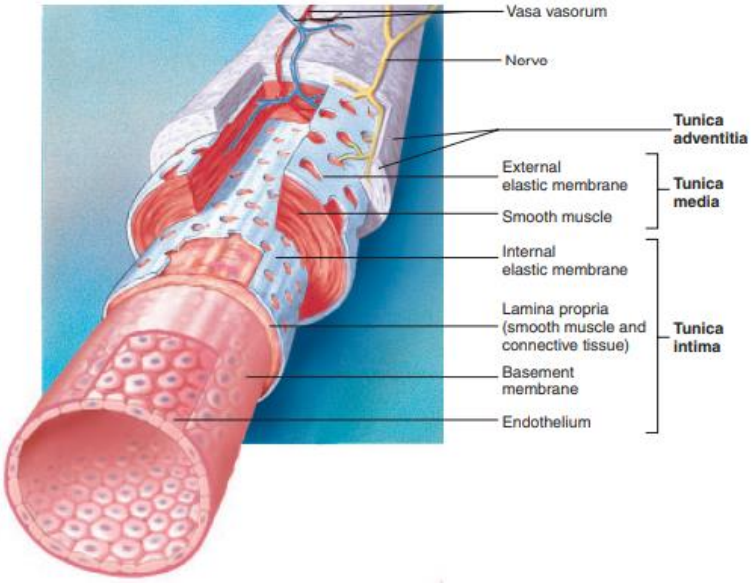

Figure 3.1: The image shows the histology of a Blood Vessel. The walls of blood vessels consist of three distinct layers: tunica intima, tunica media, and tunica adventitia. [1]

Changes in transmural pressure (P_{tm}), which is defined as the difference between the pressure inside and outside the vessel, are the main cause of sudden changes in vascular size for both arteries and veins. The relation between vascular size and P_{tm} is generally represented by a non-linear volume-pressure curve (figure 3.2), according to which vascular size increases as transmural pressure increases. Specifically, arteries are more rigid and exposed to larger

pressure variations than veins. Pressure changes in arteries are mainly determined by the pulsatile nature of the cardiac pump and they are also affected by peripheral resistances. On the other hand, veins are characterized by a much lower internal pressure, and therefore changes in P_{tm} are mainly influenced by changes in external pressure. However, it should be noted that intravascular pressure is also influenced by the intrinsic characteristics of the vessels, circulating blood volume, medication, and many other additional factors. The slope of the volume-pressure curve defines vessel compliance (C):

$$C = \frac{DV}{DP_{tm}} \tag{3.1}$$

The curve tends to flatten at high P_{tm}. A perturbation of P_{tm} would result in a corresponding change in vessel volume (DV) depending on vessel compliance. The same P_{tm} change will produces different size changes depending on vessel size, resting (mean) P_{tm} value and volume. If the average P_{tm} is low (as in veins) the size changes will be large, while with a higher P_{tm} value the vessel size will be larger and its phasic changes will be smaller.

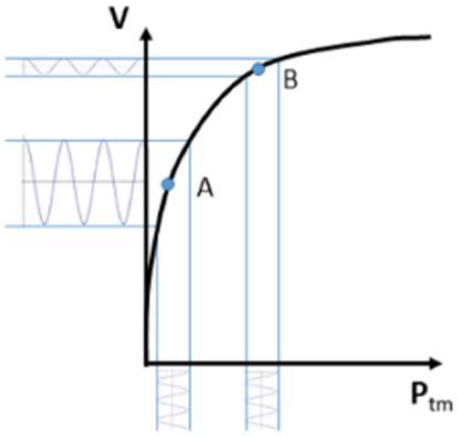

Figure 3.2: The figure shows the volume-pressure curve of a venous blood vessel representing the relationship between vessel size (volume, V) and P_{tm}. If Ptm is low (A; high vessel compliance) the size changes will be large, while if Ptm is high (B; low vessel compliance) the vessel size will be larger, and its phasic changes will be smaller. [3]

Extra-vascular compliance must also be considered when analyzing phasic changes in vascular size. Since blood vessels are embedded within other organs and tissues, their ability to expand because of changes in blood pressure also depends on the ability of extra-vascular tissues to accommodate such changes. In other words, when measuring changes in vessel volume in response to given variations in blood pressure, we are assessing the total compliance (C_{tot}), which accounts for the vascular (C_v) and extravascular (C_{ev}) compliances according to the formula:

$$c_{tot} = \frac{1}{\frac{1}{c_v} + \frac{1}{c_{ev}}} \tag{3.2}$$

C_{tot} resulting smaller than C_v. [3]

3.2 Inferior vena cava

The inferior vena cava (IVC) is a large vein that carries venous blood from the subdiaphragmatic areas of the body to the heart. It runs on the posterior wall of the abdomen to the right side of the aorta. It originates from the confluence of the two common iliac veins at the level of the sacral promontory. It then connects with the posterior aspect of the heart and, immediately after crossing the hepatic diaphragm, flows into the right atrium of the heart. Along its course, it receives numerous affluents, both parietal and visceral. The tunica intima of the large veins, as in the case of the IVC, is thin and consists of endothelial cells, a thin layer of connective tissue, and some scattered elastic fibers. The tunica media is also thin and consists of a thin layer of circularly arranged smooth muscle cells, collagen fibers, and a few scattered elastic fibers. The tunica adventitia is the predominant layer. [2]

The inferior vena cava is characterized by high compliance, i.e., a good ability to expand elastically under the effect of increasing blood pressure and then shrink by returning the accumulated blood volume under the effect of decreasing blood pressure. Compliance is a function of the elasticity of the vessel walls and, as mentioned above, is a measure of the relationships between pressure changes and volume changes. Given its good ability to dilate, the IVC readily changes its size in response to changes in transmural pressure. Pressure changes are regularly produced by respiratory activity and cardiac activity. Regarding cardiac activity, before the systole, movements of the valvular plane toward the apex create a strong suction within the atria. As a result, a rapid blood flow to the heart is generated and then a reduction in vessel diameter and pressure. Instead, a small part of the blood flow goes back during systole and causes dilation of the IVC. Regarding respiratory activity, in the condition of end thoracic exhalation in which the IVC exhibits its maximum size. During an inspiration the IVC undergoes a slight reduction in size, due to the decrease in intrathoracic pressure that increases venous return. Additionally, during inspiration, the diaphragm descends, abdominal pressure rises, and the sizes of the P_{tm} and IVC further decrease. [3] In addition, these pressure changes cause the IVC to move in both longitudinal and transverse planes during breathing.

It is important to note that any maneuver or pathological condition, which alters the pressure and volume of blood in the abdominal compartment, not only affects the size of the IVC but also the extent of the change in the size of that vessel. For this reason, the study of the size and pulsatility of the IVC is of particular interest in the clinical setting because it allows the evaluation of many critical conditions. It allows the assessment of cases of pulmonary fibrosis and cirrhosis, the extraction of information on right heart function, the patient's right atrial pressure (RAP) [4], [5], [6], the blood volume status of patients [7], and thus in fluid therapy (therapy that aims to improve oxygen delivery to tissues and increase systolic and cardiac output in patients with respiratory failure).

Possible pathologies of the inferior vena cava are cases of thrombosis or alterations in central venous pressure (CVP). Measurement of (CVP) is essential for a complete hemodynamic assessment of the patient. CVP is considered equivalent to atrial pressure (RAP) because the vena cava is continuous to the right atrium. Central venous catheterization is the gold standard of measurements of these pressures. However, this procedure is prone to possible complications such as infection, catheter-induced thrombosis, and arrhythmias, so the use of this routine is limited. [8] A reliable tool for estimating CVP is the inferior vena cava caliber assessment.

Chapter 4

Ultrasound

Technological development and the growing potential of computer computing have led to qualitative growth in imaging techniques. Ultrasound techniques have generated a change in the clinical and diagnostic approach to the patient. Ultrasonography has the great advantage of being a user-friendly technique because it is a non-invasive, simple, low-cost, and rapidly performed method. In addition, it is based on the use of ultrasound (US) and free of side effects for the patient. The main disadvantage of this technique is that it is "operator-dependent", the quality of the examination is closely related to the experience and skill of the operator who "constructs" and "interprets" the images in real-time. Other limitations of this method are the maximum depth of sound penetration, which is limited by scattering, and frequency-dependent absorption of US. For this reason, it is difficult to obtain clear images for examination in overweight patients. Ultrasound cannot be used to analyses structures covered by bone or gas because these elements have very high and very low acoustic impedance, respectively. [9]

4.1 Physics and principles of ultrasound

Ultrasound imaging is based on the physical and biological interaction properties of ultrasound. The image is generated by the signal reflected from various anatomical structures, which are characterized by a specific impedance, and scattering.

The US are mechanical vibrations, longitudinal elastic waves of rarefaction and compression, which propagate a variable speed depending on the medium of transmission; they cannot transmit in a vacuum. Such waves are described by the fundamental physical notations of wave mechanics: amplitude, intensity, wavelength, frequency, and propagation speed. Amplitude represents the maximum variation of the wave. Intensity is proportional to the square of amplitude and is generally expressed in decibels. The distance between each compression or rarefaction band represents the wavelength (λ), which is the distance travelled during a cycle or period. Frequency is the number of times the wave repeats per second and is expressed in hertz; it is the inverse of period. In diagnostic ultrasound frequencies ranging from 1.5 to 15 MHz are used; the frequency chosen influences the penetrating ability of the US. The propagation speed of US is not constant, but it varies depending on the transmission medium. In particular, the transmission speed depends on the inertia of the molecules to motion and the density of the medium. Specifically, the velocity of US in human liquids and tissues can be obtained from the equation:

$$v = \sqrt{\frac{E}{\rho}} \tag{4.1}$$

where E is the Young's modulus (elastic modulus) and ρ is the density of the material, expressed in kilogram per cubic meter. In most tissues, the velocity varies between 1500-1600 m/s. Precisely, the most likely value for biological tissues is about 1540 m/s, so ultrasound scanners are calibrated to this value.

Another material characteristic related to the speed of US propagation is the acoustic impedance (Z). It is defined as the product between the density of the medium and the speed of propagation in the medium itself.

$$Z = \rho \, \mathrm{v} \tag{4.2}$$

The table 4.1 shows the impedance values of the main tissues of the human body.

Medium	**Propagation speed (m/s)**	**Impedance (Rayl x 10^{-5})**
Vacuum	0	-
Air	330	0.0004
Fat	1450	1.38
Water	1480	1.48
Liver	1550	1.65
Kidney	1560	1.62
Blood	1570	1.61
Muscle	1580	1.70
Bone	4080	7.8
Media soft tissue	1540	1.63

Table 4.1: Propagation rate of US in air, water, and biological tissues. [9]

Acoustic impedance is fundamental to the formation of the ultrasound image because it conditions physical phenomena of reflection and scattering of US. The amplitude of the return

echo is proportional to the difference in acoustic impedance between two tissues. [9], [10] Consider the situation depicted in figure 4.1, where I represents the incident wave, R the reflected wave and T the transmitted wave. Supposing we have two mediums, the first one with acoustic impedance *Z1* and the second one with acoustic impedance *Z2*, at the interface between those two mediums there is a phenomenon similar to the one expressed by the Snell's law. This law states that if light passes through the interface of two different mediums, the ratio of the sines of the angles of incidence and refraction is equivalent to the ratio of velocities in the two media, or equivalent to the reciprocal of the ratio of the indices of refraction:

$$\frac{Sin(\theta_1)}{Sin(\theta_2)} = \frac{v_2}{v_1} = \frac{n_1}{n_2} \tag{4.3}$$

where θ_1 is the incidence angle, θ_2 is the transmitted angle, v_1 is the velocity in the first medium, v_2 is the velocity in the second medium, n_1 is the refraction index in the first medium and n_2 is the refraction index of the second medium.

Given the impedances of the two materials, it is possible to calculate the reflection coefficient (R) with the following equation:

$$R = \left(\frac{Z_2 - Z_1}{Z_2 + Z_1}\right)^2 \tag{4.4}$$

Anything which is not reflected, is transmitted, and the sum of the transmission coefficient and the reflection coefficient (T) must be equal one thus we have the following relation:

$$T = 1 - R \tag{4.5}$$

Since an ultrasound image is directly dependent from the reflection coefficient, it is possible that two different medium interfaces produce the same reflection coefficient, and by consequence, the same image. Therefore, it is not possible to distinguish a type of tissue simply by looking at tonality of grey on the image. The clinician requires an extensive formation to know exactly what an ultrasound image represents. [11], [12]

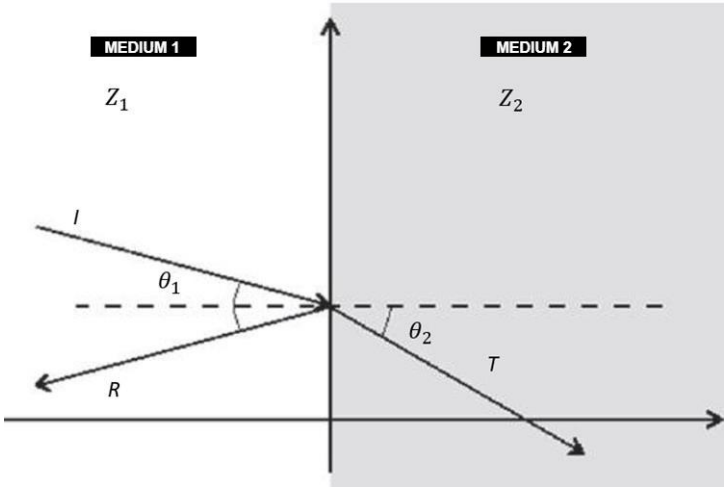

Figure 4.1: The figure shows two media with different acoustic impedance, I represents the incident wave, R the reflected wave and T the transmitted wave. The ratio of the sines of the angles of incidence θ_1 and refraction θ_2 is equivalent to the ratio of the velocities in the two media.

Many of the echoes, that form the image, come from small, irregular interfaces in the parenchyma of organs (smaller than wavelength size); this is the phenomenon of scattering, or dispersion of echoes. These echoes help to form the image of the eco structure of organ parenchyma, but they may not accurately represent the actual anatomy, macro or microscopic of the organs.

The ultrasound beam is transmitted through the body in the form of acoustic energy, described as intensity or power. The term attenuation describes the loss of acoustic energy that occurs when sound passes through tissues. Similarly, reflected echoes toward the probe are also attenuated. The attenuation of sound, like its intensity or power, is generally measured in decibel and is directly proportional to the frequency of the ultrasound beam. The factors that contribute to attenuation are absorption, reflection, and scattering. Absorption is the conversion of the acoustic energy of a sound pulse into heat. It is a phenomenon mainly due to friction between the wave passing through and the molecules of the tissue passing through. Heat production within tissues becomes important when evaluating the biological effects and safety of ultrasound use. [10]

4.2 Tools of an ultrasound equipment

All ultrasound equipment consists of a few basic components (figure 4.2): a probe, which typically plays a dual role of both emitting and receiving echoes, an ultrasound generator that stimulates and drives the piezoelectric crystals, and a receiving circuit consisting of an acoustic demodulator, which goes to search for a pulse of known frequency within the noise. [9] Due to the phenomenon of absorption, the amplitude of the echo returning to the probe is smaller than the amplitude of the emitted pulse. For this reason, a time gain compensation (TGC) filter is inserted, which compensates the amplitude of the received signal with a gain proportional to the time elapsed between pulse emission and the reception of the return echo. The TGC block

separates the two phenomena that cause the decrease of echo amplitude (tissue attenuation and reflection coefficient), since the only useful information for imaging is the reflection coefficient. The return echoes are processed to create the image visible on the monitor. [13]

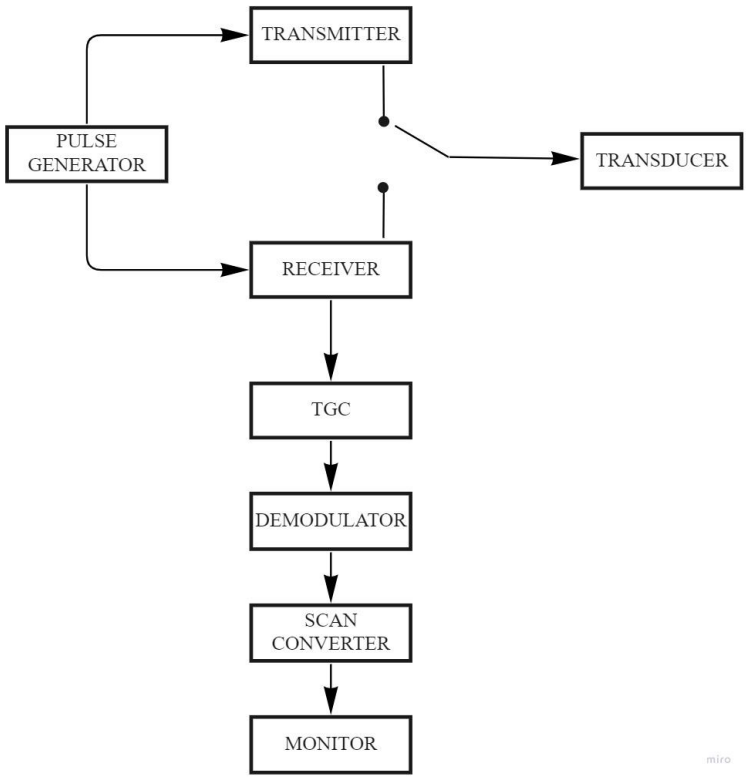

Figure 4.2 The figure represents the block diagram of an ultrasound scanner. The main components such as the pulse generator, transmitter, receiver, TGC and probe are shown.

4.2.1 Pulse generator

The pulse generator sends synchronized high-voltage pulses to piezoelectric crystals inside the probe, which in turn transmit short ultrasound emissions to the patient. The pulse length, dependent on the frequency of the probe, determines the axial resolution and usually it varies between 0.1-1.1 mm. The interval between two pulses must be long enough for the return echoes to reach the transducer before the next pulse is delivered. The pulse generator allows the pulse repetition frequency (PRF) to be adjusted.

In the specific case of Doppler ultrasound, in addition to the pulsed emission mode, it is possible to stimulate the crystals in a continuous mode. In this technique, the probe emits a continuous acoustic wave, and one part of the crystals is used only in emission while the other part is used only in reception. [10]

4.2.2 Probe

The probe, or transducer, is the central element of ultrasound equipment. In general, a transducer is a device capable of converting one form of energy into another. Ultrasound probes convert electrical current into ultrasound, and vice versa. The main components of the transducer are the piezoelectric crystals, the damping layer, and the matching layer.

Piezoelectric crystals are elements that, when deformed by mechanical stress, generate electrical charges and thus a measurable potential difference. This is known as the direct piezoelectric effect. At the same time, applying a potential difference to the faces of these sensors generates a mechanical deformation of the crystal. This is known as the inverse piezoelectric effect. The behavior of piezoelectric ceramics explains their dual function: when they are stressed by current, they deform, and generate US; conversely, when they are affected by echo feedback signals, i.e., mechanical vibrations, they generate electrical signals. Lead zirconate titanate (PTZ) is the most used ceramic for the construction of ultrasound probes. The transmission frequency depends on the electrostatic coefficient of the piezoelectric ceramic. Frequency and geometry define the fundamental characteristics of the probe. Multi-element probes consist of a variable number of ceramic columns. On the other hand, single-element transducers consist of a single piezoelectric element in the form of a flat circular disc and are generally not widely used.

Another important element of the probe is the damping layer. When it is stimulated by the generator, the transducer vibrates at its resonance frequency and generates US at the characteristic frequency. As explained later, the axial resolution of the crystals improves with shorter stimulation pulses. The duration can be reduced by damping the transducer vibration as quickly as possible after each electrical excitation. This is achieved by placing an epoxy resin layer behind the crystal plane that absorbs vibrations and their redundancy. The damping material must have two characteristics. First, it must have an acoustic impedance close to that of the piezoelectric element, this reduces the possibility of reflection at the transducer-damping material interface and thus reverberation on the rear surface of the crystals. Secondly, it must absorb US transmitted into it from the rear surface of the crystals.

Finally, the matching layer has the function of reducing US reflection at the interface between transducer and skin. For this reason, it has an impedance value intermediate between that of piezoelectric ceramics and that of tissue. The acoustic impedance of crystals is approximately 20 times greater than that of soft tissue, without this layer this difference would result in the reflection of approximately 80% of the sound energy emitted by the transducer. The US reflected by the skin would bounce off the crystals, generating redundancy and new spurious impulses. The matching layer must also respect two fundamental characteristics. It must have an impedance value intermediate between the impedance of the active elements and that of the soft tissue and a thickness equal to a quarter of the wavelength. [9]

4.2.2.1 Probe types

Most modern ultrasound devices use multi-element probes, consisting of up to hundreds of rods. This makes it possible to construct transducers of different formats according to the fields of application [9].

- Linear probes: in this case the probe has a bar shape and contains crystals inside that are arranged in a line. They are available in different sizes and frequency ranges, between 7.5 and 12 MHz. These probes offer the highest available frequency, the best possible resolution, and are used primarily for surface ultrasound. They have the disadvantage of requiring a large contact area with the skin, so they are not suitable for sub-sternal or intercostal ultrasound.
- Covex and micro-convex: they are linear probes with convex curvature. Convex probes are available in a variety of sizes and transmission frequencies, ranging from 2.5 to 3.5 MHz, they allow targeted focusing. Micro-convex probes have a small radius of curvature, a frequency range of 3 to 9 MHz, and are characterized by a very small contact surface area.
- Phased array: these probes align piezoelectric crystals in a band or rectangle configuration, creating a sectoral image. They are ideal in cardiology because, having a very high frame rate, they allow objective assessment in patients with a high heart rate. In addition, having a minimal contact surface they are suitable for intercostal spaces. A state-of-the-art echocardiography ultrasound equipment should have three phased array probes available, with frequencies ranging from 2 to 3 MHz, 5 to 7 MHz, and 10 MHz or higher for smaller patients.

4.2.3 Receiver

When the piezoelectric crystals inside the probe meet the acoustic pressure waves of the return echoes, low voltages are produced. These electrical signals are processed by the computer (the receiver), ultimately creating a diagnostic image. The manipulation of these weak electrical signals, to create the best possible image through the selection of the various controls of the ultrasound scanner, is largely up to the operator. [10]

4.3 Spatial resolution and ultrasound beam focusing

One of the main requirements in ultrasound imaging is spatial resolution. Resolution is the minimum distance by which two targets generating different echo signals can be distinguished from each other. In a 2-D ultrasound image, there are two axes of resolution: lateral resolution, which describes the resolution of the system with respect to an axis perpendicular to the US beam, and axial resolution, which defines the resolution along the beam axis. To improve axial resolution, the spatial pulse length (SPL) must be decreased. If two targets are less than half the SPL, they will be shown overlapping in the image. To decrease the SPL, either the λ or the number of pulse cycles (N) must be reduced, because the SPL is the product of N and λ.

Therefore, to improve axial resolution, the transmission frequency must be increased, at the expense of penetration capacity. On the other hand, to improve lateral resolution, the frequency emitted by the crystal must be increased, thereby reducing the beam width.

Spatial resolution also depends on the sound field. In the multi-element transducer, each crystal is a source of small wavefront. The US beam emerging from the transducer represents a unique wavefront that is generated by interference, phenomenon for which if two sound waves generated by two different sources meet in a region of space during propagation, they can give rise to constructive or destructive interference. The unfocused US beam is unusable in diagnostics because it tends to progressively diverge and lose lateral resolution. The sound field (figure 4.3) is generally divided into two regions: near field (Fresnel zone) and far field (Fraunhofer zone). The near field has a cylindrical shape and shows a linear progression, here the beam has maximum lateral resolution. The length of this zone is directly proportional to the diameter of the crystal and inversely proportional to the frequency of the wave. On the other hand, the far field tends to diverge by an angle dependent on λ and the diameter of the transducer, in this zone the resolution becomes much worse.

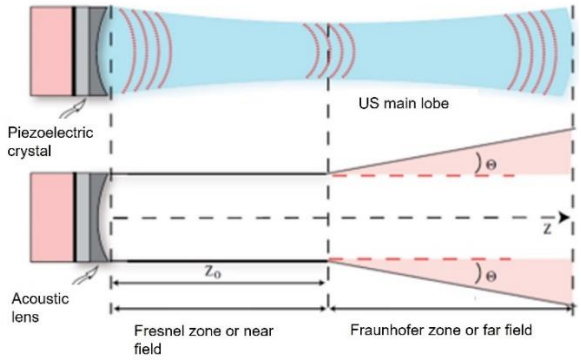

Figure 4.3: The image shows the division of the sound field (Z) into two regions, near field or Fresnel zone (Z_0) and far field or Fraunhofer zone. [9]

To improve spatial resolution, the natural divergence of the beam must be reduced by focusing (figure 4.4). The zone of maximum focusing is called the focal area while the point of maximum collimation is called the focus. In the focal zone the beam has less width and less thickness and, consequently, maximum acoustic intensity. Before the focus the beam tends to converge, after the focus it diverges. The focal zone is delimited by the points where the diameter of the beam is twice as large as the diameter of the focal point. On the other hand, the focal distance is the distance between the focus and the transducer surface and is the area of the sound field where axial and lateral resolution is greatest.

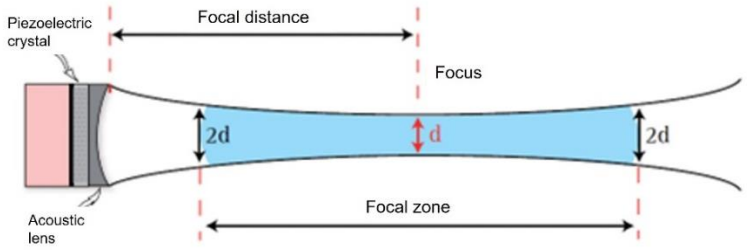

Figure 4.4: The figure represents the focal zone is the area of maximum focus, while the focus is the point of maximum collimation. In the focal zone, the beam has less width and less thickness and, consequently, maximum acoustic intensity. The focal distance is the distance between the focus and the transducer surface and is the air of the sound field where axial and lateral resolution is maximum. [9]

Beam focusing can be achieved with different techniques: mechanical focusing and dynamic focusing. Mechanical focusing was mostly used in older ultrasound instruments. It reduces the natural divergence of the US beam with acoustic lenses that converge the beam to a focal point. The same result can be achieved with the use of concave piezoelectric crystals, this is called intrinsic mechanical focusing. The choice between these two techniques depends on the probe and the clinical application. Intrinsic focusing cannot be used in probes with a nominal transmission frequency greater than 5 MHz (because the fragility of crystals less than 4 mm thick makes shaping impossible), while the lenses have an invariable focal length. Dynamic focusing uses electronic circuits that regulate the delay of individual crystals' excitation. Specifically, the outermost elements are excited first and their wave fronts have the longest time to propagate. The innermost crystals are excited with a slight delay. This generates a single wave front, with a curvilinear profile, which propagates towards the focal area. This technique is based on the interference phenomenon. The final effect is the same as with acoustic lenses, however, in this case, by acting on the delays, it is possible to vary the focal distance. Figure 4.5 shows an example of electronic focusing, in A the delay between the stimuli is smaller than in B, so the focal distance is greater.

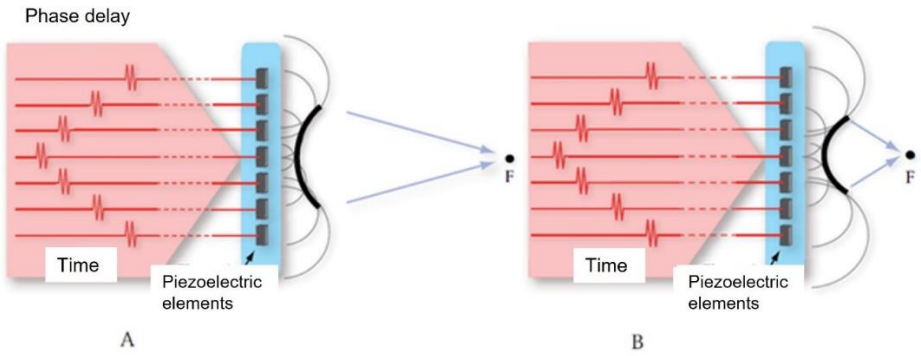

Figure 4.5: The figure represents an example of electronic focusing, in A the phase delay between stimuli is less than in B, so the focal distance is greater. [9]

During the ultrasound acquisition, it is also possible to choose the number of focuses. The pattern of the sound beam in the two cases is shown in figure 4.6. [9]

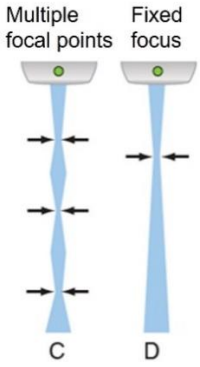

Figure 4.6: The figure shows the pattern of the sound beam in the case of multiple focal points (C) and in the case of fixed focus (D). [9]

Conventional US imaging consists of scanning line by line the imaging plane with focused beams as shown in figure 4.7. [14]

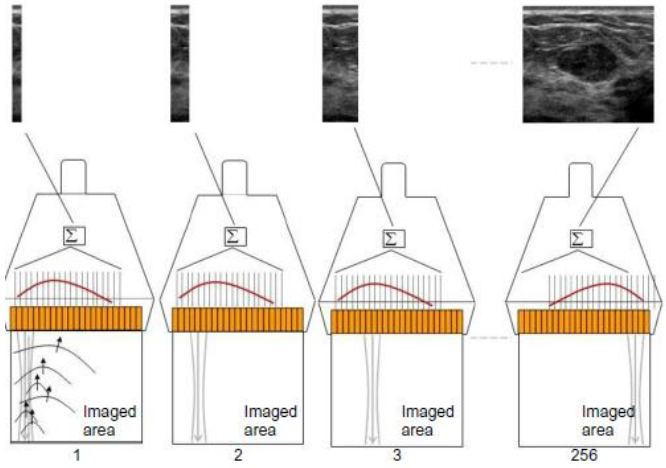

Figure 4.7: Complete image reconstruction by line-by-line scanning of the plane using several focused beams. [15]

4.4 Return echoes display mode

Ultrasound data can be displayed in different modes with the ultrasound scanner. [16], [10] There are four main strategies used:

- A-Mode (Amplitude mode). This is the simplest display mode, which is no longer widely used today; depth signals are recorded as spikes on a graph. The vertical axis (y) of the display shows the echo amplitude, and the horizontal axis (x) shows the depth in the patient. The depth is calculated from the time between transmission and return of the echo.
- B-Mode (Brightness Mode). This mode is typically used in diagnostics; signals are shown as two-dimensional anatomical images. Each pixel in the image has a brightness that is proportional to the amplitude of the echo returned. B-mode is often used to

evaluate the developing fetus and to examine organs, including the liver, spleen, kidneys, thyroid, testes, breasts, uterus, ovaries, and prostate. It is a modality that shows movement quickly in real-time. Real-time imaging provides both anatomical and functional information.

- M-Mode (Motion Mode). This mode is used to visualize moving structures. Signals reflected structures are converted into waves that are shown continuously along the vertical axis. Again, then, there is an output graph in which depth (vertical axis) versus time (horizontal axis) is represented. M-mode is used primarily for fetal heart rate determination and in cardiac imaging, especially for evaluation of valvular disorders, and is usually used in conjunction with B-mode.
- Imaging Biplane. This is a newly developed visualization mode that allows the operator to view both the transverse and longitudinal planes simultaneously. It has been incorporated into many new ultrasound devices and is particularly interesting for the study of blood vessels. [17]

4.5 Artifacts in ultrasound images

The operation of ultrasound scanners is based on four basic principles: the ultrasound must travel in a straight line, at a constant speed; return echoes originate only from objects located along the main axis of the ultrasound beam; and, finally, the intensity of the echo depends on the tissue from which the echo originates. When one of these elements is not respected, artifacts are generated. The following are the main artifacts that can be found in ultrasound images. [9]

- Lateral lobe: is produced by minor ultrasound beams that do not travel along the primary beam axis and produce ghost echoes in the image. When these beams interact with a highly reflective interface back to the probe, the returning echoes are misplaced in the image, even though they did not originate from the main ultrasound beam and generate the artifact in question.
- Slice thickness: in this case phantom echoes are produced within the image. However, slice thickness occurs when part of the US beam thickness straddles the wall of a cystic structure, that is, a cavity surrounded by a membrane and containing a liquid material. In fact, in these cases it happens that part of the beam goes inside the structure and part outside. The echoes arising from this part of the beam appear erroneously on the image inside the structure.
- Reverberation: is formed when the ultrasound beam repeatedly bounces between two highly reflective surfaces. The ultrasound in this case is bounced back and forth creating multiple echoes from a single pulse.
- Comet tail: this is an easily recognizable artifact on the image because it is formed by a series of small, discrete, and very bright close-range echoes. These are created when, in a narrow area, there are several interfaces characterized by very different acoustic impedances.

- Ring down: this type of artifact is generated by the interface of a small portion of liquid trapped between a layer of small gas bubbles. This structure behaves similarly to a piezoelectric crystal and generates a primary beam that radiates deeply.
- Mirror artifact: This is generated in the presence of large and curved reflective surfaces, such as the diaphragm-lung interface. In these cases, in fact, part of the ultrasound beam is reflected, and when the echo returns to the probe, artifacts are generated.
- Refraction: as already clarified, refraction is a phenomenon that normally occurs during the interaction between US and tissues, however, this can also produce artifacts. In the case where the sound wave passes through multiple tissues with different impedance, the wave transmitted to the second tissue will have a different direction, this can cause a reflector element to be displayed incorrectly on the monitor.
- Posterior shadow cone: manifests as an area of low-amplitude echoes that is deeper than very attenuating structures. This artifact is caused by the presence of gas or bone tissue; in the case of gas, the US waves are almost completely reflected; conversely, with bone tissue, the beam is almost completely absorbed. In both cases, an acoustic shadow is generated on the image.
- Lateral acoustic shadows: in these cases, an acoustic shadow is created away from the lateral edges of a cystic structure. This phenomenon is due to the lower propagation speed of ultrasound in a liquid-filled structure that reflects the beam at the liquid-tissue interface.
- Posterior wall reinforcement (enhancement): is characterized by a localized increase in echo amplitude that occurs distal to structures that attenuate the incident beam less. This artifact is useful in distinguishing cystic structures from hypoechogenic solid masses.

4.6 Ultrafast ultrasound

Recently, ultrafast scanners have been developed that make ultrasound recordings with high temporal resolution. Whereas classic ultrasound works at less than 100 fps, ultrafast ultrasound can achieve values of several thousand. This “ultra-fast” imaging is based on reconstructing the image from a single transmission and reception event, as opposed to traditional imaging where the plane is scanned line by line with focused beams. These scanners transmit unfocused acoustic waves, i.e., plane waves, which identically soundproof the entire region of interest (ROI). This innovation represents a major change in medical ultrasound. In a single transmission event, they scan the entire ROI achieving a significant increase in frame rate. However, reconstructing an image with a single transmission would decrease image qualities, especially resolution and contrast. This is because the reflection signal comes from the entire imaging plane rather than from a single thin acoustic line. To achieve focused transmission and improve image quality, plane waves of different angles can be coherently combined. This process is known as synthetic imaging and exploits plane-wave compounding. [18] Compounding is an image optimization tool that combines multiple images from multiple aperture positions (spatial compounding) or multiple transmission frequencies (frequency compounding) into a single frame composed in real time. Plane-wave compounding provides

the image of an entire ROI for each ultrasonic transmission, using all elements of the array. This generates a high amplitude signal and makes it possible to construct high-quality ultrasound images with a limited number of plane waves. In this way, tissue and blood movement can be studied with frame rates in the kilohertz range. [14] Figure 4.8 shows an example of reconstruction in which three wave planes are used and approximately 3200 fps are obtained. The compromise between frame rate and image quality depends on the number of transmissions used to reconstruct the synthetic image. The transmissions in each case affect each image pixel almost identically, whereas in conventional ultrasound imaging the transmission is only optimal at the focal depth level. [15]

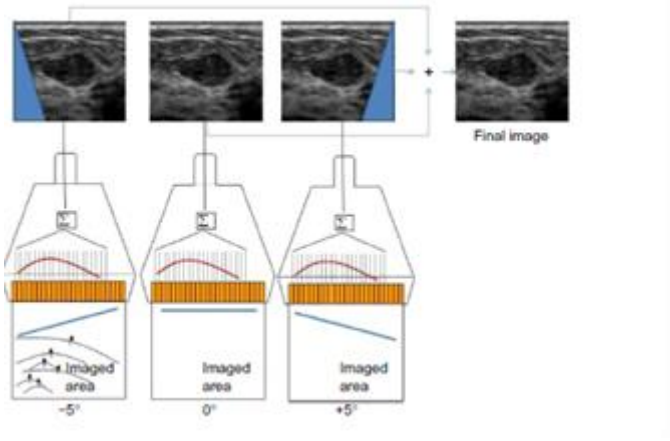

Figure 4.8: The figure represents an example ultrasound image reconstruction in three wave planes. [15]

4.7 Doppler effect in ultrasonography

Doppler ultrasound is used to detect the presence of blood flow within vessels, its direction, speed, and character. The Doppler effect is the change of the frequency of sound when the sound waves are reflected from moving targets, usually red blood cells. If the motion occurs toward the probe, the frequency of the returning echoes is greater than that of the transmitted sound (positive shift). If the motion occurs away from the probe, the echoes have a lower frequency than the transmitted sound (negative shift) The difference between the transmitted and received frequency is called the Doppler frequency, or Doppler shift, and is proportional to the velocity of the target. The definition of the Doppler frequency (f_d) is given below:

$$f_d = \frac{2f_0 v}{c} \cos\theta \tag{4.6}$$

where f_0 is the initial frequency of the US wave, v is the velocity of the erythrocytes, θ is the angle formed between the probe scan line and the direction of propagation of the erythrocytes and c is the velocity of US propagation in the tissue. The f_d can take positive or negative value depending on whether the flow is approaching or receding and f_0 is then added to or subtracted from as appropriate. From the above equation, the reflector velocity (v) can be derived:

$$v = \frac{f_d\, c}{(2f_0\, \cos\theta)} \tag{4.7}$$

In the case where θ is equal to 90°, velocity cannot be measured. Normally, the values of angle θ should be between 40° and 60°. Therefore, if a reflected sound wave has a lower frequency than the transmitted sound wave, the blood flow will move away from the transducer. If a reflected sound wave has a higher frequency than the transmitted sound wave, the blood flow moves closer. The magnitude of the frequency change is proportional to the speed of the blood flow, it is usually in the kilohertz range and audible when transmitted to the ultrasound speaker. Changes in the frequency of reflected sound waves are converted into images showing the direction and speed of blood flow. [16], [10] Echo doppler is also used to assess:

- The vasculature of tumors and organs.
- Cardiac function.
- Occlusion and stenosis of blood vessels.
- Blood clots in blood vessels.

Chapter 5

Applications of IVC ultrasound in fluid therapy and emergency room

5.1 Fluid therapy

Intravascular volume status is the total blood volume of an organism and includes both the blood circulating in the blood vessels and the blood stored in organs such as liver or spleen. It is a relevant cardiovascular factor related to cardiac preload, which in turn affects cardiac output and blood pressure. Its evaluation in patients in critical condition, admitted to the intensive care unit (ICU) or undergoing major surgery is essential. Indeed, these individuals often have inadequate tissue oxygen supply caused by insufficient circulating blood volume. A clinical example where the study of volume status is crucial is heart failure. In this case, fluid overload is generated and management with diuretics is very delicate and subjective. Similar considerations apply to patients with renal failure undergoing dialysis, for whom continuous and automatic monitoring of IVC can help to adapt the dialysis process according to the patient's current volume status. Under these conditions, rapid volume expansion via intravenous fluid administration should optimize tissue perfusion but such benefit is not without risks. The hypervolemia due to a liberal fluid administration strategy causes tissue edema or lung edema and worsens patient outcome. Otherwise, insufficient fluid administration due to a restrictive fluid therapy strategy can perpetuate hypovolemia, poor tissue perfusion and increase the rate of complications such as renal failure and death. In the medical field the fluid therapy aims to increase systolic volume (SV) and consequently improve cardiac output and oxygen transport to tissues. This technique appears to reduce patient mortality, duration of stay in the ICU and duration of medical ventilation. However, there is not a gold standard for estimating the exact amount of fluid a patient needs and it has been shown that in 50% of patients this technique does not work. This could be due to the composition of the blood volume. Blood volume consists of 70% unstressed volume (Vu) and of 30% stressed volume (Vs). Vu is the blood volume that does not influence transmural pressure. Vs is the blood volume that stretches the vessel walls, effectively increasing transmural pressure and is the major determinant of venous return (VR). The effects of fluid therapy may be the result of an unpredictable distribution of the infused fluid between the Vs and Vu. Particularly, if the fluids are distributed mainly to Vu there will be no increase in VR, SV, and CO. Conversely, as Vs increases, transmural pressure increase and thus VR, SV, and CO increase. [19]

To make the correct clinical choice, the patient's responsiveness to a change in blood volume must be assessed. The Frank-Starling curve defines the relationship between preload and systolic volume. Figure 5.1 shows the expected increase in systolic volume after administration of fluids in patients under invasive mechanical ventilation. In addition, the picture shows the relationship of the curve with the variation of inferior vena cava diameter. The increase in

systolic volume depends on cardiac function and the initial preload. In the first case (A), is shown the Frank-Starling curve of a patient with normal cardiac function in which the results of fluid administration only depend on the initial preload: if the preload is low (rising phase of the curve) the systolic volume significantly increases even for small changes in preload. When CO increases more than 10-15%, the patient is considered a responder, i.e., responsive to volume change. This corresponds to a significant variation in the diameter of the inferior vena cava with the application of positive pressure to the thorax during inspiration in the ventilated patient. If the preload is elevated (flat phase of the curve), then no significant increase in systolic volume is observed. When CO increases less than 10-15%, the patient is considered a no responder. This situation leading to pulmonary overload which corresponds to an inferior vena cava with little distension. Second example (B) shows the Frank-Starling curve of a patient with decreased cardiac function. In this case, the administration of fluids, even with low initial preload, may result in pulmonary fluid overload without a significant increase in systolic volume. [20]

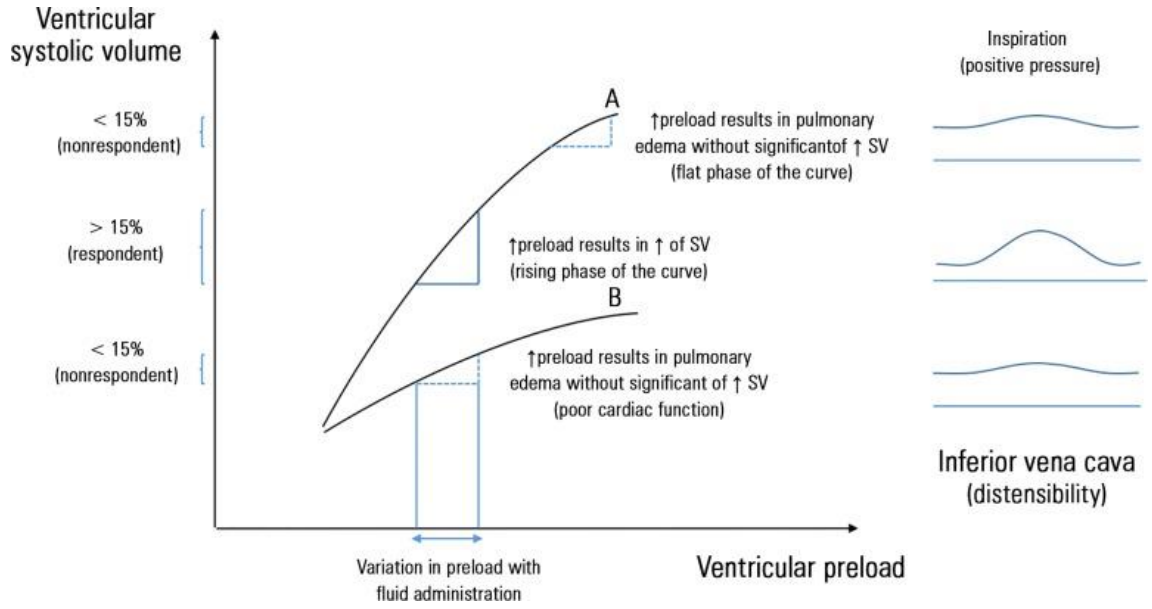

Figure 5.1: The image shows the Frank-Starling curve and its relationship with inferior vena cava variation among patients under invasive mechanical ventilation. [20]

It is evident that the fluid response of patients is not linear but depends on the contractile capacity of the myocardium. This capacity cannot be measured directly, nor can the configuration of each patient's Frank-Starling curve be predicted. Therefore, the estimation of a patient's response to volume changes is not so easy. In clinical practice, no standard reference has been defined for assessing fluid responsiveness. There are several methods for changing the volume status of a patient, each with its own limitations. [19]

- One of these methods is the fluid challenge, which involves injecting an amount of intravenous fluid and evaluating the resulting changes in SV and CO. The response is compared with the Frack-Starling curve.

- The fluid challenge may carry some risk of hypervolemia, for this reason a mini-fluid challenge technique is often used. It is based on the administration of smaller fluid volumes at a faster rate. Mini-fluid challenge has been shown to reliably predict fluid responsiveness status in the operating room and ICU.
- The passive leg raising test is a less invasive test in which no fluid injection is involved. This test shifts blood volume from the lower limbs to the thoracic area, increasing venous return and preload. In this way, the change in CO can be directly assessed and compared with the Frack-Starling curve.
- Another method is based on mechanical ventilation that changes the cardiac preload. The physiological principle behind it is the lung-heart interaction and no fluid injection is involved. Because preload changes induced by controlled ventilation cause greater SV changes in patients positioned in the descending part of the Frank-Starling curve, it is possible to identify those who respond to volume increase if these changes exceed a certain threshold [20]. The main problem with this method is that although it is effective in predicting responsiveness, it requires patients to be on mechanical ventilation in the absence of cardiac arrhythmias and spontaneous breathing efforts; these limitations hinder its use in clinical practice. [19]

After changing the volume status, the patient's response needs to be assessed to identify a predisposition for therapy. Even in this case, several methods can be exploited, some of which based on imaging techniques. [19]

- Indicator Dilution Cardiac Output Techniques: are the most accurate techniques for estimating CO, independent of operator skill. However, they are invasive, difficult to use, and do not provide continuous index values. Impractical in emergencies or for routine testing.
- Pulse Contour Analysis Cardiac Output Techniques: these methods provide continuous and real time estimation of CO and SV. The main limitation is the poor ability to track changes in CO during conditions of hemodynamic instability associated with changes in systemic vascular resistance.
- Pulse Wave Transit Time: is another recently developed technique that provides continuous, non-invasive CO estimations. However, studies have shown that this method has an unacceptable agreement with Indicator Dilution Cardiac Output Techniques.
- Echocardiography: allows the estimation of intravascular volume status through the size of the ventricles, systolic volume, and/or CO. Therefore, it provides the assessment of fluid responsiveness. This technique is accurate and precise. However, the measurements are sensitive to the presence of arrhythmias, heart valve defects, and are dependent on the experience and skill of the operator.
- Point Of Care Ultrasound (POCUS): it is a protocol performed at the patient's bedside and useful in the emergency room. IVC POCUS helps to estimate intravascular volume

status by focusing on vein diameter and collapsibility. It is a non-invasive, validated and commonly used method for the assessment of volume status. [21]

5.2 IVC in fluid therapy

The assessment of IVC using transthoracic echocardiography is a conventional element of the echocardiographic study of critical patients. The physiological principle behind it is the lung-heart interaction. The variation in transpulmonary pressure during respiration is transmitted to the right heart cavities, which varies the venous return and the IVC diameter. This relationship depends on the ventilatory mode and IVC compliance of the patient. Patients who are not ventilated or those who are under invasive mechanical ventilation (IMV) with respiratory effort have a negative transpulmonary pressure at the beginning of inspiration that causes different levels of IVC collapse depending on the compliance of the vessel. For example, IVC shows low compliance and restricted collapse because of the transmitted negative transpulmonary pressure in individuals with high right heart cavity pressure or elevated preload (during the flat period of the Frank-Starling curve). Collapse may even be nonexistent in these patients. In patients with low right heart cavity pressure in hypovolemia (the ascending phase of the Frank-Starling curve), IVC compliance is high and inspiration-induced collapse is considerable. On the other hand, in patients receiving IMV without respiratory effort (in the controlled mode), positive pressure can be applied to the thorax during inspiration. This pressure is transmitted to the right heart cavities and the IVC, which expands depending on its compliance. In patients without cardiac reserve due to poor cardiac function and/or high preload (during the flat phase of the Frank-Starling curve), the IVC has reduced compliance and minimal distention, and its diameter may not change. In contrast, patients with cardiac reserve who might benefit from fluid therapy exhibit considerable IVC distension during inspiration. A diameter greater than 25 mm is common during states of high blood volume and predicts a low probability of fluid responsiveness, whereas an IVC diameter less than 10 mm is frequent at low blood volume levels, which suggests a higher possibility of response. [20]

IVC makes it possible to evaluate the potential benefit of fluid administration in relation to vascular compliance. However, this method has only demonstrated predictive usefulness in a particular population of patients: those undergoing invasive mechanical ventilation in a controlled mode (without respiratory effort).

The results of numerous studies that have examined the accuracy of IVC pulsatility in predicting a subject's responsiveness are inconsistent. This might be related to the fact that the estimation of IVC diameter with M-mode ultrasonography is not so easy and is subject to many errors. However, a recent study [7] evaluated variations in the inferior vena cava with new algorithms that correct estimation errors. Thus, the possibility of classifying patients as having hypervolemia or hypovolemia by means of indices extracted from ultrasound images of the IVC, along both the longitudinal and transverse planes, was evaluated. Several Binary Tree Models (BTMs) were developed in the study considering all possible combinations of outputs that could be derived from the algorithms. The model with the smallest regression mean square

error was then chosen. The best classifier was found to have 78% accuracy in predicting the volume status of patients, higher than the accuracy obtained using the standard clinical M-mode method.

5.3 IVC in emergency department

The overcrowding phenomenon of emergency department (ED) is a global issue. Numerous studies have examined the negative impacts of overcrowding and ways to address them. One way is to predict patient's prognosis early and quickly provide appropriate treatment to guarantee a larger chance of success. A very important element in this respect is the hydration status of the patient. In fact, a common risk factor for several diseases and clinical conditions is dehydration, defined as the loss of total body water contents. Early identification of dehydration in patients is associated with shorter length of hospital stay and reduce the mortality. As already mentioned, ultrasound monitoring of the inferior vena cava is a rapid and non-invasive method of assessing a patient's body fluids, making it extremely useful in emergency department. This examination can also be performed by operators with limited echocardiographic experience, in a crowded outpatient clinic and using portable devices. [22] Ultrasonography of the IVC also allows central venous pressure (CVP) and right atrial pressure (RAP) to be estimated. The right atrial pressure may contribute to the evaluation of dyspneic patients by helping to distinguish cardiac heart failure and non-cardiac causes of dyspnea. RAP is useful for the treatment of many diseases, especially in patients with heart failure or pulmonary hypertension. [23] In the emergency room, accurate and rapid assessment of this index provides significant clinical benefits.

Chapter 6

Assessment of the IVC pulsatility

The clinical information obtainable from the study of inferior vena cava pulsatility has already been listed. Ultrasound imaging of the inferior vena cava is increasingly employed, although it is subject to estimation errors. These errors are due to vessel movements generated by respiratory activity and affect both the transverse plane of the vein and the longitudinal plane, although they are generally appreciable only on the longitudinal axis. To avoid breathing-related movements, in some studies the recordings were performed on patients maintaining a short apnea, thus limiting analysis of oscillations to the cardiac component. However, it is not always possible to require the patient to maintain a state of apnea. Moreover, breathing-related diameter changes are correlated with the state of blood volume, and it is often of interest to know about them.

The "traditional" non-invasive method for continuous diameter measurement is based on M-mode ultrasound imaging, which is subject to motion artifacts. The standard clinical index of IVC pulsatility is the “Caval Index” (*CI*), which reflects changes in vessel diameter during the respiratory cycle, and is defined below:

$$CI = \frac{\max(D) - \min(D)}{\max(D)} \tag{6.1}$$

where *D* is the estimated diameter of the ICV. [24] Both B-mode and M-mode US scans showed major problems due to the lack of standardization and to the subjectivity of the measurement. Both modes are followed by a subjective identification of the IVC maximal and minimal diameters measured at the end of the expiration and inhalation phases respectively. The main problem with the M-mode technique is that it scans along a fixed direction. Therefore, it cannot consistently refer to the same section of the IVC as the vessel moves with respiration. So, the diameter measurements will be taken at different points of the vessel, thus introducing an error in the estimate. This error may also be related to the fact that the pulsatility of the vessel is not uniform along the longitudinal section and the diameter may vary from point to point. The IVC cross-sectional can also be irregular, very different from a circle or ellipsoid with a large variation of pulsatility in different directions. However, the measurement of diameters in B-mode is still operator-dependent because the expert, in addition to choose the frames corresponding to the end of inspiration and exhalation, must choose the sections along which to estimate vein size. For these reasons, it is difficult to make uniform recommendations and standardize the measurement method. One idea would be to study the IVC in both long and short axis views and average across the different sections or directions, it could be important to better characterize the vessel and its respirophasic dynamics. [7] Another important consideration is that CI is also strongly influenced by cardiac pulsatility. The cardiac component

(CCI) and the respiratory component (RCI) of IVC pulsatility could be easily separated, based on their different frequency contents, and independently analyzed. A study [25] showed that the ICC is modulated by respiratory activity, which negatively affects its reliability. By averaging the CCI obtained over separate respiratory cycles it is possible to eliminate respiratory modulation and obtain an index characterized by low variability. [25]

The following paragraphs discuss the functionality of new algorithms developed for a more reliable IVC analysis.

6.1 Semi-automated method in the longitudinal plane

In a first study [24], an algorithm was developed by a start-up, Vein Image Processing for Edge Rendering (VIPER), to estimate the CI index along the longitudinal axis from B-mode ultrasound images. It is a semi-automatic algorithm as it requires partial interaction with the user. At the first frame of the ultrasound videoclip, the user is asked to select a rectangular portion including a longitudinal view of the IVC (figure 6.1). A lowpass filter is used to blur the selected portion of the frame. The user then chooses two reference points on the image, and draws the M-line, or a segment that cuts the IVC transversally and specifies the location and angle of the diameter measurement. A "reference segment" connects the two reference points. The position of each reference point is automatically re-mapped in subsequent frames comparing single image portions centered on the current position of the reference point in the first frame of the pair. The two portions are aligned in the 2-D Fourier domain. The new reference segment is calculated based on the new positions of the reference points. The M-line is recalculated by maintaining its geometric relationship to the reference segment, that is, by keeping constant their angle of intersection as well as the ratio of the distances between their intersection point and the two reference sites. In this way, the M-line should follow movements and deformations of the IVC and ideally intersect the IVC always along the same cross section. The US intensity along the line is estimated by interpolation after the M-line has been repositioned, obtaining a 1-D function. To emphasize the rapid variations, this function is then processed by an arctangent function. Then, the borders of the vessel are detected as the points in which such rapid variations are identified as points of local maximal absolute derivative. In this way, the diameter values of a section over time are obtained and the CI index can be estimated. Two components can be identified in the diameter trend, the respiratory component involving larger but slower changes and the cardiac component involving smaller but more frequent changes.

Compared to M-Mode, the new approach limits errors in CI assessment, improves the reliability of diameter monitoring and reduces motion artefacts with a low computational cost. Standardization of the measurement technique is still lacking.

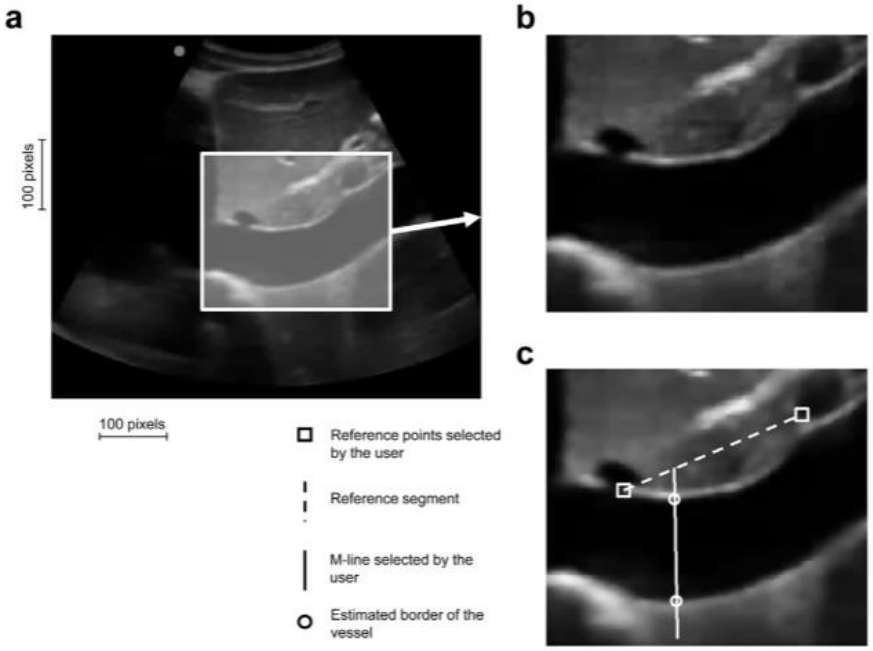

Figure 6.1: The figures show user settings on the first frame of the video, illustrating a longitudinal view of the IVC. The user selects a rectangular portion of the first frame that includes the IVC (a), the chosen portion is enlarged and blurred with a low-pass filter (b). The operator selects two reference points (open squares) and draw an M-line (solid line) (c). Based on these settings, the software defines the reference segment (dashed line) used to plot the displacement of the IVC in subsequent frames and identifies the edges of the vessel along the M-line (open circles) used to estimate the diameter of the IVC. [24]

As already said, the pulsatility along a single section may not be representative of the dynamics of the whole IVC. For example, some parts of the vein can exhibit lower pulsations than others because they are anchored to nearby structures. For this reason, VIPER proposed a second automated method [26] that tracks the movements of the IVC and simultaneously monitors the diameter of different sections of a whole portion of the vessel, again using B-mode ultrasound. Also in this update, the user must select a rectangular portion of the ultrasound video to work on and enter two reference points. Compared to the previous case, it is also necessary to draw two segments cutting across the IVC, one positioned further to the right and one further to the left. Finally, the user must indicate two points close to the edge of the vessel along the leftmost section (figure 6.2). The software then draws 21 lines uniformly distributed between the leftmost and rightmost borders set by the user. The slopes of the lines vary linearly between those of the two lines originally defined by the user. The vein borders are then identified along each of these lines using the same method as in the first study. The boundary position for each line is recomputed as the average of its initial value and the linear interpolation with its two closest neighbors. The estimate of the displacement from one frame to the next is obtained using the same method as in the previous study. Again, the two portions are aligned in the 2-D Fourier domain but, in contrast to the first study, the portion of the image to be aligned is decomposed into five sub-regions. In addition, three images (the present frame and the two previous frames) are considered from the third frame on. Then, the vessel midline is calculated, and it is approximated by a fourth-order polynomial function. Then 10 points are uniformly distributed along the midline of the vein. The sections orthogonal to the IVC midline passing from each such points are considered and the IVC diameters in these sections are computed. In each IVC

section, pulsatility is quantified by the CI. CI values are calculated for each respiration cycle and their values are averaged to determine a single index of pulsatility for each section. From these estimates, several indices, including the mean pulsatility index, the maximum CI, and the standard deviation of the CI, might be computed to describe overall pulsatility. This method solves the problem of artefacts and studies the overall longitudinal variability of pulsatility. Furthermore, by filtering the CI signal it is possible to derive the respiratory and cardiac components.

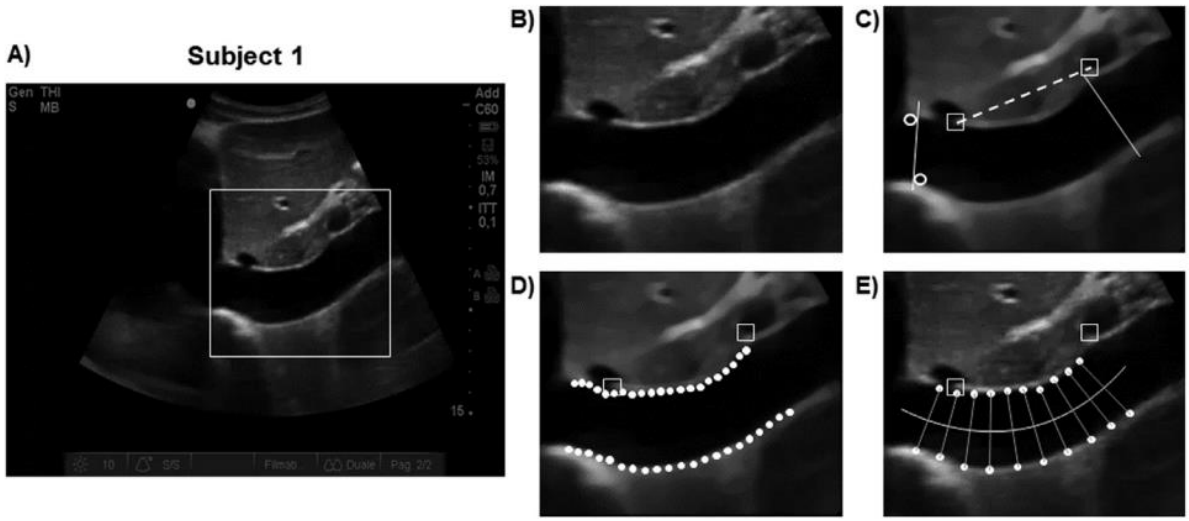

Figure 6.2: The figures show examples of user setting and automated processing in the first frame of an ultrasound video of a longitudinal view of the IVC. A rectangular portion of the ultrasound video is selected and enlarged (A-B). The user selects two reference points (squares), draw two segments that cut the IVC (continuous lines), and indicate two points near the edge along the leftmost section (circles) (C). Based on these settings, the program defines the reference segment (dashed line). Automatically, twenty-one lines are uniformly distributed between the extreme sections indicated by the user, and the software identifies the vein edges (small circles) along the segmentation lines (D). Then, the position of the edges is recalculated as the average between the original value and the linear interpolation with the two nearest points (E). [26]

6.2 Semi-automated method in the transversal plane

The IVC can have a complex geometry in the transverse plane. It often has a non-circular cross-sectional shape with different pulsatility in different directions, with a high variability between different subjects and different clinical conditions. The vessel also exhibits respiratory-related movements in this plane, which are in the order of 4 mm. Albeit small, this displacement may produce relevant alterations in the diameter using a fixed scan line as with M-mode. In addition to respiration, the surrounding structures to which the IVC is anchored can also influence vessel movements. For this reason, studying IVC in a single plane may be inaccurate. To obtain more information on the pulsatility of the IVC, a semi-automatic algorithm [27] was developed by VIPER. This new algorithm analyses the cross-section of the vessel with B-mode ultrasound (figure 6.3). Again, the operator is asked to identify the IVC in the first frame by selecting the working ROI and the center of the vein. Each frame is converted to a grayscale, cropped and then the contrast is enhanced using histogram equalization. Next, the image is processed with

a median filter to achieve stable results even when considering low-quality US video clips recorded from patients in emergency conditions. First, the centroid of the vein is computed and is used to plot venous movements in subsequent frames. Twenty equidistant rays originate from the center and are used to trace the contour of the vein. The intensity of the pixels along each ray is estimated and the border of the vein is set where an abrupt increase in intensity is detected, separating a dark and a light region (it is assumed that the inside of the vein is dark, and the outside is light). Ten sampling points before and after the location of the border in the previous frame are considered. Then the intensity along the ray is approximated by a step function and the root mean squared errors in approximating the intensity are computed. The border of the IVC is estimated as the point of discontinuity of the step function guaranteeing the best fit of the intensity profile. To achieve a smooth boundary of the vein a low pass filter is applied to the x and y coordinates of the border points. Once the vein boundary was determined the area of the IVC lumen is numerically computed (summing the contributions of the 20 circular sectors delimited by pairs of the rays). Thus, a time series is obtained with a sampling frequency equal to the video frame rate. The signal is then low-pass filtered with a cut-off frequency of 4 Hz. The effects of the heartbeat and of respiration on the IVC cross-section are then separated using a filter with cut-off frequency of 0.4 Hz. The cardiac and respiratory components are above and below such a cut-off, respectively. An equivalent diameter is calculated from the area series and then the CI index. The CI is calculated considering both the entire signal and the components alone, the following indices are obtained: CI, RCI, CCI. [27] The results of this study show that the CI value along the transverse axis depends on the direction considered, the pulsatility is greater in directions where the vein has a smaller diameter. Round IVCs are usually associated with lower values of CI. The pulsatility indexes had a coefficient of variation equal to 13% for CI, 21% for RCI and 20% for CCI.

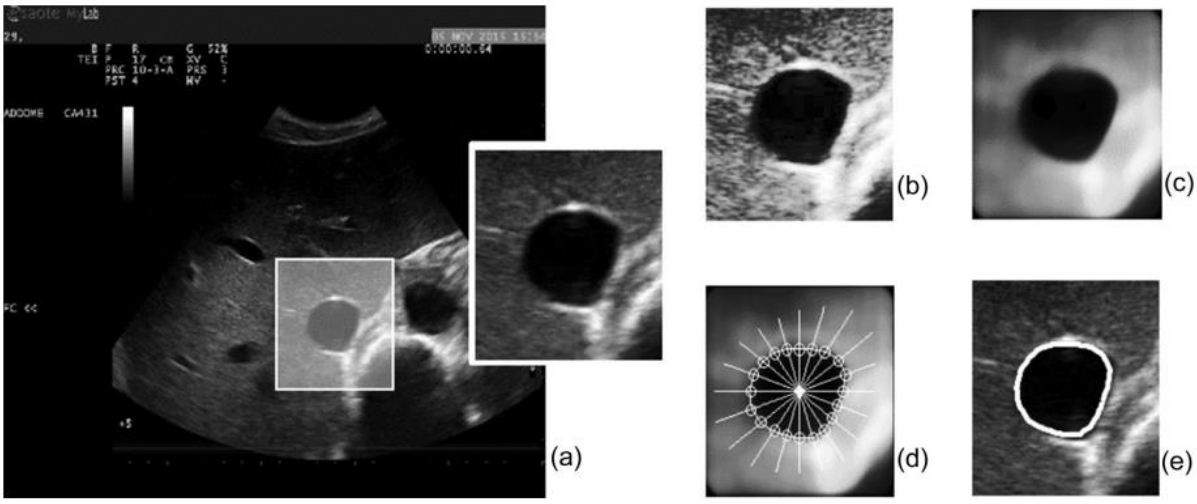

Figure 6.3: The figures show user settings on the first frame of the video, illustrating a transversal view of the IVC. The user selects the position of the IVC on the first frame of the video (a). the portion of image is equalized to enhance the contrast (b) and filtered with a median filter (c). Next, the border of the vein is identified along 20 directions, beginning from the IVC centers (d). The pixel intensity along each ray is estimated, and the vein boundary is recognized where an abrupt increase in intensity is present (e). [27]

6.3 Assessment of right atrial pressure

Right atrial pressure is a key parameter for many diseases and a correct estimation of this index has important clinical implications. For example, an elevated right atrial pressure (RAP) predicts a poor outcome in patients with heart failure (HF). The gold standard for estimating RAP is right heart catheterization (RHC), an accurate but invasive and risky method that can only be used in a few cases. For this reason, the estimation of RAP is often done with the inferior vena cava. In fact, RAP and IVC are linked. The IVC has a larger size in patients with a higher RAP while a lower RAP generates more variation in vessel size. However, the correlation with invasively measured RAP along with the reproducibility of US-based IVC measurements is modest at best. Specifically, the current technique provides fair accuracy when estimating low or high pressures, but it remains inaccurate to estimate intermediate values that encompass most patients across a range of clinical conditions. [28] Non-invasive estimation of RAP depends on operator, is not standardized, and shows motion artefacts.

To solve these problems, in some studies, the RAP was estimated using the algorithms outlined in the previous paragraphs. In an early study in 2019 [4] an estimation model was developed. It estimates RAP using the mean diameter of the IVC, the patient's age and the CI measured along a section of the longitudinal plane with the new semi-automated method. This model estimates RAP with an error of about 3.6 mmHg, the error is smaller than in the classical procedure that does not provide stable information on RAP. In a following work [5] two BTMs were developed either 3 or 5 RAP classes. These BTMs were compared with two standard estimation echocardiographic methods and direct RAP measurements obtained during a RHC were used as reference. In particular, the average diameter and the three pulsatility indices, CI, RCI and CCI, were estimated by the semi-automatic technique. These indexes and some patient characteristics (eight, weight, age, body surface area (BSA) and gender) were used to develop the multi-class estimation BTM. Different models were developed considering all possible combinations of input and the best one was selected. The results show that such models are a promising tool for more accurate pressure estimation than classical methods. Both the semi-automated measurement of CI and the mean diameter are more related to RAP than their manual versions. The BTM with three classes has the lowest miss-classification error in classifying RAP and the BTM with five classes has the highest accuracy compared to literature data. In another study [29] the estimation of right atrial pressure was obtained by studying both the transversal and longitudinal direction of the IVC. A support vector machine (SVM) and linear model (LM) were used, and the results were compared with direct RAP measurements obtained during a right atrial catheterization. Again, LM and SVM showed higher accuracy than guidelines.

Although these studies have limitations (too short US scans, ICCs dependent on the breathing phase in which they were measured, lack of real-time feedback), they show a great step forward in non-invasive estimation of RAP, which can also be used in emergency medicine.

Chapter 7

Materials and Methods

The purpose of this work was to validate new updates to the software presented previously. Therefore, this chapter will introduce the tools and methods used for this goal. It will be explained how new ultrasound videos of the IVC were obtained, the instruments used, and the possibility of using a model to simulate real-vascular conditions to test the software under controlled circumstances.

7.1 MicrUs EXT-1H

The MicrUs Ext-1H is an open architecture ultrasound diagnostic system developed by the company Telemed. It can be used on PCs, tablets, and smartphones. The types of probes supported are convex, micro convex, linear, and endo-cavitary probes that can be used in different display modes, including B and M mode. The scanning depth can vary from 2 to 31 cm depending on the probe type and scanner model. The system works with wide bandwidth multifrequency probes, (2.0 to 15.0 MHz), and generates high-quality video and images in general, abdominal, obstetric, and gynecological ultrasound, etc. The items supplied with the MicrUs EXT-1H are the beamformer (base unit), USB cable and a pen drive. Inside the pen drive there are User's Guide (installation, set-up, and maintenance), User Manual, Measurement and Calculation Manual, Software and Drivers. Transducers are not included and will have to be purchased separately. [30] To use the system, it is necessary to download the software and drivers to the PC and then connect the beamformer with the USB cable. The probe must then be connected to the beamformer (figure 7.1).

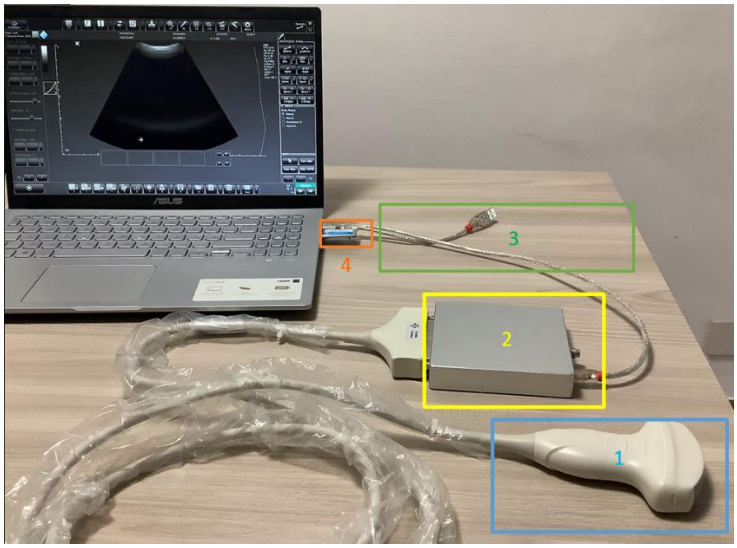

Figure 7.1: The picture represents all elements supplied with the MicrUs EXT and correctly connected. (1) Ultrasound probe, (2) beamformer, (3) USB cable and (4) pen drive.

7.1.1 ECHO WAVE II scanning software

The system is managed by the ECHO WAVE II scanning software, which features an intuitive user interface with customizable user settings, and programmable presets that allow measurements and calculations even on stored images and videos. It has a reporting program and allows the saving of photographs and movies in different formats. The life cycle of the instrumentation is extended by constant updates and implementations of new ultrasound imaging modalities, available as freeware. The software also allows telemedicine functions with remote control for training, service, and technical support. Figure 7.2 shows the user interface with different settings and parameters that can be changed.

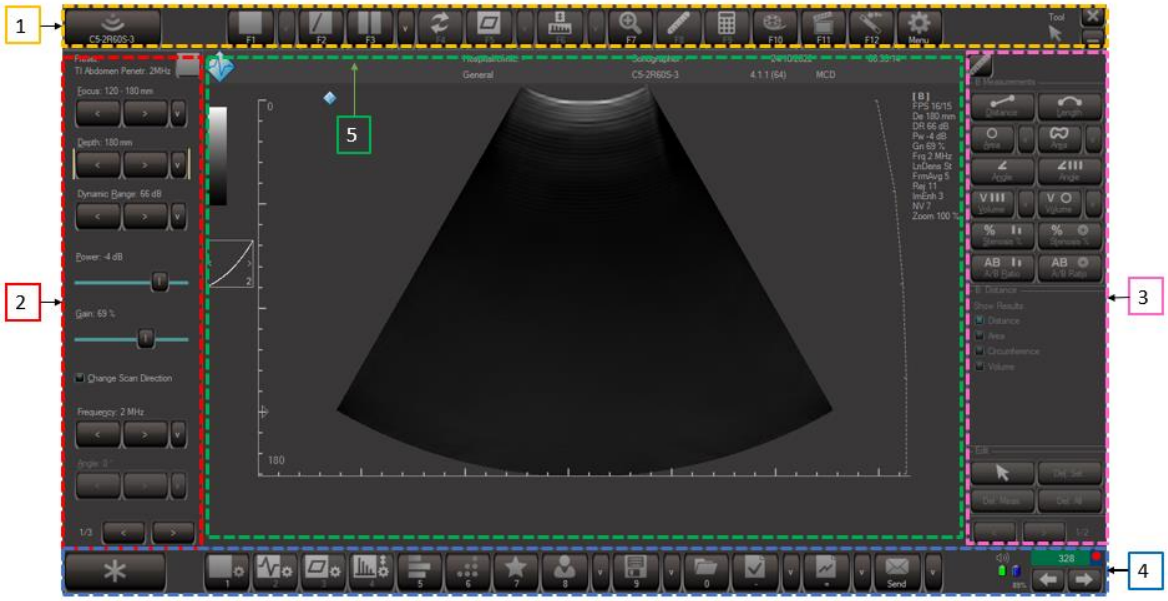

Figure 7.2: The figure shows the use interface of ECHO WAVE II. (1) Top toolbar, allows to change the scan mode, open the Control panels for calculations and measurements, activate and/or open Zoom, Cine loop, the Automatic optimization, open the General menu, (2) Left side controlbar, contain controls for adjusting image quality and ultrasound scanning parameters, (3) Right-side controlbar, contain controls that do not change scanning parameters, (4) Bottom toolbar, contains buttons to open/activate control panels for different scan modes and a quick selection of functions, (5) Ultrasound image area, contains pure ultrasound image in the centre of it and ultrasound surrounding data that is printed or saved depending on the user request.

To improve the quality of the ultrasound image, it is essential to properly adjust the controls in the ECHO WAVE II software. Initially, depending on the structure to be detected, it is necessary to set the “Depth of the scan”. A greater depth is used in the case of larger or deeper systems and vice versa. Once the depth is adjusted, the "Gain," "Time Gain Compensation" (TGC or time gain compensation controller), and "Focus" controls can be changed. Gain and TGC are the most important parameters, and the ability to master them during the examination allows the best possible image to be obtained. Both are necessary for the electrical amplification of return echoes. TGC is used to produce a uniformly bright image along its entire depth. The operator must use the TGC to reduce the brightness of the surface field by increasing the brightness of the deep field. This is achieved by raising the gain as the time the return echo

takes to reach the probe increases. After that, the overall Gain is set to raise (or reduce) the brightness of the entire image by uniformly amplifying all return echoes, regardless of the depth of their origin. To improve image resolution and reduce artifacts, it is necessary to adjust the intensity of the sound pulse emitted by the probe through "Acoustic power." This is the only user-modifiable parameter that affects the sound transmitted to the patient. Gain controllers and TGC should be employed wherever possible to optimize return echoes' amplification to adjust the acoustic power setting as low as possible. Additionally, depending on the depth at which the structure to be investigated is located, it will be important to select the right Frequency. High frequencies improve input signal resolution but decrease ultrasonic penetration at depth. As a result, for scanning superficial tissues, high frequencies should be used, and vice versa. In addition to the basic parameters mentioned above, there are other controls to improve the image. It is advised to properly adjust the image using the Gain, TGC, and Acoustic Power settings before modifying these parameters. [26]

Focusing is used to increase the resolution of specific areas. As described earlier, the US beam is focused on selected areas (or focusing zones). It is possible to select several focusing areas ("Focus number") and the focusing depth ("Focus"). It is important to adjust focuses so that focusing markers are at the center of the anatomical structure which is of most interest.

One of the methods to attenuate noise is to use "Speckle reduction". Speckle reduction imaging methods are image processing techniques that evaluate the image pixel by pixel, try to identify tissues, and eliminate "Speckle" (speckle noise), so that the image is smoother and cleaner. A similar effect can be achieved through the "Frame Averaging" command, which can smooth out noise by averaging the sequence of several different screenshots. These methods can reduce the frame rate, slow down the operation of the software, and distort some details in the image. For example, high values of Frame Averaging make the image smoother, but may hide small details in the image.

Another parameter that can be tuned is the "Dynamic range" (Variable Dynamic Band), which adjusts the logarithmic amplification of the echo signal. A high Dynamic range allows to discriminate and identify structures with minimal differences of acoustic impedance. On the other hand, low Dynamic range allows for a more contrasty image, useful for visualizing structures with high acoustic impedance differences (e.g., cysts, vessels, bladder, etc.). A similar result can be obtained by adjusting the Palette (Color map or Gray scale) of the ultrasound image. Unlike the Dynamic range, which increases or decreases the number of shades of gray displayed, the Gray scale determines how dark or light each level of gray are shown according to the intensity of the ultrasound signal. The Color map can be changed through the "Gamma," "Brightness," and "Contrast" controls.

The "Lines density" command allows to adjust the number of scan lines in the ultrasound image. A higher level provides better image resolution (more scan lines) but reduces the frame rate, and vice versa. The "Image enhancement" parameter can be used to achieve a relief effect by enhancing the tissue contour and more echogenic structures. In case a higher frame rate is

required, it will be necessary to disable the function since it tends to decrease the frame rate. Another control to reduce the amount of noise, in addition to Speckle reduction and Frame averaging, is "Rejection". Ultrasonic signal rejection is a type of processing that changes a range of values of the ultrasonic signal received. The values of this function ranging from 0 to 32. 0 means that the function is not active while a higher value reduces more data.

Depending on the type of transducer used, there is a choice of presets, which is a combination of predefined parameters based on the ultrasound investigation needed. [31]

7.2 Ultrasound probe

For this study, a Convex-type probe, C5-2R60S-3, manufactured by the company Telemed, was used (figure 7.3). The crystals on the probe are S3 type and the transducer can work in the frequency range of 2-5 MHz. It has a bending radius of 65 mm and a field of view of 60°. The main applications are for abdomen, gynecology, and pediatric ultrasound. [32]

Figure 7.3: Convex probe C5-2R60S-3. [32]

7.3 Ultrasound vein model

The ultrasound scanner described was first used with a model simulating the structure of veins: SONOtrain ultrasound vein model. [33] This manikin is made of a material that has a texture and echogenicity similar to that of human tissue. It is designed to be a teaching tool for learning how to perform ultrasound acquisitions and can also be used by inexperienced doctors to learn how to perform injections without perforating vessels. The model consists of three veins of different diameters (8 mm, 12 mm and 15 mm) that are located at a depth of about 30-40 mm. In addition, liquids can flow through these vessels, which makes the model even more realistic. A fluid container simulating the operation of an intravenous feeding, is also provided, and a regulator is used to control the amount of outflow. Figure 7.4 shows the manikin during an ultrasound acquisition in the longitudinal plane of the largest vessel.

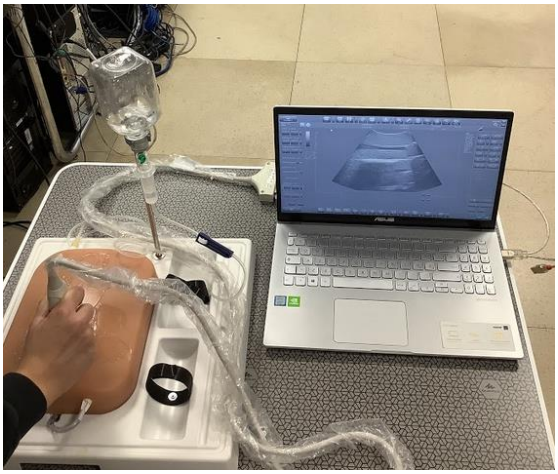

Figure 7.4: Image of manikin during an ultrasound acquisition in the longitudinal plane of the largest vessel (15 mm diameter).

The aim in this study was to investigate a possible application of the model in the evaluation of new algorithms for studying IVC. In particular, the idea was to examine the software's ability to measure the diameter and trace the vessel walls. Various ultrasound images were therefore acquired in both cross-sectional and longitudinal sections; examples are shown in figure 7.5.

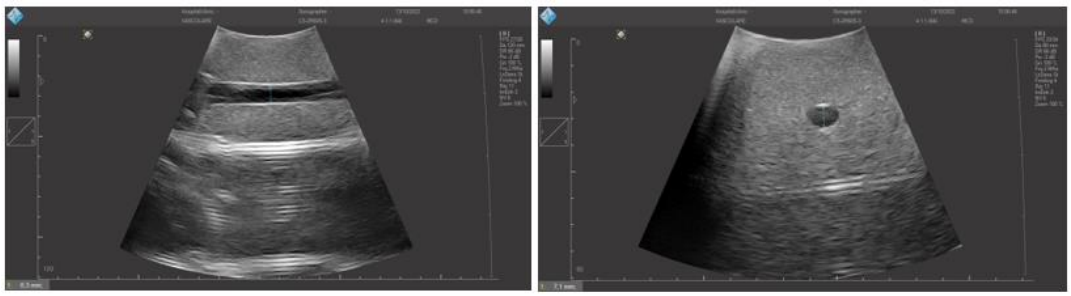

Figure 7.5: Example of two ultrasound images, along the longitudinal and along the transverse axis respectively, of the central vessel of the manikin (15 mm diameter).

Various tests have shown that changing the fluid flow does not result in significant changes in diameter. The diameter is much more sensitive to the presence of the probe than to changes in flow. In fact, when using a convex probe, a certain amount of pressure must be applied to make the transducer area completely adhere to the manikin. This pressure partially compresses the vessel. Ultrasound videos of the manikin were processed with the software, but no results were obtained. In contrast to the IVC, the diameter does not vary with flow, nor is there any kind of movement of the vessel, other than compression due to the probe. As the dimensions vary in a poorly controlled manner, the manikin was only useful during the learning phase of the ultrasound basics and not for software evaluation.

7.4 IVC ultrasound

To evaluate the new vein analysis algorithms, numerous ultrasound videos were collected using the ultrasound machine described above. Ultrasound of the IVC is generally performed with a convex probe and can be carried out in both transverse and longitudinal views. In both cases, the use of a probe-tissue coupling gel is essential. The gel increases the conductivity of the US by cancelling out the resistance to its propagation due to the presence of air. The orientation of the probe can be identified by a marker on it; the scanned structures that are in the direction of the marker are shown in the top left of the ultrasound video (figure 7.6).

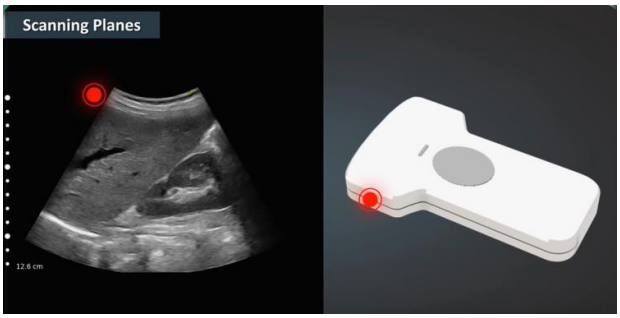

Figure 7.6: Correspondence between ultrasound probe marker (in red) and US image representation.

To obtain a transverse scan the probe is positioned just below the xiphoid process along the transverse axis. By convention, in this study, the marker has been positioned at the patient's right shoulder, so all structures present on the right side of the patient will be shown on the left side of the ultrasound image and all the structures present on the left side are shown on the right side of the image. The most superficial structures are shown at the top and the deepest at the bottom. Two vessels can be identified from the transverse plane images and video: the IVC on the left and the aorta on the right. Artifacts generated by the deeper presence of the spinal column are visible at the bottom (figure 7.7).

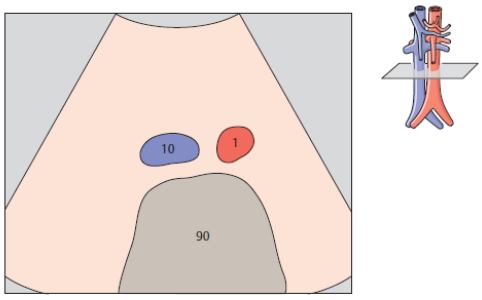

Figure 7.7: The image represents the transverse view at the level of the upper abdomen. The vena cava (10), the aorta (1) and the spinal column (90) are visible. [18]

In the longitudinal scan, the probe must be positioned at the level of the xiphoid process, in this case in the cranio-caudal direction. By convention, the marker is positioned in the cranial direction, so tissues that are in the cranial direction are shown on the left side of the ultrasound

image, and those in the caudal direction on the right side. On longitudinal ultrasound, in addition to the IVC, the liver, right atrium, hepatic vein and other abdominal structures can be visualized (figure 7.8). [18]

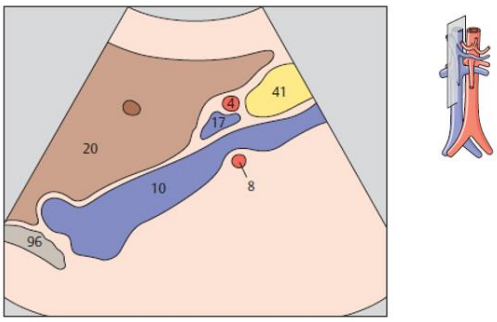

Figure 7.8: The image represents the longitudinal ultrasound scan at the level of the upper abdomen. The vena cava (10), hepatic artery (4), right renal artery (8), portal vein (17), right lobe of liver (20), head of pancreas (41) and diaphragm (96) are visible. [18]

7.5 Segmentation software

The performance achieved by software in the segmentation of the inferior vena cava along the transverse and longitudinal plane, were evaluated through a comparison with binary masks obtained from manual segmentation and taken as a reference. The software, that do not differ much from the algorithm presented in the previous paragraphs, and the way in which the reference masks were obtained will be described below.

7.5.1 Software VIPER

The software is implemented in Matlab and is an updated version of the algorithm presented in [26] and [27]. In particular, the transverse plane processing algorithm was significantly modified. It allows the median filter size, the dimension of the ROI and contrast modification mode to be varied according to the characteristics of the ultrasound video. One of the new developments introduced by the software is that in the case where no significant center shift or area change occurs between two consecutive frames, the results obtained for the previous frame are retained. A minimum value that the area must assume was also defined; again, if this limit is exceeded, the software maintains the results obtained in the previous frame. This last control allows the software to continue processing even in cases where the vein tends to close or disappear. Again, as in [14], the software identifies boundary points by evaluating the intensity variation along the segmentation lines. In this case, however, a selection of the detected edge points is made, those considered “wrong” are discarded. In fact, although vein sizes vary from subject to subject and at different stages of the respiratory/cardiac cycle, points too close or too far from the center are anatomically improbable and, therefore, not considered. Another modification, which also affects the longitudinal plane, involves the rectangular working portion. The latter is no longer drawn by the user in the first frame but is estimated based on the input data points and the chosen dimensions. In the longitudinal plane, the segment that cuts

the IVC on the left side must no longer be traced. Furthermore, to track the two reference points, the software no longer works in the 2-D Fourier domain but exploits the recognition of Oriented Fast and Rotated BRIEF (ORB) features in each frame. ORBs are descriptors for image detection and matching, which are widely used in computer vision problems. [34] For both working planes once the processing of the ultrasound video is completed, the software returns the coordinates of the edge pixels and the processed video with the superimposed segmentation. Specifically, for the transverse plane it also returns the coordinates of the vein center and the value of the segmented area while for the longitudinal plane it returns the coordinates of the reference points.

7.5.2 Manual segmentation software

The manual segmentations were obtained using a Matlab script that takes in input the video and the corresponding frames to be segmented. With this code, each frame can be processed by positioning points at the edges of the vein using the mouse. To optimize the manual operation, the segmentations are not performed on all frames of the video but at regular intervals short enough to evaluate all significant variations in the section and position of the vein. Knowing the frame rate and duration of the video, the appropriate selection interval was chosen for each case to process at least 1 fps. It was considered that the most rapid variations are related to the cardiac cycle, characterized by a frequency of approximately 1 Hz. Even displacements of the probe, such as translations or changes in inclination, generate a variation in the position and section of the vein. Although faster variations are also present, the analysis of 1 fps was considered sufficient to validate the software's ability to correctly track and segment the vessel.

Along the longitudinal axis, the VIPER segmentation software follows the movement of the vein by processing only a portion of the vessel. For the manual, the entire vein section visible in the ultrasound video was segmented, then for each frame only the portion segmented by the software to validate was considered. In this way, however, it will not be possible to assess the ability of the algorithm to always segment the same portion of the vessel for the duration of the ultrasound video.

7.6 Performance evaluation

This section describes the statistical parameters estimated to evaluate the performance of the software and the various tests it was subjected to.

7.6.1 Statistical parameters

To compare the manual segmentations with those obtained from the software, statistical metrics were calculated. In literature, the most used parameters for validating segmentation techniques are the Dice Similarity Coefficient (DSC) [35], the Intersection-over-Union (IoU), or also called the Jaccard index [36], the Relative Volume Difference (RVD) and the Hausdorff Distance (HD) [36]. All presented metrics, except HD, can then be calculated from the binary

masks obtained from the segmentation results. So, for each frame compared, a value of the parameters will be obtained.

The IoU and DSC measure the similarity between two data sets. The former is defined as:

$$IoU = \frac{|X \cap Y|}{|X \cup Y|} \tag{7.1}$$

Whereas the DSC is defined as:

$$DSC = \frac{2|X \cap Y|}{|X| + |Y|} \tag{7.2}$$

In our case, X represents the manual mask and Y the automatic mask obtained as output from the software. This variable can have values in the range of 0 and 1. If there is a complete overlap between the two masks it accepts a value of 1, while 0 in the opposite case. The difference between the two metrics is that the IoU penalizes under- and over-segmentation more than the DSC. Even so, both scores are appropriate metrics, the DSC is the most used metric in most scientific publications [36] which is why it was chosen for this study.

The RVD is a statistical tool that measures the difference between two data sets and is defined as follows:

$$RVD = \frac{|Y| - |X|}{|X|} \tag{7.3}$$

Where X represents the manual mask of the vessel and Y the automatic mask. This parameter has only a lower bound equal to -1. A negative value indicates under-segmentation, while a positive value indicates over-segmentation. The larger the value, the greater the over-segmentation. Zero represents the optimal situation.

In contrast to other binary mask-based metrics, the HD is a spatial distance-based metric. The HD measures the maximum of all minimum distances between two curves in the plane. In our case, the curves to be compared are the vein contour defined by the automatic mask and the vein contour defined by the manual mask. The value is expressed in millimeters.

Therefore, to assess processing performance, DSC, RVD and HD were estimated for both transverse and longitudinal computing. Considering the clinical importance of the vein area, its value in the transverse plane was estimated for each frame as the area of the polygon defined by the border points. The error committed by the software compared to manual segmentation was calculated and then averaged over the entire video.

Along the longitudinal plane, the software's error in estimating the mean diameter was evaluated. For the manual and software segmentation the diameters were estimated from the median of the vessel. The median was calculated frame by frame as the average of the two edges identified by the segmentations and then it was interpolated with a straight line. Between 5% and 95% of the length of this line, 30 points were uniformly distributed and the lines orthogonal to the median passing through them were considered. The diameter was then calculated from the intersection of the newly estimated lines with the vessel edges as the Euclidean distance between two points. The thirty diameters obtained were then averaged to calculate a single representative value for each frame. The error committed was calculated for each frame as the difference between the average diameter estimated by manual segmentation and the average diameter estimated by the software. The mean and standard deviation of the error is reported for each video of each test. For both diameter and area, positive error values indicate under-segmentation by the software, while negative values indicate over-segmentation. In the literature the Bland-Altman plot is used to assess how well two metrics agree with each other. [37] The Bland-Altman method makes it possible to assess the size of the agreement/disagreement between two measurement methods and to look for systematic differences, outliers (outliers), and structures of disagreement (patterns). The ideal situation is when the first and second measurements coincide, in this case, the average systematic error (bias) is zero and the points are aligned along the x-axis. [38] Specifically, in this study, the Bland-Altman plot was used to, more accurately, evaluate the agreement between the measurements of diameters and areas estimated manually and with software. In fact, the mean value and standard deviation of the error do not allow to evaluate the results for each frame nor to understand for how many frames the software over/under segments the IVC. To better analyze the results obtained in the cases of greatest interest, i.e., which most represent the capabilities and limitations of the software, the Bland-Altman plot is reported.

7.6.2 Tests conducted

The first tests to which the algorithm was subjected involved the processing of videos acquired by us with the portable ultrasound scanner. Their aim was to assess the reliability and resilience to occasional events of the software. In a subsequent test, their ability to segment ultrasound videos acquired directly by doctors was then evaluated. To correctly interpret the results obtained from all these tests, the variability of manual segmentations must also be considered. The latter was estimated by means of two further tests. Finally, a test was performed to assess how much the results obtained by the algorithms depend on the user input. All tests were performed in both transverse and longitudinal planes. The videos used in the first tests were acquired using the following protocol. First, the ultrasound probe was connected to the computer and the patient was made to lie supine. From here the actual ultrasound examination began. Using the ECHO WAVE II software, the ultrasound parameters were set to optimize the image according to the case being analyzed and finally the video was recorded. The result was then processed with the VIPER segmentation software. The acquisitions were performed on two 24-year-old women in good health. It should be noted that, in general, it was easier to obtain better quality video with the second patient.

7.6.2.1 Reliability testing

To assess reliability, the software was subjected to four different tests for which the following videos were acquired:

- Test 1: thirty videos lasting 30 s each in which the condition of the vessel remains virtually unchanged.
- Test 2: four videos of 2 minutes each, also recorded under static vessel conditions, useful for validating the performance of the software in longer examinations.
- Test 3: ten videos of 1 minute each, in which the operator moves the probe left and right to assess the algorithms' ability to follow the vein as it moves.
- Test 4: ten videos each lasting 1 minute, in which the probe is moved so that the vessel was no longer seen for 10 s and then displayed again. In particular, the vein was not present in the ultrasound video from the 30^{th} to the 40^{th} second. This was to validate the software's ability to find the vein.

7.6.2.2 Resilience testing to occasional events

Afterwards, additional ultrasound videos were acquired to test the resilience of the software to occasional events. The following conditions were evaluated along both planes:

- Test 5: sudden change in diameter due to a very rapid pressure change generated by a coughing fit. In this case, ten videos lasting 20 s each were acquired, the coughing fit occurring at the fifteenth second.
- Test 6: change in probe tilt angle during recording. Ten videos with a duration of 10 s each were acquired, the tilt being changed after 5 s.
- Test 7: simulation of a shadow cone by interposing a low echogenic material between probe and patient. Ten videos of 15 s each were acquired for this test.

7.6.2.3 Reliability testing on hyper- and hypo-volemic patients

For the transversal plane, 53 ultrasound videos acquired on hyper-, hypo- and eu-volemic men and women were processed. In the literature [20], an IVC diameter of less than 10 mm at the end of the expiratory phase is indicative of hypovolemia, whereas values greater than 25 mm are more likely in hyper-volemic cases. Based on this information, the area values obtained by manual segmentation allowed us to divide the subjects into two large groups, hypo- and hyper-eu-volemic. Manual segmentation, however, was not performed for every frame and therefore it was possible that some expiratory phases were missed. Furthermore, in some videos the vein was not clearly visible and manual segmentation was also unreliable. For these reasons, the division was also performed by visual analysis of the ultrasound videos. The decision to divide the subjects into two groups was made because, in hypovolemic cases, given the small size of the vessel which tends to close completely in some cases, correct segmentation is more complex. Lower software performance was expected.

Nine ultrasound videos acquired from five patients with a bi-plane probe were chosen for the longitudinal plane, of which only the portion corresponding to the longitudinal view was processed. In this case, patients were not divided into hyper- eu- and hypo-volemic.

7.6.2.4 Testing for intra- and inter-operator variability of manual segmentations

Inter- and intra-operator variability was estimated by running tests on both works plans to account for the imprecision associated with manual segmentation and afterward evaluate the VIPER software's mistakes objectively. Along the transverse plane, to evaluate intra-operator variability, the 40th frame of the sixth video of Parient2 acquired for Test 1 was segmented 30 times by the same user. Similar testing was performed for the inter-operator case, where the same frame of the same video was segmented from 10 different people. The identical tests were conducted along the longitudinal plane by segmenting the 10th frame of the first video of the Patient2 obtained for Test 1. In both cases, to evaluate the results obtained, DSC and HD were used as the statistical parameters, i.e., the most widely used metrics in the literature for this type of analysis [39], [40]. In addition, to evaluate the variation of the area estimate in the transverse plane, the average and standard deviation of the difference between the values obtained from the various segmentations were determined. The same procedure was carried out along the longitudinal plane by estimating the error of the mean diameter.

7.6.2.5 Sensitivity testing to user input

Evaluating how responsive the algorithm is to user input is necessary to provide an objective view of the performance achieved by the software in analysis. With this aim, the results obtained from processing the same ultrasound video were compared in both the transverse and longitudinal planes. Specifically, in the transverse plane, video 35, belonging to the hyper-euvolemic patients, was processed by varying the initial position of the vessel center from time to time. On the other hand, for the longitudinal plane, the 10th video belonging to the second patient acquired during Test 1 was chosen. In this case, different portions of the vein were studied by also changing the position of the reference points at each process. The same user processed each video five times. Even for this analysis, DSC, HD, RVD, area error for the transverse plane, and diameter error for the longitudinal plane were estimated. Specifically, to verify that the software obtains similar performance as the input change, the results achieved for both work planes were compared with the manual segmentations. For the transverse plane, an additional test was carried out to validate the algorithm's ability to obtain approximately equal segmentations as the initial position of the center varies; in the longitudinal, such a comparison was not possible because as the input vary, the portion of the vessel processed by the software changes.

7.7 Selection of segmentation software parameters

For processing along transverse plane in VIPER software, the minimum frame-to-frame variation values of vessel center and estimated area were set to 13 pixels and 300 pixels^2,

respectively. On the other hand, the minimum area value was chosen to be 200 pixels^2. The number of segmentation rays along the transverse plane was set to 30, and the same value was chosen for the segmentation lines in the longitudinal. The ROI size was set at 400x400 pixels for both working planes. This value proves an effective trade-off between a reduction in computational weight and the software's capacity to track and segment the vein. The Matlab "imadjust" function, which saturates 1% of the image data at low and high intensities, was typically employed when the contrast modification mode was applied to the image during processing. The median filter size was set equal to 5 for the transverse plane and equal to 0 for the longitudinal.

7.8 Bug reporting

Bugs, that commonly occurred, were found during the initial processing of the videos described in the previous section. These limitations were fixed and overcome as far as possible to improve the overall performance of the algorithm.

The first limitations were found in processing along the transverse plane. It was noticed how the algorithm in many videos associated the vein edges with highly irregular and anatomically impossible shapes. Figure 7.9 shows the example of the second ultrasound video acquired in static conditions and belonging to Patient2.

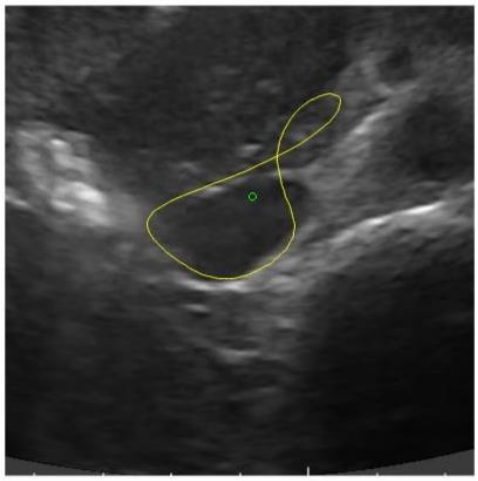

Figure 7.9: The image represents 256th frame of the second video of Patient2 acquired for the first test, where the algorithm associates the vein edge with an irregular and unrealistic shape. The estimated vessel border is represented in yellow and the center of the vein in green.

Because of this problem, in some cases the software could not process the video, crashing due to an error. This occurred, for example, during the segmentation of video 6 belonging to Patient2 during Test 4. Analyzing this video showed that improper edge point interpolation led to the selection of pixels outside the software's working ROI, making processing impossible. An image of this case is shown in figure 7.10, where the edge points recognized by the algorithm are shown in red, only some of them will be considered as "correct", the interpolation of the

points considered "correct" in green, the filtered curve in black and the estimated vein center in yellow. The problem depended on the interpolation method used, which considered points far away from those evaluated as correct. When these "assumed" points were outside the working ROI, the software could not proceed with processing. Additionally, this interpolation resulted in an incorrect estimation of the center, leading correct edge points to be excluded because they were too close and to be taken into consideration others that did not belong to the vessel. This problem was solved by implementing linear interpolation in polar coordinates. As visible in figure 7.11, the segmentation of the same frame of the same video under the same initial conditions turns out to be representative of the real anatomy of the vessel.

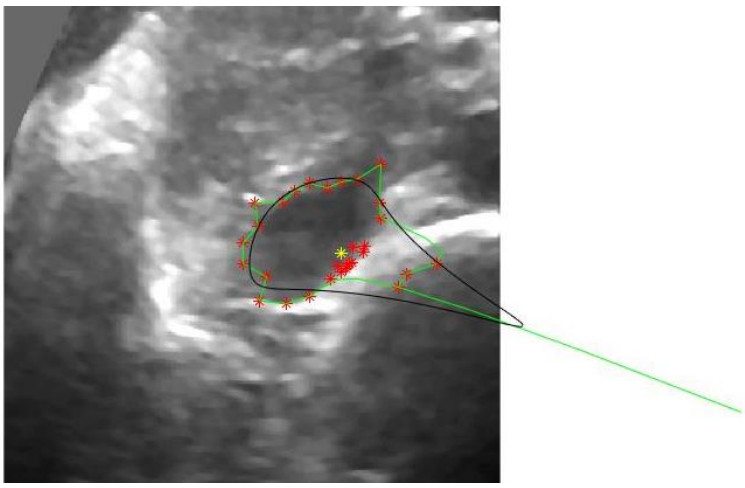

Figure 7.10: The image shows the improper edge interpolation obtained from frame 146 of the sixth video of Patient2 during the probe displacement test. The edge points recognized by the algorithm are shown in red, the interpolation of the points considered "correct" in green, the filtered curve in black and the estimated vein center in yellow.

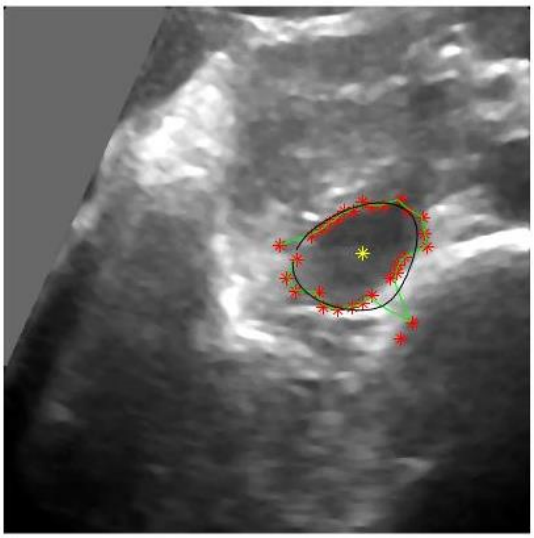

Figure 7.11: The image shows the correct edge interpolation obtained from frame 146 of the sixth video of the Patient2 during Test 3. This result is obtained imposing the same input as in the previous case. The edge points recognized by the algorithm are shown in red, the interpolation of the points considered "correct" in green, the filtered curve in black, and the estimated vein center in yellow.

As a result of the changes, an improvement in the segmentation speed of the software was evaluated. Five ultrasound videos were processed using both the upgraded program and the older version, keeping the center coordinates entered for the first frame unchanged. The results obtained in frames per second are shown below (table 7.1) and it is visible how the upgrade has led to an improvement in this field as well. In general, the new version turns out to be faster and segments on average about 4 ± 1.48 fps more than the previous version.

Video processed	**Previous version (fps)**	**Upgraded version (fps)**
Video 7 of Patient2 in static conditions in the transverse plane	15.69	19.60
Video 14 of Patient2 in static conditions along the transverse plane	15.89	17.84
Video 1 of Patient1 in static conditions along the transverse plane	25.89	29.65
Video 22 of the hyper- and eu-volemic patients along the transverse plane	29.81	35.93
Video 20 of the hyper- and eu-volemic patients along the transverse plane	29.58	33.75

Table 7.1: Results obtained from the evaluation of the segmentation speed of the two versions of the software VIPER.

A persistent problem that avoided the processing of some ultrasound videos was discovered while working in the longitudinal plane. The issue was related to the length of the segmentation lines; in fact, if they were longer than the working ROI, an error was displayed, and processing was interrupted. An example of one of the cases where this bug occurred is shown in figure 7.12 which represents the second video of the third test belonging to Patient2. The image shows how the last line is not displayed because the lower boundary exits the working ROI, and the software could not proceed with the elaboration. The length of the segmentation lines is estimated based on the average diameter and the point of intersection between the line linking the reference points and the segmentation line. Specifically, the upper edge and lower edge segmentation limits are calculated from the distance between the intersection point and the center of the vessel by subtracting and adding, respectively, 90% of the median diameter.

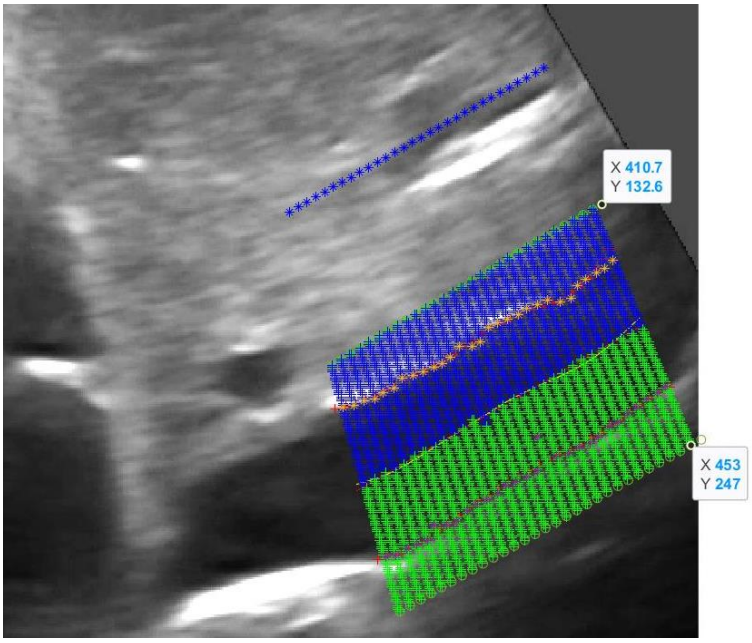

Figure 7.12: The image represents frame 758 of the second video of Patient2 acquired for the probe displacement test. The lower boundary of the last line exits the working ROI, as a result, the software fails to continue with processing.

This limitation was overcome by considering only the line points that lie within the ROI and excluding the others. This can be seen in figure 7.13, obtained from the same frame of the same video with the same initial conditions. However, if the vein moves excessively to one side of the working zone, the software estimates the edge of the image as the bottom edge of the vessel, leading to a significant segmentation mistake. For this reason, it is appropriate not to work with ROIs of too small size in the case of ultrasound videos in which the vessel moves excessively.

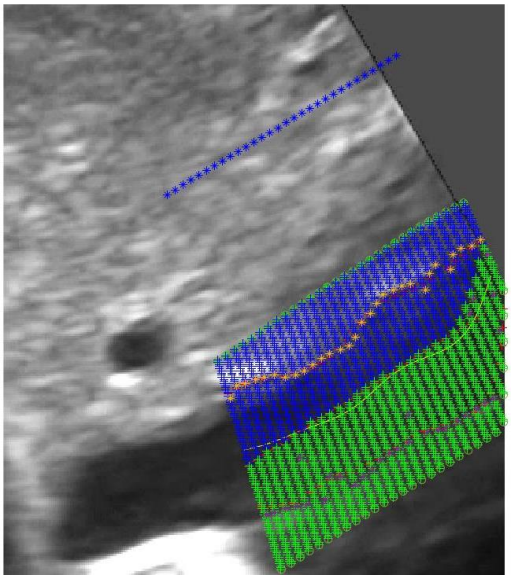

Figure 7.13: The image represents frame 758 of the second video of Patient2 acquired for the probe displacement test. It can be seen how the lines do not leave the working ROI, but the estimated edge coincides with the edge of the image.

Chapter 8

Results

This chapter presents the results obtained from the previously described tests. Regarding the tests performed on our acquisitions for each patient the results are evaluated separately. In general, the mean value and standard deviation of the DSC, RVD, and HD are reported for each ultrasound video. In addition, the area and diameter estimation errors are reported for the transverse and longitudinal planes, respectively. In all those tests in which the vessel disappears for the corresponding frames the classical statistical parameters are not evaluated; instead, the estimated area value is reported for the transverse plane while, for the longitudinal plane, the mean diameter is reported to quantify the software error in not recognizing the disappearance of the vein.

8.1 Results of the inter- and intra-operator variability test of manual segmentations

The results obtained from the manual segmentation variability tests are shown below. In the transverse plane, the values obtained for both cases are very similar (table 8.1), with the DSC having a mean of about 0.9 and a low standard deviation. The HD is about 2 mm, with a standard deviation of 0.6 mm, while the estimated area error is of the order of 10 mm^2. The results in the longitudinal plane do not differ from those just described (table 8.2). The inter- and intra-operator variability shows an average DSC of more than 0.9 and a Hausdorff distance of about 6 mm.

Statistical parameters	Inter-operator variability	Intra-operator variability
DSC	0.8890±0.0329	0.8982±0.0321
HD [mm]	0.29±0.59	2.14±0.57
Area estimation error [mm^2]	7.59±36.44	17.12±24.48

Table 8.1:Results obtained from the inter- and intra-operator variability test in the transverse plane. To evaluate intra-operator variability, the 40th frame of the sixth video of Patient2 acquired for Test 1 was segmented 30 times by the same user, while to study inter-operator variability, the same frame of the same video was segmented to 10 different people.

Statistical parameters	Inter-operator variability	Intra-operator variability
DSC	0.9252±0.0205	0.9289±0.0142
HD [mm]	6.56±2.20	5.71±1.02
Diameter estimation error [mm]	0.33±1.38	0.24±1.48

Table 8.2: Results obtained from the inter- and intra-operator variability test in the longitudinal plane. To evaluate intra-operator variability the 10th frame of the first video of Patient2 acquired for Test 1 was segmented 30 times by the same user, while to study inter-operator variability the same frame of the same video was segmented to 10 different people.

8.2 Results of the sensitivity test to user input

The statistical parameters obtained from comparing the results achieved by the software as the input change with the manual segmentations are shown in the tables below. For the transverse plane the performance in the different tests turns out to be very similar (table 8.3). However, this is not the case in the longitudinal plane for which the DSC goes from a value of 94% achieved in the Test 3, to a value of 68% estimated in the fourth, while the RVD also varies by an order of magnitude between the different processes (table 8.4).

Test	DSC	RVD	HD [mm]	Area estimation error [mm^2]
1	0.8149±0.0758	-0.2655±0.1255	3.95±1.67	61.46±42.73
2	0.8144±0.0760	-0.2661±0.1257	3.93±1.68	62.05±42.42
3	0.7964±0.0902	-0.2861±0.1434	4.32±2.50	64.16±51.29
4	0.8166±0.0820	-0.2592±0.1324	3.75±1.75	56.23±40.76
5	0.8062±0.0736	-0.2771±0.1209	4.09±1.63	62.55±40.34

Table 8.3: Results of software sensitivity to input along the transverse plane. The test was performed with the 35th video from hyper- and eu-volemic patients. The input was selected five times by the same user and the results were compared with manual segmentation.

Test	DSC	RVD	HD [mm]	Diameter estimation error [mm]
1	0.8655±0.0968	-0.1720±0.1746	10.36±1.73	0.18±0.19
2	0.8444±0.0903	-0.2143±0.1542	10.42±1.84	0.22±0.17
3	0.9408±0.0334	-0.0168±0.0735	10.72±1.35	0.01±0.06
4	0.6852±0.1518	-0.4003±0.2295	11.95±2.25	0.36±0.23
5	0.9034±0.0820	0.0362±0.0620	10.26±1.44	-0.03±0.10

Table 8.4: Results of software sensitivity to input along the longitudinal plane. The test was performed with video 10 from Test 1 of Patient2. The input was selected five times by the same user and the results were compared with manual segmentation.

On the other hand, table A.1 shows the performance achieved by comparing the five segmentations obtained in the transverse plane as the input change. The average results from these tests are shown in table 8.5, where it is possible to observe a DSC of more than 96%, an incredibly small RVD, HD, and area estimation difference.

DSC	RVD	HD [mm]	Area estimation difference [mm^2]
0.9636±0.0479	-0.0131±0.0482	5.05±7.52	0.95±17.20

Table 8.5:Mean of the results obtained by comparing the five segmentations performed by the software along the transverse plane as the input change.

8.3 Test results of reliability and resilience to occasional events in the cross-sectional plane

8.3.1 Test 1

The performance achieved during the first test of software reliability analysis appears to be high for both patients (tables A.2, A.3). The overall mean values and corresponding standard deviations of statistical parameters for each patient are shown in tables 8.6 and 8.7. In particular, the DSC varies between 0.8 and 0.9, the RVD reaches negative but close to zero results, and the HD is a few millimeters. Finally, compared to the typical range of values the algorithm can take, the errors committed to estimating the area are not excessively significant (with an average

diameter of 15 mm, the area is in the order of 100 mm^2). Overall, the standard deviation obtained for the various parameters does not appear to be particularly high.

DSC	RVD	HD [mm]	Area estimation error [mm^2]
0.9079±0.0322	-0.0613±0.0656	3.24±1.31	15.05±32.71

Table 8.6: Mean and standard deviations of the statistical parameters obtained on all videos of the first patient acquired for Test 1 along the transverse plane.

DSC	RVD	HD [mm]	Area estimation error [mm^2]
0.8492±0.0827	-0.1102±0.1466	3.53±2.08	18.53±33.89

Table 8.7: Mean and standard deviations of the statistical parameters obtained on all videos of the second patient acquired for Test 1 along the transverse plane.

Figure 8.1 shows an example of the Bland-Altman plot obtained for the first video of the second subject and represents a case where the algorithm works correctly. It is visible how the difference between the area values obtained by the software and the respective manuals is extremely small, on the order of 10 mm^2.

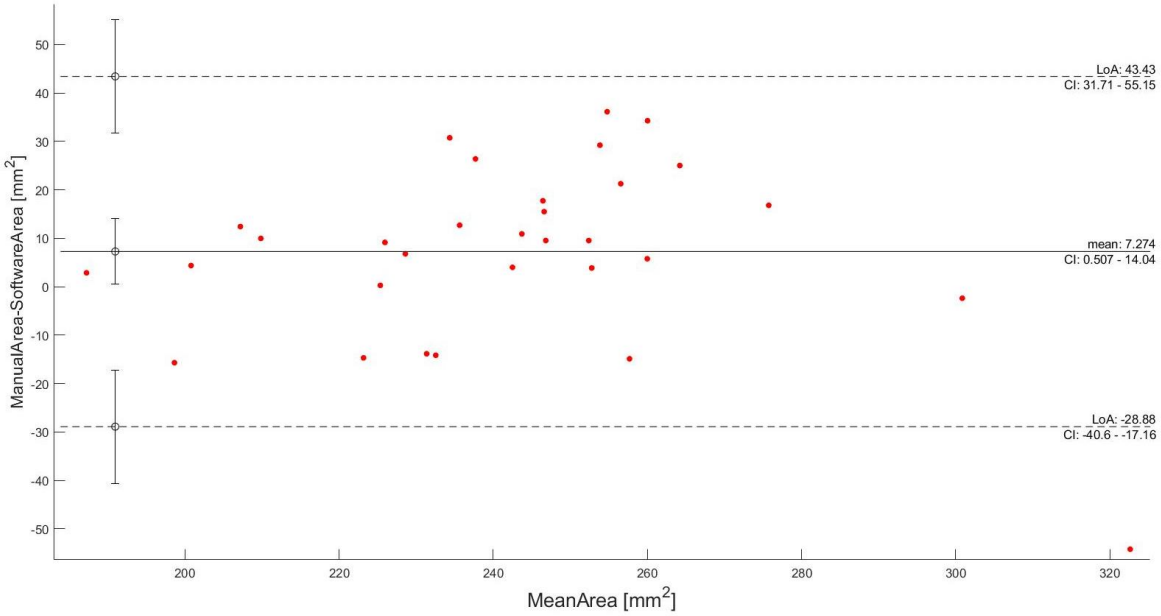

Figure 8.1: The image shows the Bland-Altman plot of the first video of the second patient acquired for Test 1 and represents a case where the algorithm works correctly. The image plots on the x-axis the average area obtained for each frame from manual and software segmentation, and on the y-axis the difference between them.

8.3.2 Test 2

The software, even for long-duration ultrasound videos, generally obtains good results (tables 8.8, 8.9). The values achieved by the statistical parameters are comparable with those described for Test 1 except for the second video of Patient1, which is noisier than the first one. In this case, the algorithm correctly follows the vessel only in the first frames and then loses the vein and fails to recover it.

Video	DSC	RVD	HD [mm]	Area estimation error [mm^2]
1	0.7981±0.1654	-0.2448±0.1798	6.10±4.33	70.08±38.56
2	0.2127±0.3401	-0.8119±0.3235	23.31±10.38	92.30±49.29

Table 8.8: Mean and standard deviations of the statistical parameters obtained on all videos of the first patient acquired for Test 2 along the transverse plane.

Video	DSC	RVD	HD [mm]	Area estimation error [mm^2]
1	0.9172±0.0215	-0.0459±0.0573	1.93±0.57	10.98±16.38
2	0.8998±0.0352	-0.0841±0.0882	2.31±0.76	25.50±26.10

Table 8.9: Mean and standard deviations of the statistical parameters obtained on all videos of the second patient acquired for Test 2 along the transverse plane.

Figures 8.2, 8.3, and 8.4 show three frames of the second video belonging to the first patient. As seen in figure 8.2, the presence of noise inside the vessel makes the vein ill-defined and leads the algorithm to consider pixels inside the IVC as edge points. This inaccuracy becomes more significant in subsequent frames, shown in figure 8.3. The algorithm detects only the right edge of the vein and discards all edge points found on the left because they are too far from the center. When the displacement of the center becomes so important, the software selects edge points belonging to the aorta and completely misses the inferior vena cava, as visible in figure 8.4.

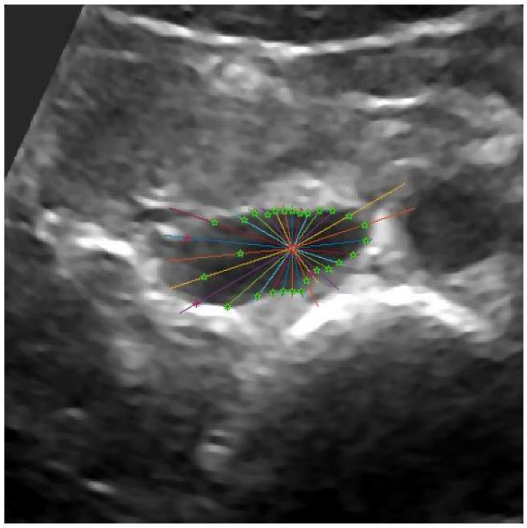

Figure 8.2: The image shows frame 370 of the second video of the first patient acquired during Test 2. In green are represented the edge points recognized as correct by the software and in red are those discarded because they are too far from the center, which is identified with a red circle. It is visible how the presence of noise inside the vessel leads the algorithm to recognize pixels inside the vein as edge points.

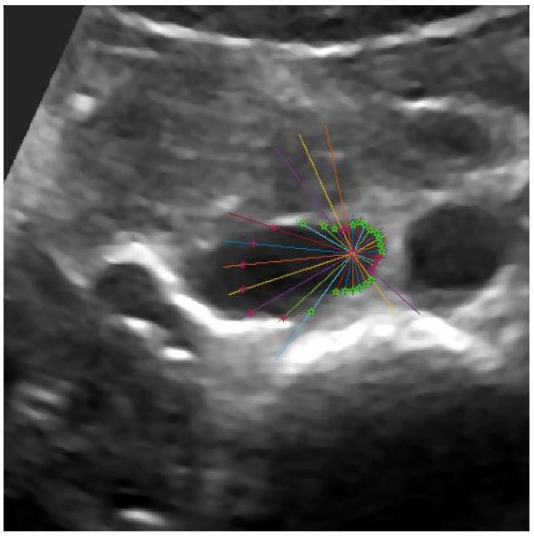

Figure 8.3: The figure represents frame 490 of the second video of the first patient acquired during Test 2 and shows how the error in edge point identification results in the incorrect estimation of the center of the vessel segmentation. In green are represented the edge points recognized as correct by the software and in red are those discarded because they are too far from the center, which is identified with a red circle.

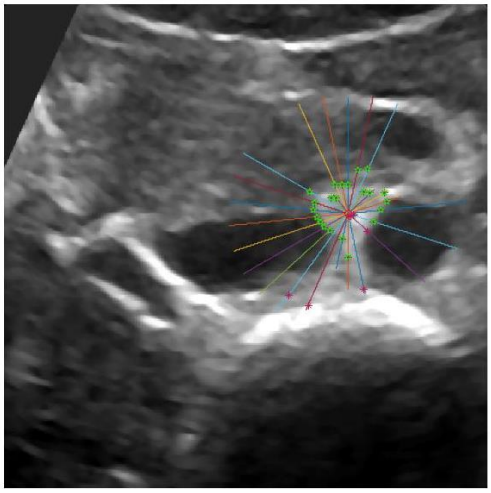

Figure 8.4: The figure represents frame 600 of the second video of the first patient acquired during Test 2. Edge points recognized as correct by the software are represented in green, discarded points in red, and the center of the vessel is identified by a red circle. As seen the excessive displacement of the center leads the software to recognize pixels belonging to the aorta as edge points.

Figure 8.5 shows Bland-Altman's plot of the same video. As visible, the difference between manual and software-estimated segmentation areas is particularly significant, for some frames greater than 200 mm^2.

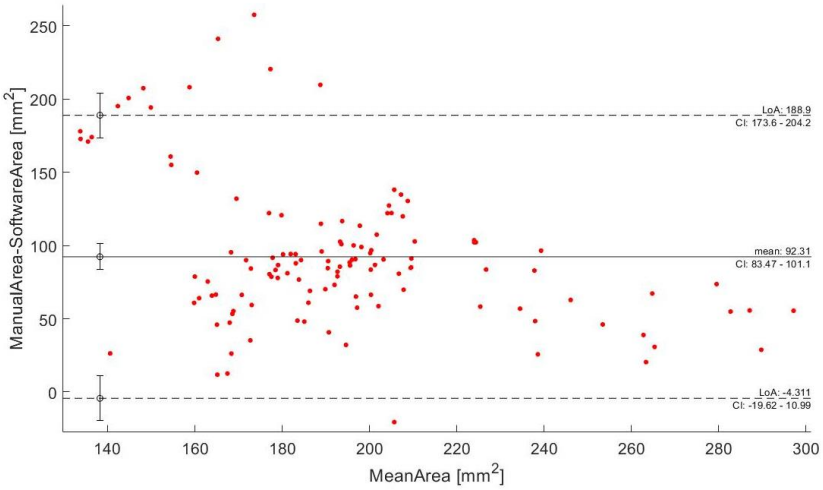

Figure 8.5: The figure shows the Bland-Altman plot of the second video of the first patient acquired for Test 2 along the transverse plane. The image shows the area estimation error committed by the software in the case of particularly noisy videos. The image plots on the x-axis the average area obtained for each frame from manual and software segmentation, and on the y-axis the difference between them.

8.3.3 Test 3

The performance achieved for this test agrees with the results obtained in previous cases. The statistical parameters show comparable values to the other tests with an average DSC of 0.8, an HD on the order of a few millimeters, a negative and close to zero RVD, and an area error that

is not very high (table 8.10, 8.11). The same problem that occurred in Test 2 is also present in the first and third videos of Patient1. Similarly, due to internal noise, segmentation is focused on the right side of the vessel until the vein is completely lost.

Video	DSC	RVD	HD [mm]	Area estimation error [mm^2]
1	0.3473±0.3871	-0.4987±0.2981	15.86±8.38	31.31±99.81
2	0.8871±0.0501	-0.0964±0.0877	3.62±1.52	38.75±35.78
3	0.3512±0.4112	0.0292±0.2172	13.70±8.07	-51.80±95.25
4	0.6809±0.3473	0.0061±0.3702	7.58±7.44	-2.44±102.75
5	0.8400±0.1118	-0.1708±0.1595	4.75±3.39	49.99±36.95

Table 8.10: Mean and standard deviations of the statistical parameters obtained on all videos of the first patient acquired for Test 3 along the transverse plane.

Video	DSC	RVD	HD [mm]	Area estimation error [mm^2]
1	0.8486±0.1754	-0.0844±0.2289	3.43±3.56	4.43±41.69
2	0.8632±0.0485	-0.0380±0.1231	2.96±1.04	0.73±33.34
3	0.8071±0.1188	-0.1713±0.1580	4.28±2.62	37.59±42.39
4	0.8504±0.0633	-0.0567±0.1305	3.08±1.29	5.97±32.60
5	0.8822±0.0421	-0.0339±0.0746	2.64±0.85	-4.90±23.65

Table 8.11: Mean and standard deviations of the statistical parameters obtained on all videos of the second patient acquired for Test 3 along the transverse plane.

The Bland-Altman plot of the third video of the first patient is reported in figure 8.6 to understand the negative value of the area error obtained. From the figure, the algorithm predicts a smaller area than manual segmentation for more than half of the video, while for the remaining frames the values obtained are larger than the actual vessel size. This is possible because although in the first frames the software segments only the right side of the vein, once the vessel

is lost the estimation error takes on positive values for some frames and negative values for others.

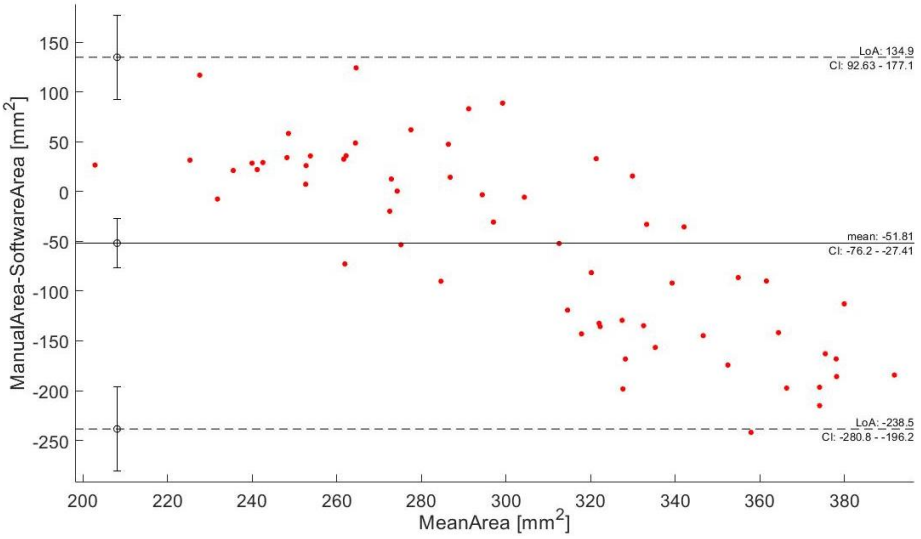

Figure 8.6: The figure shows the Bland-Altman plot of the third video of the first patient acquired for Test 3 along the transverse plane. The image represents a case in which the algorithm initially segments only a portion of the vein, due to the noise inside, and then misses the vessel completely. After this event, the software estimates a larger area than it really is. The graph plots in the x-axis the average area obtained for each frame from manual and software segmentation, and in the y-axis the difference between them.

8.3.4 Test 4

The performance achieved by the software in the fourth test is not particularly high, and this is shown by the values of the statistical parameters obtained (tables A.4, A.5). For only the frames where the vessel is present the DSC has an average value of about 0.4, the RVD reaches even more negative values than in the previous tests and the HD achieves results above 10 mm. Finally, the area estimation error committed by the algorithm appears to have a mean value that is not very high but is characterized by high variability (tables 8.12, 8.14). The estimated area values for frames where the vessel is not present are particularly high, comparable to the values that the IVC can take under physiological conditions (tables 8.13, 8.15). Examples of Bland-Altman plots are not shown for this test because not considering the frames in which the vein disappears makes them unrepresentative.

DSC	RVD	HD [mm]	Area estimation error [mm^2]
0.3934±0.4126	-0.4535±0.4375	13.37±12.61	12.43±135.78

Table 8.12: Mean and standard deviations of the statistical parameters obtained on all videos of the first patient acquired for Test 4 along the transverse plane.

Video	Area [mm^2]
1	192.33±31.82
2	284.55±82.30
3	372.12±72.03
4	276.28±77.53
5	261.53±65.95

Table 8.13: Mean and standard deviation of the estimated area in the frames in which the vessel is not present. The results are reported for each video of Patient1 acquired for Test 4 along the transverse plane in which the vein disappears.

DSC	RVD	HD [mm]	Area estimation error [mm^2]
0.4636±0.4555	-0.3117±0.4119	10.78±14.17	-19.86±134.31

Table 8.14: Mean and standard deviations of the statistical parameters obtained on all videos of the second patient acquired for Test 4 along the transverse plane.

Video	Area [mm^2]
1	219.37±58.30
2	277.80±74.88
3	238.84±62.44
4	293.30±90.75
5	288.37±170.31

Table 8.15: Mean and standard deviation of the estimated area in the frames in which the vessel is not present. The results are reported for each video of Patient2 acquired for Test 4 along the transverse plane in which the vein disappears.

8.3.5 Test 5

The software also achieves suboptimal performance in the case of sudden pressure change (tables A.6, A.7). The statistical parameter values are generally very similar to the results obtained for the previous test, as visible from the averages shown in tables 8.16 and 8.18. The areas estimated by the software in frames where the vein is not visible still turn out to be very high (tables 8.17, 8.19). Also in this case, examples of Bland-Altman plots are not reported because they are not representative of the frames of most interest.

DSC	RVD	HD [mm]	Area estimation error [mm^2]
0.5520±0.4108	-0.1741±0.3400	7.45±9.33	-23.53±135.52

Table 8.16: Mean and standard deviations of the statistical parameters obtained on all videos of the first patient acquired for Test 5 along the transverse plane.

Video	Area [mm^2]
1	164.48±75.91
2	230.09±34.59
3	231.02±33.05
4	320.64±95.19
5	223.74±36.24

Table 8.17: Mean and standard deviation of the estimated area in the frames in which the vessel is not present. The results are reported for each video of Patient1 acquired for Test 5 along the transverse plane in which the vein disappears.

DSC	RVD	HD [mm]	Area estimation error [mm^2]
0.5600±0.4329	-0.2574±0.2968	7.71±8.67	7.56±109.76

Table 8.18: Mean and standard deviations of the statistical parameters obtained on all videos of the second patient acquired for Test 5 along the transverse plane.

Video	Area [mm^2]
1	294.36±94.62
2	278.08±227.88
3	288.73±55.72
4	234.39±138.45
5	206.50±105.40

Table 8.19: Mean and standard deviation of the estimated area in the frames in which the vessel is not present. The results are reported for each video of Patient1 acquired for Test 5 along the transverse plane in which the vein disappears.

8.3.6 Test 6

The performance obtained for this test is shown in tables 8.20 and 8.22. It can be analyzed by dividing the videos into two groups, the first one in which the vessel continues to be partially visible and the second in which the vein disappears completely (in this case the estimated area for the corresponding frames is reported). For the first group, the algorithm obtains reasonably high results (see videos 1 and 4 of the first patient and videos 2 and 4 of the second) with a DSC reaching values even higher than 90%. However, in the second case, the result is worse, especially for the noisy videos where the DSC achieves less than 50% (video 5 of patient one).

Video	DSC	RVD	HD [mm]	Area estimation error [mm^2]
1	0.9123±0.0284	-0.0426±0.0910	2.98±1.16	12.13±35.81
2	0.7407±0.2769	-0.0985±0.2084	4.73±3.80	7.18±87.93
3	0.5595±0.2935	-0.3416±0.2475	8.60±5.62	88.06±155.34
4	0.7269±0.2284	0.5307±0.5465	8.03±6.59	-171.81±196.93
5	0.4586±0.4156	-0.2660±0.3268	11.44±11.68	21.78±245.77

Table 8.20: Mean and standard deviations of the statistical parameters obtained on all videos of the first patient acquired for Test 6 along the transverse plane.

In the frames where the vessel disappears, the estimated area is of the order of 100 mm^2 (tables 8.21, 8.23).

Video	Area [mm^2]
2	187.27±0.00
3	193.31±0.59
5	437.47±216.63

Table 8.21: Mean and standard deviation of the estimated area in the frames in which the vessel is not present. The results are reported for each video of Patient1 acquired for Test 6 along the transverse plane in which the vein disappears.

Video	DSC	RVD	HD [mm]	Area estimation error [mm^2]
1	0.7968±0.2655	-0.0508±0.1032	3.75±1.93	-7.62±107.13
2	0.8215±0.1274	-0.1452±0.1220	3.14±1.80	22.20±39.30
3	0.6972±0.3559	-0.0729±0.1734	2.51±2.29	-29.79±94.69
4	0.9238±0.0260	-0.0208±0.0724	1.88±0.54	-0.56±19.36
5	0.6587±0.4241	-0.0915±0.3159	3.21±5.76	-25.13±84.48

Table 8.22: Mean and standard deviations of the statistical parameters obtained on all videos of the second patient acquired for Test 6 along the transverse plane.

Video	Area [mm^2]
1	285.91±0.00
3	210.54±4.05
5	160.23±132.54

Table 8.23: Mean and standard deviation of the estimated area in the frames in which the vessel is not present. The results are reported for each video of Patient2 acquired for Test 6 along the transverse plane in which the vein disappears.

For the fourth video of Patient1 a very high and extremely variable area estimation error is obtained. The processed video shows that the software could not appropriately segment the vessel or later recover it in the frames where the occasional event occurs. This is due to the presence of a clear spot in the upper area of the vein that the algorithm incorrectly identifies as an edge. Below is the Bland-Altman Plot of the same video in figure 8.7. In the frames corresponding to the incorrect processing, the software tends to estimate a much larger area than the real one committing extremely high errors, even exceeding 500 mm^2.

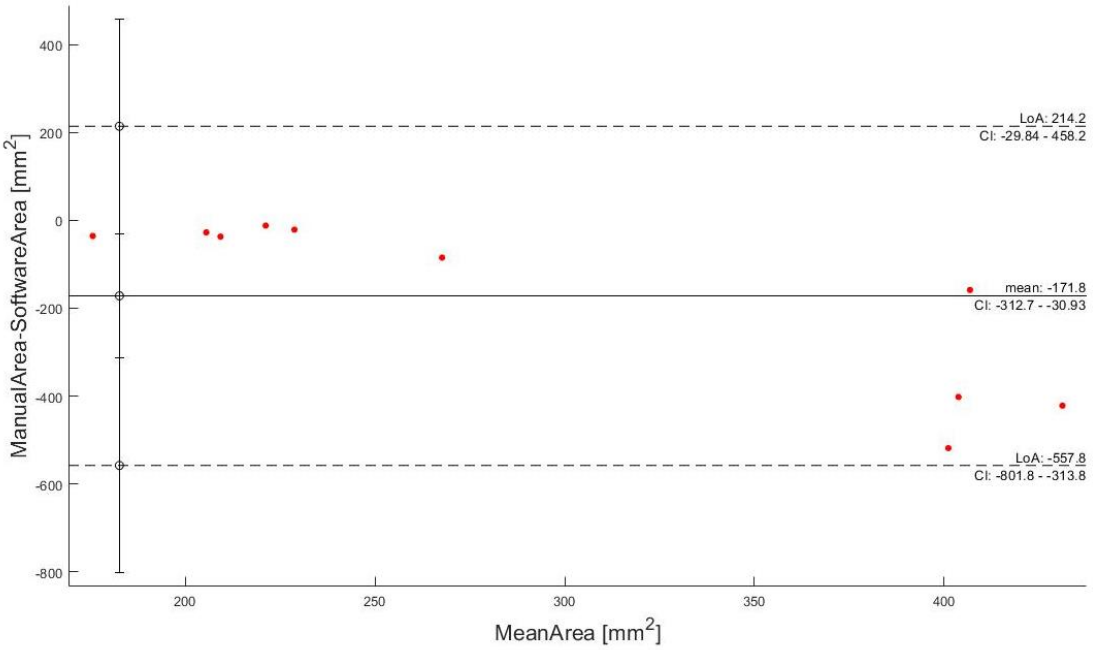

Figure 8.7:The figure represents the Bland-Altman plot of the area estimation error of the fourth video Patient1, acquired for Test 6 along the transverse plane. The plot shows in the x-axis the average area obtained for each frame by manual segmentation and by the software. In this case, after the occasional event, the software makes a very high and variable estimation error due to the presence of a clear spot that the algorithm incorrectly identifies as an edge. The algorithm also fails to recover the correct segmentation in subsequent frames.

8.3.7 Test 7

When a cone of shadow is near the vessel, the performance of the software varies a lot from video to video, depending on the position and intensity of the cone (tables 8.24, 8.25). For example, in video four of Patient1 and video five of Patient2 (figure 8.8), the cone does not completely cover the vessel, and the performance obtained is quite high. Specifically, in these two cases, the DSC reaches a value of about 0.8, the RVD is positive but still close to zero, and the HD is a few millimeters. Finally, the area estimation error is not found to be particularly high even though the artifact decreases the quality of the video. An opposite condition occurs in video three of Patient1 in which the vein is difficult to identify even visually (figure 8.9). For this example, the performance achieved is poor, as demonstrated by the average DSC value below 10%.

Video	DSC	RVD	HD [mm]	Area estimation error [mm^2]
1	0.4874±0.2987	0.1547±0.6832	8.48±3.69	-81.56±59.83
2	0.2784±0.2963	-0.7540±0.3122	19.06±8.52	52.31±88.83
3	0.0680±0.1959	-0.8994±0.3515	23.52±5.22	-30.83±102.93
4	0.7855±0.1338	0.1432±0.5694	5.25±3.76	-38.66±113.53
5	0.1965±0.2732	-0.8211±0.3058	22.69±8.57	68.38±59.78

Table 8.24: Mean and standard deviations of the statistical parameters obtained on all videos of the first patient acquired for Test 7 along the transverse plane.

Video	DSC	RVD	HD [mm]	Area estimation error [mm^2]
1	0.4594±0.0332	0.7948±0.1861	13.54±1.34	-402.01±47.12
2	0.4869±0.0876	0.0457±0.2506	14.41±2.09	-271.94±79.11
3	0.2259±0.2340	-0.5021±0.4852	17.99±7.14	-144.15±79.55
4	0.2284±0.3165	-0.4282±0.7094	22.51±10.61	-151.54±125.54
5	0.8404±0.0814	0.0186±0.1231	4.31±2.85	-35.66±69.00

Table 8.25: Mean and standard deviations of the statistical parameters obtained on all videos of the second patient acquired for Test 7 along the transverse plane.

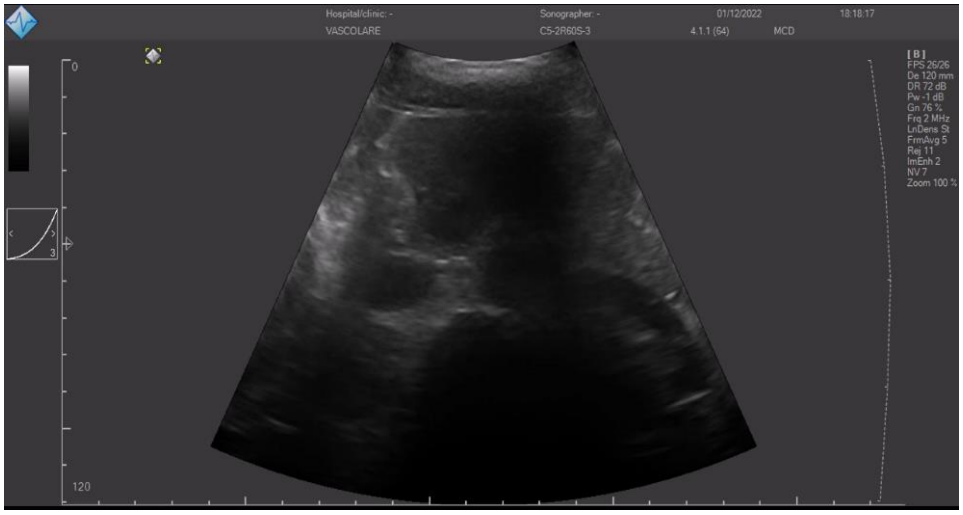

Figure 8.8: The image belongs to the fifth video of the second patient, acquired for Test 7. As visible, the cone is over the aorta and does not cover, even partially, the IVC. However, the presence of the artifact degrades the quality of the video.

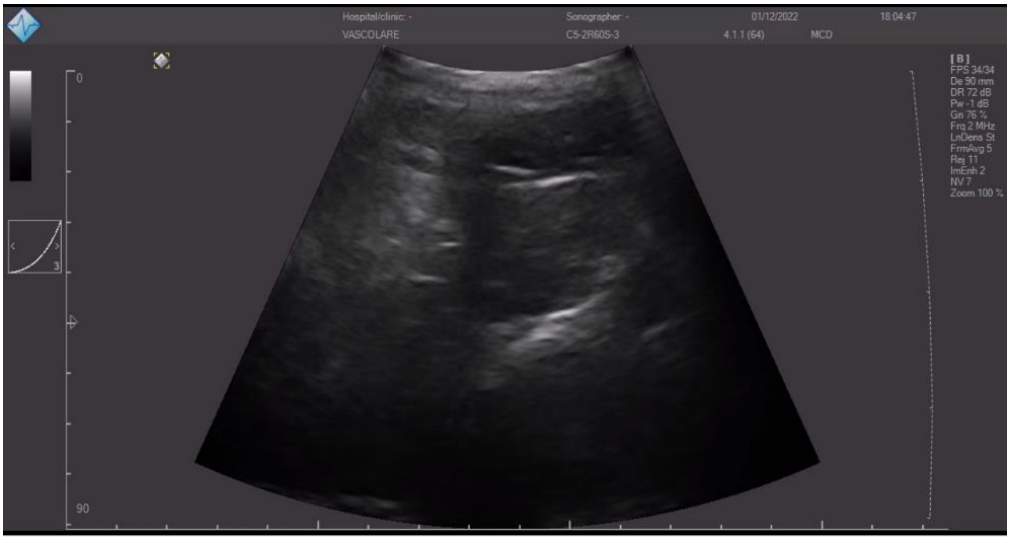

Figure 8.9: The image belongs to the third video of the first patient, acquired for Test 7. In this case, the cone of shadow completely covers the IVC, which is also difficult to identify visually.

8.4 Test results of reliability on hyper- and hypo-volemic patients in the cross-sectional plane

8.4.1 Results obtained for hyper- and eu-volemic patients

The performance obtained in processing the ultrasound videos of the hyper- and eu-volemic patient group appears to be quite high (table A.8). The average values of statistical parameters are shown in table 8.26. The DSC is about 0.82, the RVD shows a mean value of -0.1 with a standard deviation of the same order of magnitude, the value obtained for HD is a few millimeters, and the area estimation error does not appear to be high.

DSC	RVD	HD [mm]	Area estimation error [mm^2]
0.8274±0.0819	-0.1027±0.1359	4.48±2.06	26.06±47.49

Table 8.26: Mean and standard deviations of statistical parameters obtained on all patients belonging to the hyper-and eu-volemic group in the cross-sectional plane.

These results must be evaluated by considering the presence of some problematic videos. In these cases, the software performs very poorly, which affects the final parameter averages (table 8.27).

Video	DSC	RVD	HD [mm]	Area estimation error [mm^2]
10	0.2085±0.2972	-0.0429±0.7643	15.29±4.89	-104.08±141.47
14	0.4892±0.4099	-0.5025±0.4296	13.87±10.72	24.34±83.31
15	0.5908±0.1404	-0.5075±0.2619	16.02±4.93	225.05±151.71
38	0.2977±0.3841	-0.4018±0.1434	12.42±7.49	54.65±27.55

Table 8.27: Mean and standard deviation of the results obtained for the problematic videos belonging to hyper- and eu-volemic patients in the cross-sectional plane.

Videos 10, 14 and 38 turn out to be extremely noisy. In these cases, the software completely misses the vein and fails to recover it due to the unclear intensity variation between the area inside and outside the vessel. A different situation occurs for the fifteenth video in which the software does not lose the vein but fails to segment it completely by focusing only on a small area of the vessel. As seen in figure 8.10, the same condition that was present in Test 2 occurs. An ill-defined outline of the vessel, due to the presence of a black band, leads the software to fail to recognize the left edge. As a result, the center is moved frame by frame to the right, and the few points recognized on the left are discarded because their distance from the center exceeds the working threshold. This is also due to the flattened shape of the vein that leads the two sides to move apart.

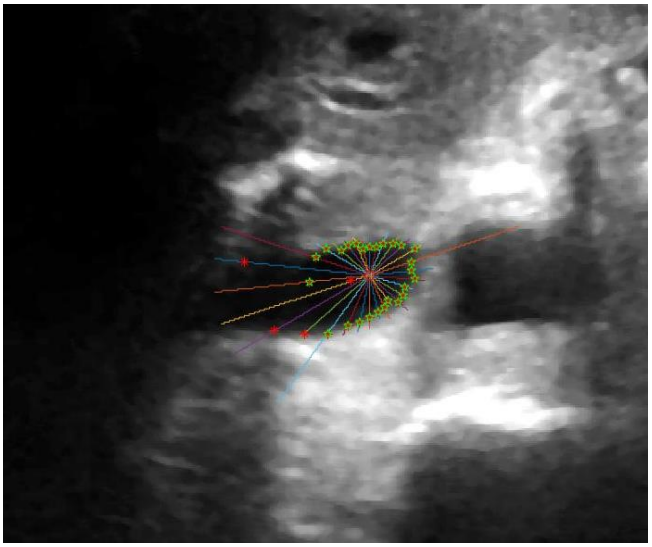

Figure 8.10: The image represents the segmentation of the 20th frame of the video of patient fifteen belonging to the hyper- and eu-volemic group. The detected edge points are shown as red asterisks, the green stars indicate the edge points considered correct, the red circle is the center of the estimated vessel, and the segmentation lines are also represented. From the segmentation it is visible how an ill-defined contour of the vessel leads the software to not recognize the left edge, the center is thus shifted frame by frame to the right

8.4.2 Results obtained for hypo-volemic patients

The performance obtained with patients belonging to the hypo-volemic group is lower (table A.9). In this case, three ultrasound videos, 1, 6, and 13, were excluded. The statistical parameters obtained for these videos show that the algorithm did not segment the vessel correctly. However, these results are not related to the software, but rather to the noisy and poorly defined vessels in the videos, which make even manual segmentation difficult.

The average performance achieved by the software, without considering the three excluded videos, is shown in table 8.28. The software does not achieve good results, as evidenced by the values obtained for RVD and HD but especially by the mean DSC value, which is less than 0.65. Once again, the estimated parameters must be evaluated considering the presence of very noisy videos with low brightness. In contrast to the excluded videos, the vein is always visible in these cases, albeit poorly defined, ensuring that manual segmentation can be performed. The worst results are obtained for the fifth and fourteenth videos where the DSC has a value of less than 10% and the RVD tends to -1.

DSC	RVD	HD [mm]	Area estimation error [mm^2]
0.6266±0.1382	-0.3096±0.2450	10.19±4.20	-19.94±62.98

Table 8.28: Mean and standard deviations of statistical parameters obtained on all patients belonging to the hypo-volemic group in the cross-sectional plane, excluding videos 1, 6 and 13 for which manual segmentation could not be performed.

8.5 Test results of reliability and resilience to occasional events in the longitudinal plane

8.5.1 Test 1

The results obtained for each video of Test 1 are shown in the appendix, Tables A.10 and A.11. Tables 8.29, 8.30 show the values of the statistical parameters obtained as an average over all videos for the first and second patient respectively. The results show a very high performance of the software. For both patients, in fact, the estimated masks overlap almost perfectly with the manual ones as shown by a DSC of about 0.9. The RVD reaches negative values but close to zero and the Hausdorff distance, like the mean diameter error, is minimal. From the performance it is possible to see a difference between the two patients, in the second, in fact, the results achieved by the software are slightly higher. Most probably this is due to the presence of a more well-defined vein in the US videos.

DSC	RVD	HD [mm]	Diameter estimation error [mm]
0.8824±0.0497	-0.0444±0.1199	6.95±1.10	0.70±1.69

Table 8.29: Mean and standard deviation of the statistical parameters obtained for Test 1 of the first patient along the longitudinal plane. The values were calculated by averaging the results of all videos.

DSC	RVD	HD [mm]	Diameter estimation error [mm]
0.9398±0.0242	-0.0022±0.0647	10.21±1.08	0.12±1.43

Table 8.30: Mean and standard deviation of the statistical parameters obtained for Test 1 of the second patient along the longitudinal plane. The values were calculated by averaging the results of all videos.

The figure 8.11 shows the Bland-Altman plot obtained for the 9th video of the second patient where the algorithm reaches the best performance. The error between the diameter estimated manually and that estimated by the software is minimal, on the order of 0.1 mm.

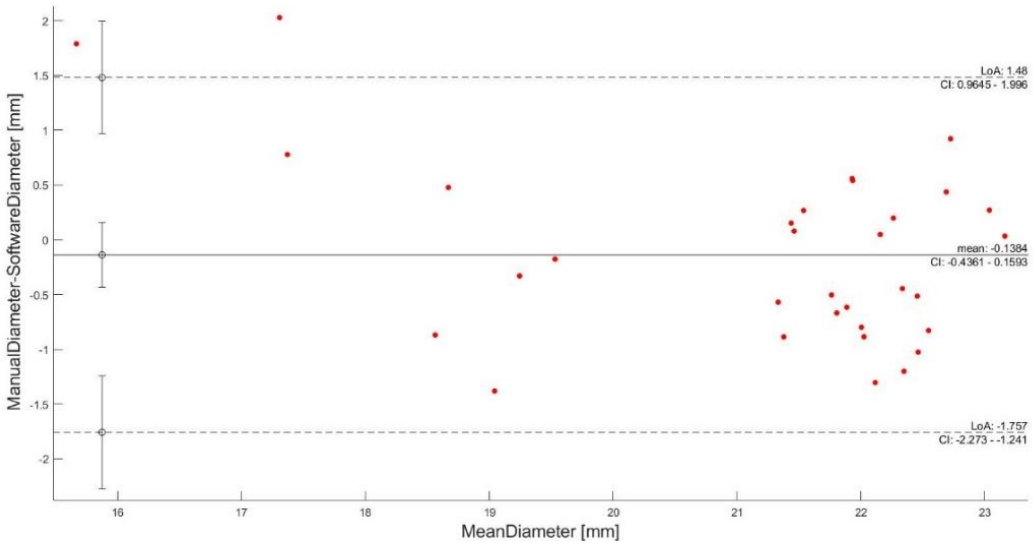

Figure 8.11: The image represents the Bland-Altman Plot of the 9th video of the second patient, acquired in the longitudinal section for Test 1. The algorithm in this case makes a small error in diameter estimation. The average between the diameters obtained from manual and software segmentation for each frame is shown on the x-axis, and the difference between the two diameters is shown on the y-axis.

8.5.2 Test 2

The complete tables containing the results obtained for each video are shown in the appendix (tables A.12 and A.13). The values obtained highlight the software's excellent capabilities in segmenting ultrasound videos of long duration. The statistical parameters calculated as the average of the results of each video are very similar to those achieved for Test 1, in this case there is greater variability between the two patients (tables 8.31, 8.32).

DSC	RVD	HD [mm]	Diameter estimation error [mm]
0.8523±0.05770	-0.1171±0.1416	7.00±1.22	1.83±2.70

Table 8.31: Mean and standard deviation of the statistical parameters obtained for Test 2 of the first patient along the longitudinal plane. The values were calculated by averaging the results of all videos

DSC	RVD	HD [mm]	Diameter estimation error [mm]
0.9444±0.0291	0.0083±0.0666	10.27±1.16	-0.25± 1.31

Table 8.32: Mean and standard deviation of the statistical parameters obtained for Test 2 of the second patient along the longitudinal plane. The values were calculated by averaging the results of all videos.

8.5.3 Test 3

The complete tables with the results obtained for each video are given in the appendix and show good performance achieved by the software (tables A.14, A.15). Tables 8.33 and 8.34 show the values averaged over all the videos for each patient.

DSC	RVD	HD [mm]	Diameter estimation error [mm]
0.8641±0.0893	-0.0286±0.1966	7.98±1.77	0.28±3.65

Table 8.33: Mean and standard deviation of the statistical parameters obtained for Test 3 of the first patient along the longitudinal plane. The values were calculated by averaging the results of all videos

DSC	RVD	HD [mm]	Diameter estimation error [mm]
0.9262±0.0434	0.0032±0.0948	8.88±1.63	-0.65±3.96

Table 8.34: Mean and standard deviation of the statistical parameters obtained for Test 3 of the second patient along the longitudinal plane. The values were calculated by averaging the results of all videos.

8.5.4 Test 4

Slightly worse results are obtained for this test (see tables A.16 and A.17 for all results). For frames in which the vein is visible, performance remains quite high as demonstrated by an average DSC value of about 0.7, RVD and HD similar to that obtained for previous tests, and finally, a diameter error that is not particularly high (tables 8.35, 8.37). However, at the frames in which the vessel disappears, the software continues to estimate a diameter of approximately 10 mm (tables 8.36, 8.38).

DSC	RVD	HD [mm]	Diameter estimation error [mm]
0.6899±0.3241	-0.0936±0.1174	6.59±3.41	1.55±1.87

Table 8.35: Mean and standard deviation of the statistical parameters obtained for Test 4 of the first patient along the longitudinal plane. The values were calculated by averaging the results of all videos.

Video	Diameter [mm]
1	12.57±1.24
2	12.20±2.18
3	11.62±1.68
4	6.66±1.86
5	8.31±1.82

Table 8.36: Mean and standard deviation of the mean diameter estimated by the software in the frames in which the vessel is not present is shown. The results are shown for each video of patient 1 acquired for Test 4.

DSC	RVD	HD [mm]	Diameter estimation error [mm]
0.7776±0.3462	-0.0016±0.0717	7.52±3.45	-0.05± 1.48

Table 8.37: Mean and standard deviation of the statistical parameters obtained for Test 4 of the second patient along the longitudinal plane. The values were calculated by averaging the results of all videos.

Video	Diameter [mm]
1	16.33±1.76
2	10.56±3.15
3	22.15±2.05
4	17.39±1.37
5	17.09±2.63

Table 8.38: Mean and standard deviation of the mean diameter estimated by the software in the frames in which the vessel is not present is shown. The results are shown for each video of patient 2 acquired for Test 4.

8.5.5 Test 5

The results obtained in each video for both patients during the fifth test are shown in the appendix (tables A.18, A.19). The values of the statistical parameters estimated in the frames in which the vessel is visible are similar to those achieved in the first tests. The average values (tables 8.39, 8.41) show a DSC of about 0.8, an RVD close to zero, a HD and a diameter error that are not very high. In the frames in which the vein disappears, the software commits a segmentation error by estimating a diameter in the order of 10 mm (tables 8.40, 8.42).

DSC	RVD	HD [mm]	Diameter estimation error [mm]
0.7708±0.2614	-0.0493±0.1079	6.42±2.47	0.54±1.73

Table 8.39: Mean and standard deviation of the statistical parameters obtained for Test 5 of the first patient along the longitudinal plane. The values were calculated by averaging the results of all videos

Video	Diameter [mm]
1	5.64±0.00
2	10.56±0.08
3	11.34±2.26
4	12.50±0.00
5	10.66±0.00

Table 8.40: Mean and standard deviation of the mean diameter estimated by the software in the frames in which the vessel is not present is shown. The results are shown for each video of patient 1 acquired for Test 5.

DSC	RVD	HD [mm]	Diameter estimation error [mm]
0.8345± 0.2614	0.0427±0.1319	8.31±2.80	-0.82± 3.61

Table 8.41: Mean and standard deviation of the statistical parameters obtained for Test 5 of the second patient along the longitudinal plane. The values were calculated by averaging the results of all videos.

Video	Diameter [mm]
1	18.06±0.00
2	23.18±1.73
3	17.72±1.80
4	18.17±0.00
5	14.87±0.85

Table 8.42: Mean and standard deviation of the mean diameter estimated by the software in the frames in which the vessel is not present is shown. The results are shown for each video of patient 2 acquired for Test 5.

8.5.6 Test 6

For the sixth test, the results achieved show good segmentation capabilities of the software (tables 8.43, 8.45). Again, statistical parameters were estimated only for those frames in which the vein is present but, unlike the previous tests, the disappearance of the vessel did not occur in all videos. When the vein disappears (videos 1 and 2 of the first patient and videos 2, 3 and 5 of the second), the performance achieved are slightly lower, the DSC does not exceed a value of 0.85 in contrast to the other videos in which it always reaches higher values. For the other parameters, comparable results are obtained.

Video	DSC	RVD	HD [mm]	Diameter estimation error [mm]
1	0.8047±0.2834	0.0376±0.2642	6.31±2.56	0.51±1.60
2	0.7780±0.2801	0.1246±0.4349	6.81±2.66	-0.66±3.65
3	0.8799±0.0343	-0.0474±0.0867	6.09±0.94	0.70±1.13
4	0.8875±0.0740	0.1121±0.2149	7.37±1.35	-1.17±2.24
5	0.8846±0.0943	0.0437±0.2722	8.13±1.27	-0.47±2.93

Table 8.43: Mean and standard deviation of the statistical parameters obtained for each video of the first patient during Test 6 along the longitudinal plane.

As in the previous tests of resilience to occasional events, in the frames in which the vessel disappears, the diameter estimated by the software is of the order of 10 mm (tables 8.44, 8.46).

Video	Diameter [mm]
1	10.64±0.00
2	14.21±0.00

Table 8.44: Mean and standard deviation of the mean diameter estimated by the software in frames where the vessel is not present. Results are only reported for videos of Test 6 of the first patient in which the vein disappears.

Video	DSC	RVD	HD [mm]	Diameter estimation error [mm]
1	0.9380±0.0412	0.0501±0.0950	8.68±1.31	-0.85±1.83
2	0.7501±0.3759	0.0041±0.1093	7.65±4.11	-0.45±3.31
3	0.8522±0.2834	0.0167±0.0589	7.80±2.74	-0.22±1.18
4	0.9362±0.0322	0.0456±0.0808	8.45±0.95	-0.37±1.22
5	0.8565±0.2849	0.0007±0.0246	8.26±2.88	-0.07±0.66

Table 8.45: Mean and standard deviation of the statistical parameters obtained for each video of the second patient during Test 6 along the longitudinal plane.

Video	Diameter [mm]
2	10.97±0.20
3	19.42±0.00
5	19.95±0.00

Table 8.46: Mean and standard deviation of the mean diameter estimated by the software in frames where the vessel is not present. Results are only reported for videos of Test 6 of the second patient in which the vein disappears.

8.5.7 Test 7

In contrast to the transverse plane, the shadow cone always covered a part of the IVC and was included in the software segmentation zone selected by input. The results achieved by the algorithm are quite high, as demonstrated by the statistical parameters obtained for each video and reported in the appendix (tables A.20, A.21). Tables 8.47 and 8.48 show the overall values of the parameters. The average DSC is about 0.8, the RVD is different in the two subjects but still close to zero (for the first patient an RVD of an order of magnitude lower than for the second patient was estimated). The HD and diameter error are slightly higher than the average values obtained for the previous tests.

DSC	RVD	HD [mm]	Diameter estimation error [mm]
0.8440±0.0509	-0.0214±0.1512	7.62±1.28	0.36±2.20

Table 8.47: Mean and standard deviation of the statistical parameters obtained for Test 7 of the first patient along the longitudinal plane. The values were calculated by averaging the results of all videos

DSC	RVD	HD [mm]	Diameter estimation error [mm]
0.7993±0.0943	0.2900± 0.2326	11.23±2.72	-3.72± 2.41

Table 8.48: Mean and standard deviation of the statistical parameters obtained for Test 7 of the second patient along the longitudinal plane. The values were calculated by averaging the results of all videos.

8.6 Test results of reliability on hyper- and hypo-volemic patients in the longitudinal plane

A problem was observed during this test for some videos of hypo-volemic patients. In this case, when the vein comes to close completely, the two edges estimated by the software overlap preventing the calculation of the segmentation lines and consequently the processing of the video. An example is shown in figure 8.12 representing frame 557 of the third patient belonging to the hypo-volemic group in which this error occurs. It is visible, in fact, how the right side of the vessel is completely flattened leading the two edge lines to coincide. Due to this problem, in the hypo-volemic patients, only the vein segments that did not completely close were segmented, making the division into two groups unnecessary.

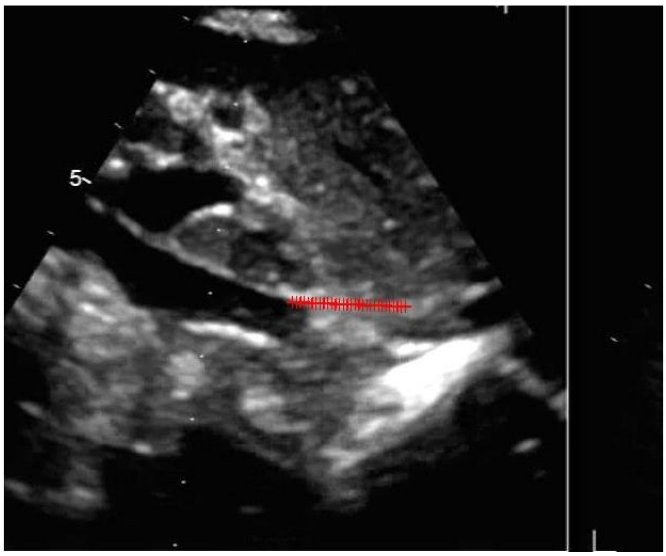

Figure 8.12: The image represents frame 577 of the third patient belonging to the hypo-volemic group and it is visible how the two segmentation edges, depicted in red, overlap.

The software achieves a very high performance, as can be seen in table A.22 in the appendix. As similar parameters were obtained for each video, the results were averaged and reported in table 8.49. In particular, the DSC is greater than 0.9 and the RVD is close to zero. The error committed by the algorithm in estimating the diameter also shows that the software achieved a very good result. The HD obtained is slightly higher than the optimal result although it does not exceed the value of 14 mm in any case.

DSC	RVD	HD [mm]	Diameter estimation error [mm]
0.9161±0.0362	0.0020± 0.0802	10.12±1.22	0.00± 1.65

Table 8.49: Mean and standard deviation of the statistical parameters obtained for the patients belonging to the hyper- and hypo-volemic group in the longitudinal plane. The values were calculated by averaging the results of all videos.

Chapter 9

Discussion

9.1 Limits and capabilities of VIPER software in the cross-sectional plane

Along the transverse plane, the software shows repeatability of processing as user input changes. In fact, the values of statistical parameters do not vary significantly by changing the initial position of the vessel center.

To properly evaluate the software's capabilities, particular attention should be paid to the variability of manual segmentations. In fact, from the results obtained, it is possible to conclude how the errors made by the algorithm may depend in part on the inaccuracy of the segmentations with which the software is compared. Since the DSC obtained for the inter- and intra-operator variability tests is about 0.90, it can be concluded that values above 0.85 for this parameter can be considered optimal.

The results show that the software can correctly segment the vessel in ultrasound videos acquired under static conditions, which are not excessively noisy and are characterized by a well-defined vein edge. Additionally, in high-quality videos, it is evident from the performances that the algorithm can track movement by correctly detecting moving vein edges. In fact, one of the first issues is the software's sensitivity to noise, which is demonstrated by the results obtained in all the videos where the presence of this disturbance makes the vessel ill-defined (as happens in the second video of Test 2 belonging to the first patient). For example, this occurs in patient 15 belonging to the hyper- eu-volemic group (for whom the software fails to correctly identify the left border because of a dark area near the vein), and in all videos of Test 7 in which the shadow cone almost completely overlaps the vessel. In conclusion, in low-contrast, noisy ultrasound videos or those characterized by light or dark bands, the software fails to correctly detect the edge because it is incapable of recognizing a sharp difference in intensity between the inside and outside of the vessel due to the poorly defined edges.

A further limitation of the software is in its ability to correctly segment small vessels, as demonstrated by the results obtained for hypo-volemic patients. In some of these patients the vein tends to close completely, as initially assumed. In addition, when noise is also present, the software fails to segment correctly and loses the vein without recovering it. The lower area limit introduced in the Matlab code allows the software to not lose the vein in less critical hypo-volemic patients while over-segmenting it at the time of vessel closure. However, this limit is insufficient to ensure good performance for low-quality video.

In general, in both the disappearing vein and occasional event simulation tests, the IVC is no longer visible in the ultrasound video when the event occurs. From this point on, the software no longer segments the vessel correctly; not recognizing its disappearance, it continues to process an incorrect portion of the video (as evidenced by the area values obtained in the corresponding frames where the vein is not present). After the event, segmentation resumes correctly only when the vessel reappears at the area where the algorithm is assuming the vein. Different results are obtained when the vessel is partially visible in these cases the algorithm does not miss the vein and segment correctly for the entire duration of the ultrasound video.

Another assessment to be made is that, when the software segments an incorrect region of the video, the area values obtained must be critically evaluated because they are not representative of the vein. This is demonstrated, for example, in the results obtained for Test 7 where the area error in video 3 of Patient1, in which the software completely misses the veins during processing (DSC=0.06), is better than the values obtained for the fourth video of the same patient, in which the segmentation capabilities of the algorithm are significantly higher (DSC=0.78).

Additionally, from the values obtained for RVD in the different tests, it is possible to show a tendency of the software to under-segment, which is more pronounced in videos affected by noise and of low quality.

9.2 Limits and capabilities of VIPER software in the longitudinal plane

The algorithm along the longitudinal plane is very sensitive to user input. In fact, the software obtained very different results from processing the same ultrasound video. The segmentation is influenced by the choice of the area of the vessel to be processed. It is possible to identify portions of the vein in the videos that are characterized by more or less defined edges, leading the algorithm to obtain different results. In addition, the software is strongly dependent on the reference points that ensure the algorithm's ability to properly follow the vessel's movements. Selecting a correct location for these points is not always easy. In fact, often, it is necessary to visualize the ultrasound video beforehand to identify those anatomical areas characterized by features that are easily recognized (by the algorithm). Even along this plane, there is a variability of manual segmentations that must be considered when evaluating the results obtained.

In general, the performance achieved is even higher than that obtained for the transverse plane. In the case of noisy videos, it is sufficient that only a portion of the vessel is unaffected by artefacts for the software not to miss the vein. In the longitudinal plane, in fact, the segmentation lines are uniformly distributed along the portion of the vessel to be processed and include areas with well-defined edges that anchor the segmentation to the vein. For this reason, the software along this plane is less sensitive to the presence of noise, of light or dark bands or low contrast.

Except for particularly noisy videos, the algorithm performs less precise segmentation in areas affected by artefacts but never loses the vessel. In Test 7 for example, in areas where the cone is present, the software estimates the edge more less correctly depending on the intensity of the artefact and segments the rest of the vein correctly, achieving high performance.

Even along the longitudinal plane, the SW can correctly segment the vessel during a movement of the probe. The performance obtained demonstrates the algorithm's ability to not miss the vein and to make only small errors in segmentation. However, these results do not guarantee that the software can always process the same portion of the vessel during vein movements. In this case, larger working ROIs should be used for two main reasons. Firstly, to avoid the problem of the approach of the segmentation lines to the edge of the ROI resulting in incorrect segmentation of the lateral area of the vessel. Secondly, a larger working area ensures a wider anatomical view, allowing the reference points not to escape from the ROI during movement.

A limitation of the software, also present in the transverse plane, is the inability to recognize the disappearance of the vessel. As demonstrated by the estimated diameter values in frames where the vein is not present, the software continues to search for the vessel by segmenting incorrect areas of the ultrasound video. An important advantage in the longitudinal plane is a higher probability of recovering the vein after the occasional event. This is due to the larger size of the vessel, segmentation lines that are uniformly distributed in the area of interest and the fact that in general the vein reappears in approximately the same position where it had disappeared.

Another problem that can occur in the longitudinal plane is the overlapping of the edges estimated by the software. This could happen for example in frames in which the vein disappears or in the case of hypo-volemic patients in which the vessel comes to a complete closure. When this overlap occurs, the algorithm crashes and cannot finish processing. In general, the software achieves good performance even in the case of ultrasound videos acquired by medical personnel. However, to avoid the problem of overlapping edges for hypo-volemic patients, a working zone had to be chosen in which the vessel does not completely close.

Chapter 10

Conclusion

The aim of this study was to evaluate the VIPER software's ability to segment IVC, both in the transverse and longitudinal plane, in different working conditions. The performances were analyzed by comparison with manual segmentation, taking the variability of the latter into account. The results showed that the algorithm correctly identifies and segments the vein in both planes during static conditions and controlled movements of the probe. The analysis, however, also revealed an important dependence of the software on noise and artefacts in the processed ultrasound videos. From this point of view, the longitudinal plane proved to be more stable and robust. The algorithm along this plane, in fact, only needs small, well-defined portions of the vein to not miss the vessel and make only minimal segmentation errors (the average DSC obtained for the first three tests was 0.9015±0.0489). In contrast, the transverse plane showed greater sensitivity to noise as demonstrated by the lower performances achieved (the average DSC obtained for the first three tests was 0.7738±0.1139). However, the most modern ultrasound scanners ensure superior performance compared to the probe used in this study. Indeed, with these devices, it is possible to obtain higher quality ultrasound videos and to apply effective filters to attenuate artefacts in the most problematic situations. The use of more modern probes makes it possible to decrease the software's sensitivity to noise. Another limitation of the software in both plans is the inability to recognize vein disappearance. In such cases, the algorithm estimates incorrect area and diameter values, which can cause incorrect clinical diagnoses and endanger the patient's life. Moreover, when the vein disappears, in the transverse plane the algorithm cannot recover the vessel when it reappears. In contrast, in the longitudinal plane, the software can correctly resume segmentation, achieving better performance than in the transverse plane. In general, the software also showed good results in the segmentation of ultrasound videos acquired by medical personnel, although problems arose in hypo-volemic subjects. In fact, these patients are characterized by small veins that cause difficulties to the algorithm in both working planes. In particular, in the transverse plane, in good quality ultrasound videos the software segments the vessel correctly but overestimates the area in the frames where the vein closes. When, in addition to the small size of the vessel, there is also noise, the algorithm loses the IVC. The average DSC obtained for the hypo-volemic group (DSC=0.6266±0.1382) is significantly lower than that obtained for the hyper- and eu-volemic patients (DSC=0.8274±0.0819). A different problem arose in the longitudinal plane where small vessels caused the edges estimated by the software to overlap, thus blocking processing. Due to this problem, in the hypo-volemic patients, only the vein segments that did not completely close were segmented, making the division into two groups unnecessary (DSC=0.9161±0.0362). An important future goal could be to include a control that prevents this condition from happening, e.g., by imposing a maximum approach distance between the two edges.

The software proved repeatability of processing along the transverse plane as the initial position of the center changed, obtaining very similar performance when comparing the segmentations with the manual masks (DSC=0.8097±0.0085) and very high DSC values when comparing the same segmentations (DSC=0.9636±0.0479). In contrast, in the longitudinal plane, the algorithm is dependent on user input. It was noted that the results obtained from the comparison with manual masks were very different as the position of the reference points and the processed vessel section varied. One method to reduce the variability of the results could be to use a more pronounced contrast in the input selection frame to obtain an initial image that facilitates the placement of the reference points and the selection of a well-defined area of the vein in which no artifacts are present. If this solution is not sufficient, another suggestion would be to limit the number of user input in order to reduce the dependency of the algorithm, while still ensuring sufficient information for the software to perform a correct segmentation.

The presented software works exclusively offline, so it is necessary to first acquire the ultrasound videos and then process them to obtain the information of interest. This could be an important limitation in the clinical setting, where an immediate diagnosis is essential to make the therapy more effective, thus reducing the risks for the patient and the hospitalization time. A new software implementation is being developed in the C++ language, which allows real-time processing ensuring a more immediate response. This algorithm is under development and so far, has only been implemented along the transverse plane, but it already seems to introduce significant advantages. These include the possibility of repositioning the vessel center at any time, which is particularly useful in cases where the software loses the vein or does not recognize its disappearance. In addition, the ROI is no longer fixed and follows the movements of the center of the vessel, so there is no risk of the IVC going outside the working zone generating a segmentation error. Finally, this upgrade opens the possibility of a future implementation on tablets or other portable devices, making the analysis of the inferior vena cava and the study of all its related parameters even easier and faster.

Appendix A

Test	DSC	RVD	HD [mm]	Area estimation difference [mm^2]
1	0.9986±0.0044	0.0000±0.0034	0.15±0.511	-0.01±1.21
2	0.9440±0.0617	-0.0140±0.0479	7.95±10.67	-2.21±24.63
3	0.9730±0.0263	-0.0098±0.0313	3.35±3.45	2.34±11.96
4	0.9681±0.0524	-0.0076±0.0276	4.24±7.62	0.05±15.71
5	0.9441±0.0619	-0.0141±0.0479	7.97±10.70	-2.20±24.61
6	0.9729±0.0263	-0.0098±0.0316	3.34±3.45	2.35±12.04
7	0.9680±0.0524	-0.0077±0.0276	4.28±7.67	0.06±15.74
8	0.9530±0.0642	-0.0274±0.0954	7.02±11.23	4.56±23.29
9	0.9443±0.0746	-0.0238±0.0977	8.00±12.00	2.27±26.82
10	0.9698±0.0547	-0.0165±0.0711	4.21±7.88	2.29±16.03

Table A.1: Performance achieved by comparing the five segmentations obtained by the software in the transverse plane as the input vary.

Video	DSC	RVD	HD [mm]	Area estimation error [mm^2]
1	0.9283±0.0204	-0.0649±0.0423	2.26±0.76	23.48±18.19
2	0.9232±0.0199	-0.0827±0.0373	2.53±0.69	27.01±18.90
3	0.8903±0.0678	-0.1231±0.1085	3.04±1.64	35.28±42.09

Video	DSC	RVD	HD [mm]	Area estimation error [mm^2]
4	0.8781±0.0543	0.0732±0.1339	3.83±2.03	-28.86±49.85
5	0.8875±0.0406	-0.0277±0.1121	3.70±1.88	0.19±50.73
6	0.9141±0.0286	-0.0894±0.0507	2.86±1.00	32.38±26.59
7	0.8940±0.0364	-0.1343±0.0591	3.53±1.19	60.22±31.56
8	0.9278±0.0211	-0.0492±0.0428	2.80±1.09	14.88±22.56
9	0.9194±0.0264	-0.0469±0.0496	2.83±1.07	5.40±32.98
10	0.9236±0.0217	-0.0654±0.0466	2.89±1.25	19.70±29.90
11	0.8873±0.0346	-0.1067±0.0865	3.64±1.04	26.89±45.51
12	0.9061±0.0245	-0.0528±0.0473	4.37±1.71	-9.13±30.35
13	0.9134±0.0335	-0.0174±0.0465	3.72±2.07	-18.13±30.75
14	0.9059±0.0295	-0.0744±0.0592	3.75±1.51	18.88±34.65
15	0.9197±0.0215	-0.0576±0.0613	2.83±0.70	17.63±25.95

Table A.2: Mean and standard deviation of the statistical parameters obtained for each video of the first patient during Test 1 along the transverse plane.

Video	DSC	RVD	HD [mm]	Area estimation error [mm^2]
1	0.9245±0.0277	-0.0344±0.0476	1.85±0.76	7.27±18.44
2	0.8655±0.1353	-0.0561±0.2307	3.39±3.37	7.31±49.23

Video	DSC	RVD	HD [mm]	Area estimation error [mm^2]
3	0.7144±0.1613	-0.1954±0.3857	7.41±3.95	19.81±110.72
4	0.8701±0.0734	-0.0614±0.1455	3.39±1.89	3.80±44.90
5	0.8582±0.1271	-0.1664±0.1755	3.35±3.32	40.69±34.62
6	0.9029±0.0305	-0.0954±0.0726	2.14±0.74	24.99±18.69
7	0.9132±0.0271	-0.0683±0.0707	1.98±0.52	20.86±20.39
8	0.8839±0.0374	-0.0927±0.1039	2.49±1.08	23.51±28.12
9	0.8940±0.0293	-0.0731±0.0985	2.42±0.86	17.10±26.66
10	0.8895±0.0315	-0.0724±0.0677	2.49±0.68	14.37±23.85
11	0.9110±0.0229	-0.0334±0.0745	2.06±0.48	9.59±21.06
12	0.5551±0.4015	-0.4046±0.4233	10.20±9.80	30.16±41.54
13	0.8197±0.0544	-0.1642±0.1037	4.27±1.83	33.33±25.12
14	0.8714±0.0420	-0.0994±0.0911	2.81±1.08	19.93±22.52
15	0.8648±0.0395	-0.0362±0.1079	2.66±0.83	5.17±22.48

Table A.3: Mean and standard deviation of the statistical parameters obtained for each video of the second patient during Test 1 along the transverse plane.

Video	DSC	RVD	HD [mm]	Area estimation error [mm^2]
1	0.2474±0.4053	-0.6389±0.4582	16.98±12.26	17.69±83.10
2	0.4668±0.4421	-0.3637±0.4507	11.35±12.34	10.99±139.30
3	0.4755±0.4269	-0.3869±0.4084	11.30±12.84	21.50±175.67
4	0.3390±0.3651	-0.5249±0.4023	15.89±13.64	10.22±151.33
5	0.4384±0.4238	-0.3533±0.4680	11.31±11.99	1.75±129.50

Table A.4: Mean and standard deviation of statistical parameters obtained for each video of the first patient during Test 4 along the transverse plane.

Video	DSC	RVD	HD [mm]	Area estimation error [mm^2]
1	0.4803±0.4613	-0.3770±0.4738	14.13±16.68	5.80±91.91
2	0.4623±0.4440	-0.3189±0.4263	9.88±13.84	-10.58±157.02
3	0.4484±0.4591	-0.1841±0.2939	6.67±8.71	-29.19±133.31
4	0.4760±0.4575	-0.3348±0.4371	11.55±15.51	-37.64±130.47
5	0.4509±0.4554	-0.3439±0.4284	11.67±16.11	-27.73±158.86

Table A.5: Mean and standard deviation of statistical parameters obtained for each video of the second patient during Test 4 along the transverse plane.

Video	DSC	RVD	HD [mm]	Area estimation error [mm^2]
1	0.5192±0.3702	-0.2553±0.2845	9.22±8.06	21.11±110.50
2	0.4939±0.4160	-0.1671±0.2547	5.49±7.21	-39.12±130.48

Video	DSC	RVD	HD [mm]	Area estimation error [mm^2]
3	0.6860±0.3697	-0.1000±0.2650	4.93±5.79	-0.32±107.27
4	0.5344±0.4565	-0.1845±0.4039	9.71±16.55	-28.57±193.56
5	0.5265±0.4414	-0.1635±0.4919	7.91±9.03	-70.78±135.81

Table A.6: Mean and standard deviation of statistical parameters obtained for each video of the first patient during Test 5 along the transverse plane.

Video	DSC	RVD	HD [mm]	Area estimation error [mm^2]
1	0.4897±0.4449	-0.4128±0.4273	9.34±9.62	42.48±123.50
2	0.5520±0.4434	-0.2508±0.2478	7.14±8.35	15.58±114.88
3	0.5148±0.455	-0.2229±0.2808	9.40±11.14	17.91±118.21
4	0.5118±0.456	-0.3540±0.4711	10.88±13.13	-5.314±94.52
5	0.7318±0.3651	-0.0465±0.0570	1.79±1.12	-32.86±97.68

Table A.7: Mean and standard deviation of statistical parameters obtained for each video of the second patient during Test 5 along the transverse plane.

Video	DSC	RVD	HD [mm]	Area estimation error [mm^2]
1	0.7041±0.3202	-0.1849±0.3728	7.73±7.86	-5.24±90.00
2	0.9566±0.0118	-0.0091±0.0199	1.41±0.42	0.82±9.02
3	0.9138±0.0116	-0.0215±0.0916	1.51±0.35	3.23±20.92
4	0.8374±0.0594	-0.1929±0.0981	4.58±1.46	82.62±42.22

Appendix A

Video	DSC	RVD	HD [mm]	Area estimation error [mm^2]
5	0.8882±0.0504	-0.1118±0.1050	2.43±0.78	39.52±34.08
6	0.7311±0.2554	-0.1004±0.3368	3.46±3.21	-2.41±20.02
7	0.9150±0.0259	-0.0266±0.0775	3.06±1.34	7.93±66.59
8	0.9099±0.0213	-0.0733±0.0592	2.09±0.40	20.03±27.08
9	0.8807±0.0360	-0.1325±0.0671	3.83±1.19	72.88±49.80
10	0.2085±0.2972	-0.0429±0.7643	15.29±4.89	-104.08±141.47
11	0.9177±0.0176	-0.0890±0.0500	2.86±0.70	56.00±40.50
12	0.9358±0.0198	-0.0256±0.0336	2.50±0.82	0.09±28.85
13	0.8266±0.0445	-0.2517±0.0661	4.51±1.00	157.73±50.61
14	0.4892±0.4099	-0.5025±0.4296	13.87±10.72	24.34±83.31
15	0.5908±0.1404	-0.5075±0.2619	16.02±4.93	225.05±151.71
16	0.8946±0.0258	-0.1213±0.0600	3.06±0.71	69.74±40.34
17	0.8516±0.0657	-0.1824±0.1228	2.29±0.74	49.82±33.62
18	0.9179±0.0230	-0.0919±0.0397	2.18±0.44	43.99±28.82
19	0.7894±0.0697	-0.1225±0.2412	7.12±3.61	32.94±147.04
20	0.8744±0.0406	0.0776±0.0842	5.17±2.00	-90.54±55.12
21	0.8706±0.0376	-0.1355±0.0788	3.48±1.55	54.24±37.97

Video	DSC	RVD	HD [mm]	Area estimation error [mm^2]
22	0.9207±0.0196	-0.0282±0.0829	3.12±0.74	27.52±44.06
23	0.8107±0.1761	-0.1076±0.2107	7.20±5.08	25.52±103.80
24	0.9303±0.0192	0.0258±0.0675	2.04±0.57	-10.29±26.25
25	0.9367±0.0159	-0.0318±0.0486	1.82±0.56	11.44±19.79
26	0.8993±0.0244	-0.0298±0.0674	2.46±0.78	14.78±16.83
27	0.8859±0.0607	0.0099±0.0598	4.23±3.26	-47.29±64.02
28	0.8783±0.0300	-0.0405±0.0934	2.70±0.67	1.02±21.70
29	0.9009±0.0235	-0.0590±0.0599	2.46±0.56	16.49±24.21
30	0.8905±0.0278	-0.1345±0.0609	2.74±0.63	61.57±29.42
31	0.9400±0.0159	-0.0620±0.0265	1.62±0.50	20.11±9.48
32	0.9443±0.0141	-0.0344±0.0345	1.92±0.41	15.34±16.35
33	0.8706±0.0619	0.1162±0.1769	4.03±2.16	-38.08±57.83
34	0.8289±0.1255	0.1582±0.3333	3.76±2.37	-38.44±61.31
35	0.8179±0.0686	-0.2285±0.0965	4.19±1.70	64.64±29.76
36	0.8688±0.0370	-0.1620±0.0705	3.06±0.88	62.27±28.90
37	0.9149±0.0259	-0.0458±0.0726	1.95±0.68	10.54±24.41
38	0.2977±0.3841	-0.4018±0.1434	12.42±7.49	54.65±27.55

Table A.8: Mean and standard deviation of the statistical parameters obtained for each subject belonging to the hyper- eu-volemic group in the cross-sectional plane.

Video	DSC	RVD	HD [mm]	Area estimation error [mm^2]
1	-	-	-	-
2	0.5598±0.3268	-0.4158±0.3410	9.53±7.09	-7.85±117.68
3	0.7099±0.1269	-0.3891±0.1634	5.43±2.04	93.94±35.57
4	0.8510±0.0606	-0.0428±0.1307	3.01±1.30	24.67±56.30
5	0.0533±0.2006	-0.9464±0.1984	40.71±18.81	55.51±73.84
6	-	-	-	-
7	0.6686±0.1333	-0.3131±0.2724	4.81±2.22	23.78±26.98
8	0.6206±0.1650	0.04760±0.5950	6.27±3.06	-27.90±85.62
9	0.8320±0.0954	-0.1680±0.1409	3.88±1.94	43.25±35.27
10	0.8417±0.0597	-0.1340±0.1466	2.14±0.79	12.54±14.12
11	0.8033±0.0629	-0.1174±0.1509	2.57±1.08	7.23±11.98
12	0.7535±0.1407	-0.2855±0.2094	2.92±1.17	27.88±17.14
13	-	-	-	-
14	0.0554±0.1864	-0.9227±0.2787	38.15±9.69	-494.58±253.96
15	0.7696±0.1000	-0.0285±0.3127	2.80±1.22	2.19±27.27

Table A.9: Mean and standard deviation of the statistical parameters obtained for the videos of each subject belonging to the hypo-volemic group in the cross-sectional plane.

Video	DSC	RVD	HD [mm]	Diameter estimation error [mm]
1	0.9006±0.0344	0.0893±0.1040	5.98±1.13	-1.22±1.25
2	0.9069±0.0319	0.0029±0.0837	6.89±1.17	0.00±1.22
3	0.8877±0.0401	-0.0926±0.1169	7.11±1.15	1.37±1.71
4	0.8830±0.0414	-0.0406±0.1184	7.07±1.17	0.97±1.78
5	0.8739±0.0552	-0.1253±0.1238	7.41±1.27	2.06±2.22
6	0.8946±0.0303	-0.0477±0.0636	7.48±0.82	0.54±1.56
7	0.8737±0.0550	-0.0601±0.1132	7.18±0.79	1.10±1.56
8	0.8954±0.0515	-0.0596±0.0988	7.35±1.44	0.75±1.33
9	0.8976±0.0412	0.0057±0.1367	6.66±0.93	-0.06±1.43
10	0.8693±0.0578	-0.0338±0.1660	6.17±1.29	0.83±2.28
11	0.8428±0.1101	-0.0908±0.1906	5.70±0.95	0.79±1.97
12	0.8645±0.0667	-0.0633±0.1590	5.69±0.94	0.97±2.04
13	0.8977±0.0353	-0.0514±0.0958	7.72±1.06	1.26±1.63
14	0.8769±0.0608	-0.0109±0.1293	7.09±1.02	-0.03±1.78
15	0.8712±0.0342	-0.0883±0.0991	8.71±1.30	1.14±1.61

Table A.10: Mean and standard deviation of statistical parameters obtained for each video of the first patient during Test 1 along the longitudinal plane.

Video	DSC	RVD	HD [mm]	Diameter estimation error [mm]
1	0.9499±0.0143	0.0137±0.0374	10.97±0.71	0.02±1.00
2	0.9281±0.0231	0.0978±0.0683	9.97±0.76	-2.20±1.62
3	0.9294±0.0280	0.1115±0.0743	10.12±1.21	-1.57±1.39
4	0.9246±0.0241	-0.052±0.0724	10.05±0.82	1.15±1.57
5	0.9443±0.0192	0.0041±0.0494	10.39±0.90	0.04±1.49
6	0.9563±0.0108	0.0264±0.0451	9.66±0.82	-0.37±0.87
7	0.9358±0.0243	-0.0131±0.0877	10.01±0.67	0.29±1.87
8	0.9547±0.0153	0.0013±0.0568	9.25±0.92	0.09±1.05
9	0.9609±0.0140	0.0077±0.0416	10.45±1.36	-0.13±0.82
10	0.8988±0.0606	-0.1208±0.1063	10.54±1.71	2.51±2.22
11	0.9514±0.0169	-0.0011±0.0594	10.42±1.19	0.05±1.17
12	0.9319±0.0329	-0.0405±0.0713	10.02±1.32	0.58±1.50
13	0.9501±0.0164	-0.0118±0.0549	10.61±1.66	0.29±1.16
14	0.9496±0.0180	-0.0008±0.0596	9.57±0.81	0.01±1.70
15	0.9307±0.0456	-0.0553±0.0861	11.15±1.36	1.11±1.96

Table A.11: Mean and standard deviation of statistical parameters obtained for each video of the second patient during Test 1 along the longitudinal plane.

Video	DSC	RVD	HD	Diameter estimation error [mm]
1	0.8411±0.0642	-0.1322±0.1644	6.90±1.39	1.95±2.42
2	0.8636±0.0513	-0.1020±0.1188	7.10±1.04	1.70±2.98

Table A.12: Mean and standard deviation of statistical parameters obtained for each video of the first patient during Test 2 along the longitudinal plane.

Video	DSC	RVD	HD [mm]	Diameter estimation error [mm]
1	0.9493±0.0244	-0.016±0.0481	10.00±0.98	-0.09 ±1.01
2	0.9394±0.0338	0.0327±0.0851	10.53±1.34	-0.40 ±1.62

Table A.13: Mean and standard deviation of statistical parameters obtained for each video of the second patient during Test 2 along the longitudinal plane.

Video	DSC	RVD	HD [mm]	Diameter estimation error [mm]
1	0.8858±0.0393	0.0056±0.1509	7.66±1.28	-0.86±5.05
2	0.8095±0.1930	-0.1072±0.2753	8.27±2.25	1.95±4.18
3	0.8833±0.0714	0.0017±0.1785	8.38±1.63	0.02±3.11
4	0.8525±0.1058	0.0113±0.2903	8.09±2.52	-0.35±4.08
5	0.8894±0.0369	-0.0544±0.0882	7.49±1.16	0.67±1.80

Table A.14: Mean and standard deviation of statistical parameters obtained for each video of the first patient during Test 3 along the longitudinal plane.

Video	DSC	RVD	HD [mm]	Diameter estimation error [mm]
1	0.9036±0.0505	-0.0101±0.1391	7.55±1.38	0.56± 3.06
2	0.9446±0.0284	-0.0003±0.0612	8.61±1.01	-0.85 ±4.41
3	0.932±0.0401	0.0127±0.0807	9.50±1.54	-1.68± 4.34
4	0.9086±0.0585	-0.0047±0.1124	10.04±3.00	-0.84± 5.83
5	0.9419±0.0395	0.0185±0.0809	8.71±1.20	-0.47 ±2.18

Table A.15: Mean and standard deviation of statistical parameters obtained for each video of the second patient during Test 3 along the longitudinal plane.

Video	DSC	RVD	HD [mm]	Diameter estimation error [mm]
1	0.6908±0.3298	-0.0867±0.1053	6.13±3.12	1.85±1.80
2	0.7032±0.3223	-0.0690±0.1170	6.08±3.04	1.27±1.97
3	0.7516±0.2979	-0.0730±0.1103	6.14±2.54	1.26±1.79
4	0.7116±0.3388	-0.0992±0.1036	6.12±3.01	1.98±1.66
5	0.5921±0.3318	-0.1401±0.1507	8.45±5.35	1.42±2.15

Table A.16: Mean and standard deviation of statistical parameters obtained for each video of the first patient during Test 4 along the longitudinal plane.

Video	DSC	RVD	HD [mm]	Diameter estimation error [mm]
1	0.7991±0.3362	-0.0237±0.0545	7.60±3.36	0.38 ±1.15
2	0.7248±0.3824	-0.0015±0.0945	7.03±3.81	-0.20±2.05

Video	DSC	RVD	HD [mm]	Diameter estimation error [mm]
3	0.8548±0.2593	0.0379±0.0879	8.30±2.63	-0.26±1.69
4	0.7617±0.3781	0.0055±0.0547	7.39±3.74	-0.36±1.05
5	0.7477±0.3748	-0.0261±0.0666	7.26±3.72	0.15±1.45

Table A.17: Mean and standard deviation of statistical parameters obtained for each video of the second patient during Test 4 along the longitudinal plane.

Video	DSC	RVD	HD [mm]	Diameter estimation error [mm]
1	0.8170±0.2143	-0.1049±0.1405	5.87±1.51	1.43±1.48
2	0.8019±0.2689	-0.0364±0.1016	5.79±2.02	0.60±1.50
3	0.7595±0.3196	-0.0402±0.0768	6.10±2.70	1.06±1.20
4	0.6239±0.3021	-0.0269±0.1303	9.21±4.76	-0.87±3.42
5	0.8517±0.2020	-0.0379±0.0903	5.12±1.38	0.48±1.06

Table A.18: mean and standard deviation of statistical parameters obtained for each video of the first patient during Test 5 along the longitudinal plane.

Video	DSC	RVD	HD [mm]	Diameter estimation error [mm]
1	0.8931±0.2116	0.0114±0.0777	8.55±2.19	-0.93±1.72
2	0.8097±0.2774	0.1655±0.1919	8.66±3.18	-4.22±4.60
3	0.7938±0.3331	0.0623±0.0932	8.01±3.48	-0.23±2.66
4	0.8754±0.2032	0.0615±0.129	8.46±2.10	-0.84±1.84

Video	DSC	RVD	HD [mm]	Diameter estimation error [mm]
5	0.8004±0.2815	-0.087±0.168	7.89±3.04	2.13 ±7.26

Table A.19: Mean and standard deviation of statistical parameters obtained for each video of the second patient during Test 5 along the longitudinal plane.

Video	DSC	RVD	HD [mm]	Diameter estimation error [mm]
1	0.8494±0.0434	-0.1739±0.078	6.64±0.88	2.59±1.30
2	0.8394±0.0707	-0.1643±0.1304	8.31±0.86	2.37±2.32
3	0.8253±0.0624	0.0093±0.2689	7.03±1.36	-0.32±3.79
4	0.8777±0.0318	-0.0864±0.0911	6.76±1.17	1.18±1.43
5	0.8283±0.0461	0.3081±0.1874	9.36±2.12	-4.01±2.18

Table A.20: Mean and standard deviation of statistical parameters obtained for each video of the first patient during Test 7 along the longitudinal plane.

Video	DSC	RVD	HD [mm]	Diameter estimation error [mm]
1	0.7665±0.1187	0.5102±0.2689	12.01±3.80	-6.24± 2.33
2	0.7697±0.0927	-0.1081±0.1471	12.21±2.32	1.96± 2.46
3	0.7919±0.1051	0.4027±0.3364	11.16±2.14	-7.11± 4.35
4	0.815±0.0913	0.3878±0.2716	10.52±3.38	-3.17 ±1.76
5	0.8534±0.0637	0.2572±0.1388	10.24±1.94	-4.02± 1.15

Table A.21: Mean and standard deviation of statistical parameters obtained for each video of the second patient during Test 7 along the longitudinal plane.

Video	DSC	RVD	HD [mm]	Diameter estimation error [mm]
1	0.9391±0.0137	0.0082±0.0461	14.13±0.75	-0.41±1.36
2	0.9177±0.0315	0.0933±0.0744	13.56±1.19	-2.44±2.19
3	0.8687±0.0621	0.0488±0.1593	4.51±1.06	-0.24±2.08
4	0.9017±0.0377	-0.0245±0.0842	7.04±1.02	-0.03±1.98
5	0.8651±0.0879	0.0340±0.1471	8.53±2.34	-0.15±2.78
6	0.9471±0.0147	-0.0685±0.0395	10.11±1.00	1.57±2.37
7	0.9256±0.0473	-0.0342±0.0787	10.97±1.83	1.18±2.98
8	0.9464±0.0133	-0.0549±0.0368	11.15±0.78	1.39±1.51
9	0.9331±0.0170	0.0154±0.0561	11.10±1.06	-0.81±1.97

Table A.22: Mean and standard deviation of the statistical parameters obtained for each subject belonging to the hyper- and hypo-volemic group along the longitudinal plane.

Bibliography

[1] Seeley R., Stephens T., Tate P.. Anatomy and Physiology, Sixth Edition. The McGraw−Hill Companies, 2004; pp.712-716; 813-840.

[2] Ambrosi G., Cantino D., Castano P., Correr S., D'Este L., Donato R. F., Familiari G., Fornai F., Gulisano M., Iannello A., Magaudda L., Marcello M. F., Martelli A. M., Pacini P., Rende M., Rossi P., Sforza C., Tacchetti C., Toni R., Zummo G. Anatomia dell'uomo. Milano, Edi. Emes, 2010. P.240.

[3] Mesin L., Albani S., Policastro P., Pasquero P., Porta M., Melchiorri C., Leonardi G, Albera C., Scacciatella P., Pellicori P., Stolfo D., Grillo A., Fabris B., Bini R., Giannoni A., Pepe A., Ermini L., Seddone S, Sinagra G., Antonini-Canterin F., Roatta S. Assessment of phasic changes of vascular size by automated edge tracking-state of the art and clinical perspectives. Frontiers in Cardiovascular, January 2022, Vol. 8.

[4] Mesin L., Albani S., Sinagra G. Non-invasive Estimation of Right Atrial Pressure Using Inferior Vena Cava Echography (2019) Ultrasound in Medicine and Biology, 45 (5), pp. 1331-1337.

[5] Albani S., Pinamonti B., Giovinazzo T., De Scordilli M., Fabris E., Stolfo D., Perkan A., Gregorio C., Barbati C., Geri P., Confalonieri M., Lo Giudice F., D. Aquaro g., Pasquero p., Porta M., ·Sinagra G., Mesin L. Accuracy of right atrial pressure estimation using a multi-parameter approach derived from inferior vena cava semi-automated edge-tracking echocardiography: a pilot study in patients with cardiovascular disorders. The International Journal of Cardiovascular Imaging, 19 Marzo 2020.

[6] Mesin L., Policastro P., Albani S., Petersen C., SciarroneP., Taddei C., Giannon A. Non-Invasive estimation of right atrial pressure using a semi-automated echocardiographic tool for inferior vena cava edge-tracking. Journal of Clinical Medicine, 2022, 11, 3257.

[7] Mesin L., Roatta S., Pasquero P., Porta M. Automated Volume Status Assessment Using Inferior Vena Cava Pulsatility. Electronics 2020, 9, 1671.

[8] Ciozda, W., Kedan, I., Kehl, D.W. et al. The efficacy of sonographic measurement of inferior vena cava diameter as an estimate of central venous pressure. Cardiovasc Ultrasound 14, 33 (2015).

[9] Meola M., Cap. I. Principi fisici dell'ecografia. natura e caratteristiche fisiche degli ultrasuoni. Eureka, Lucca, 2008.

[10] Mattoon John S., Nyland T. G. Principi fondamentali di Ecologia Diagnostica, Capitolo I.

[11]: Lombardi Elio G. Application of speckle tracking to follow the edges of the inferior vena cava.

[12] Brahme A. Comprehensive biomedical physics. Volume 1-10. Elsevier, 2014.

[13] Campo A. Simulazione di immagini ad ultrasuoni multi- tessuto: confronto tra immagini cliniche e simulate a diversi stadi patologici.

[14] Tanter M., Fink M. Ultrafast Imaging in Biomedical Ultrasound. IEEE Transactions on Ultrasonics, Ferroelectrics, and Frequency Control, vol. 61, no. 1, January 2014.

[15] Berco J. Ultrafast ultrasound imaging. Ultrasound Imaging Medical Applications, 2011.

[16] https://www.msdmanuals.com/it-it/professionale/argomenti-speciali/principi-di-imaging-radiologico/ecografia

[17] Convissar D., Bittner Edward A., Chang Marvin G. Biplane Imaging Versus Standard Transverse Single-Plane Imaging for Ultrasound-Guided Peripheral Intravenous Access: A Prospective Controlled Crossover Trial. Critical Care Explorations 3(10): p e545, October 2021.

[18] B. Block. Color atlas of Ultrasound anatomy. Thieme, clinical sciences, 2014.

[19] Teixeira-Neto Francisco J., Valverde A. Clinical Application of the Fluid Challenge Approach in Goal-Directed Fluid Therapy: What Can We Learn From Human Studies? Frontiers in Veterinary Science, 3 August, 2021.

[20] Furtado S., Reis L. Inferior vena cava evaluation in fluid therapy decision making in intensive care: practical implications. Rev Bras Ter Intensiva. 2019 Apr-Jun.

[21] Corl K.A., George N.R., Romanoff J., Levinson A.T., Chheng D B., Merchant R.C., et al. Inferior vena cava collapsibility detects fluid responsiveness among spontaneously breathing critically-ill patients. J Crit Care. (2017) 41:130– 7.

[22] Sung Jin Bae M.D., Sun Hwa Lee M.D., Ph. D., Seong Jong Yun M.D., Keon Kim M.D. Comparison of IVC diameter ratio, BUN/creatinine ratio and BUN/albumin ratio for risk prediction in emergency department patients. The American Journal of Emergency Medicine Volume 47, September 2021, Pages 198-204.

[23] Anderson, K.L., Fields, J.M., Jenq, K.Mangili, A., Panebianco, N., Dean, A.J. Test Characteristics of Sonographic Evaluation of IVC Maximum Diameter and IVC Collapsibility Index In Predicting Congestive Heart Failure Among Dyspneic Patients In the Emergency

Department. Annals of Emergency Medicine, Volume 56, Issue 3, Supplement, September 2010, Page S81.

[24] Mesin L., Pasquero P., Albani S., Porta, M., Roatta, S. Semi-automated tracking and continuous monitoring of inferior vena cava diameter in simulated and experimental ultrasound imaging. Ultrasound in Medicine & Biology, Volume 41, Issue 3, 2015, Pages 845-857.

[25] Ermini L., Seddone S., Policastro P., Mesin L., Pasquero P., Roatta S. The cardiac caval index. Improving non invesive assessment of cardiac preload. American Institute of Ultrasound in Medicine, 2021; 9999:1–12.

[26] Mesin L., Pasquero P., Roatta, S. Tracking and monitoring pulsatility of a portion of inferior vena cava from ultrasound imaging in long axis. Ultrasound in Medicine & Biology, Volume 45, Issue 5, 2019, Pages 1338-1343.

[27] Mesin L., Pasquero P., Roatta S. Multi-directional Assessment of Respiratory and Cardiac Pulsatility of the Inferior Vena Cava From Ultrasound Imaging in Short Axis,Ultrasound in Medicine & Biology, Volume 46, Issue 12, 2020, Pages 3475-3482, ISSN 0301-5629.

[28] Albani A., Mesin L., Roatta S., De Luca A., Giannoni A., Stolfo D., Biava L., Bonino C., Contu L., Pelloni E., Attena E., Russo V., Antonini-Canterin F., Pugliese N.R., Gallone G., Maria De Ferrari G., Sinagra G., Scacciatell P. Inferior Vena Cava Edge Tracking Echocardiography: APromising Tool with Applications in Multiple Clinical Settings. Diagnostics 2022,12, 427.

[29] Mesin L., Policastro P., Albani S., Petersen C., Sciarrone P., Taddei C., Giannoni A. Non-Invasive Estimation of Right Atrial Pressure Using a Semi-Automated Echocardiographic Tool for Inferior Vena Cava Edge-Tracking. Journal of Clinical Medicine. 2022, 11, 3257.

[30] https://www.telemedultrasound.com/wp-content/uploads/2020/09/MicrUs-Brochure.pdf

[31] https://www.telemedultrasound.com/wp-content/uploads/2020/09/EchoWaveII-Manuale-Utente.pdf

[32] https://www.medicalexpo.it/prod/telemed-medical-systems/product-70298-718259.html

[33] https://www.3bscientific.com/us/sonotrain-ultrasound-vein-model-1019637-p120-3b-scientific,p_1397_27465.html

[34] Rublee E., Rabaud V., Konolige Gary Bradski K., “ORB: an efficient alternative to SIFT or SURF”. 2011 International Conference on Computer Vision.

[35] Karami E., Shehata M., Mcguire P., Smith A. Ultrasound Image Segmentation Techniques for Tracking and Measurement of the Internal Jugular Vein. Conference: 2015 Newfoundland Electrical and Computer Engineering. Conference At: St. John's, Canada.

[36] Müller D., Soto-Rey I., Kramer F. Towards a guideline for evaluation metrics in medical image segmentation. Müller et al. BMC Research Notes (2022) 15:210.

[37] Giavarina D. Understanding Bland Altman analysis. Biochemia Medica, Vol. 25 No. 2, 2015.

[38] Franco F. Valutazione della concordanza tra misurazioni di caratteri di tipo quantitativo: il metodo di Bland-Altman. Epidemologia e statistica. G Tec Nefrol Dial 2017; 29 (1): 59-61.

[39] Ataei A., Eggermont F., Baars M., van der Linden Y., de Rooy J., Verdonschot N. Evaluation of inter- and intra-operator reliability of manual segmentation of femoral metastatic lesions. International Journal of Computer Assisted Radiology and Surgery volume 16, pages 1841–1849 (2021).

[40] Davico G., Bottin F., Di Martino A., Castafaro V., Baruffaldi F., Faldini C., Viceconti M. Intra-operator Repeatability of Manual Segmentations of the Hip Muscles on Clinical Magnetic Resonance Images. Journal of Digital Imaging (2022).